FINAL DEGREE PROJECT

TITLE: DESIGN OF A GEAR SHIFTING SYSTEM FOR BICYCLES

AUTHOR: ZAMBRANO BRAVO, RONEY EMANUEL

PRESENTATION DATE: July 2023

COGNOMS: ZAMBRANO BRAVO **NOM: RONEY EMANUEL**

TITULACIÓ: ENGINYERÍA MECÀNICA

PLA: 2023

DIRECTOR: INGRID MAGNUSSON MORER

DEPARTAMENT: ENGINYERÍA MECÀNICA

QUALIFICACIÓ DEL TFG

TRIBUNAL

PRESIDENT **SECRETARI** **VOCAL**

DATA DE LECTURA:

Aquest Projecte té en compte aspectes mediambientals: □ Sí X No

ABSTRACT

A gearing system is the mechanism used, by different types of transports, to modify the features of the transmission. This mechanism must adapt the speed, and torque, according to the road conditions and the requirements of the driver, in order to optimise the driving.

In case of bicycles, the transmission mechanism adapts the energy produced by the muscular effort of the driver into rotational movement of the wheels. Nowadays, most of them include a derailleur gearing system, which uses a chain transmission and several chain rings to modify the speed ratio transmitted to the rear wheel.

However, since the different context of use, and users, require different types of bicycles, the market also includes a large variety of designs and gearing proposals.

The main goal of this project is to develop a design proposal based on a gear shifting system. From previous research, with focus on the state of the art and the actual market of bicycles, different ideas of designs arise. As objective, the proposals obtained must accomplish a functional improvement in relation to precedent models and the integration of the different systems studied during the research. Then, these are studied to verify the technical possibilities to carry out each one of them.

The proposal finally selected is a redesign of the shifting system of the Sturmey-Archer gearing hub, which is known to be one of the first internal gearing systems. This mechanism was very popular when was launched but it presented problems in the cable shifting system, which failed in activating the correct speed. As a solution, the design focuses on incorporating the ratchet system of a motorcycle to replace the direct cable shifting.

During the design process, the parts and the assembly are modelled by 3D software, and evaluated by mechanical calculations and simulations, which must guarantee the correct performance of the mechanism. In this process, the materials used are also compared and selected to achieve the safety condition.

To conclude, the development of this project is considered to have followed correctly the process stablished. The results of the different design stages are satisfactory.

Regarding the resulting proposal, it is considered to achieve the safety and functional goals, although some aspect might be modified to obtain a more complete solution.

Keywords (10 maximum):

Gearing system	Derailleur	Ratchet mechanism	Internal gearing hub
Speed ratio	Cable shifting clutch	Design proposal	

INDEX

INDEX OF FIGURES

GLOSSARY OF SIGNS, SIMBOLS, ABBREVIATION, ACRONYM AND WORDS

Speed ratio: Relationship between the output and input velocities of a mechanism.

Yield strength: Maximum load that a material supports before being plastically deformed.

Ultimate strength: Maximum load that a material supports before reaching rupture.

Young modulus: Relationship between the loads supported and the deformations generated in a part, during the elastic performance.

Spring coefficient: Relationship between the loads supported by a spring and its total deformation.

Von Mises stress: Theoretical stress which combines the main axial and shearing stresses of a specific point of the part and is valid to be used in the safety factor calculation.

Neutral fiber: Theoretical line, of the section of a part, that separates the stretched zone from the compressed zone.

Stress concentration: Increase of the stress obtained in specific geometries of a part in relation to the theoretical stress.

Safety factor: Relationship between the yield strength of the material and the maximum stress.

Fatigue strength: Characteristic of the part, derived from the ultimate strength, that allows to describe the maximum dynamic loads that the part supports during the fatigue performance.

Rigidity constant: Constant that relates the young modulus, the thickness and the area affected by the bolted joint.

INTRODUCTION

The bicycle is a two-wheeled personal vehicle, which is propelled by the traveler. It is a relatively simple mean of transport, generally composed of a structural frame, a seat, a handlebar, and a transmission system, which turns the muscular effort of the driver into movement of the wheels [1].

Throughout history, the bicycle has changed several times implementing various functional, comforting, safety and even efficiency innovations, such as the gear shifting system. This system is incorporated in the transmission assembly to transform the energy provided by the traveler into speed or torque, depending on the features of the journey [2].

A common gearing system, used in many of today's bikes, is the derailleur-type external gearing. However, and not limited to the bikes, there are different proposal mechanisms for the energy optimization. The variety of vehicles, and their relationship in the context of usage, open up to several design options.

GOALS

This project will be based on the design process of a bicycle gearing system. Its features and the kind of bike used as reference, will be defined throughout the project.

As concerns to the development of the project, the following results are expected:

1. Previous research focused on the state of the art of transmission systems and models of bicycles.

2. Justification and complete definition of the proposal selection. This must accomplish two requirements: a functional improvement in relation to precedent models and the integration of the different systems studied during the research.

3. Complete design process of the product supported by calculations and simulations and explanatory elements.

4. Dimensional and visual definition of the final proposal, by means of 3D modelling and drawing software.

METHODOLOGY

Aside the previous research and the definition of the proposal, the design process will be divided in the different groups of parts and will follow the following method for every of them:

1. First, every part will be modelled by 3D software, defining the dimensions of the elements and the distribution of forces along the assembly.

2. Next, the free body diagrams of the parts will be analyzed and solved by the required equilibrium equations.

3. Then, every part will be studied for the static and dynamic mechanical performance. This would include the comparison of different materials and the definition of their safety factors.

4. Once every part is theoretically verified and modified to accomplish a proper safety factor, the 3D model is used to simulate and check the element works as expected. If the parts fail, they will also be modified, calculated, and simulated again until it gets to work correctly. As a correct safety factor, a 1.4 minimum value will be considered.

5. Finally, the plans will be drawn, for every part and the assembly of the final design.

1. HISTORY AND STATE OF THE ART

The modern bicycle used nowadays is the result of a two-century long development, during which several changes and improvements have been implemented in order to guarantee an optimal performance and the maximum safety for the driver.

Prior to the conception of the design to be proposed, an investigation will be carried out about the history and state of the art of the bicycle. From this, you will be able to understand the different mechanisms and components that are part of a bicycle to finally choose the most appropriate or interesting design.

In addition, the aspects related to the assembly and operation of the proposal will depend on the type of bicycle chosen as a reference and, therefore, its different possibilities will also be studied.

1.1. DEVELOPING THE BICYCLE

The exact invention of the bicycle is still debated: due to the lack of clarity as to the characteristics that should define it, it is difficult to identify the first prototype or model of bicycle. Probably, the most correct thing is to understand it as the result of the different contributions of several inventors.

The model introduced in 1817 by Von Drais establishes a consensus regarding the first two-wheeled rider-propelled machine. This product, named "the running machine", was made of wood and had to be driven either by the paddling of the rider's feet [3].

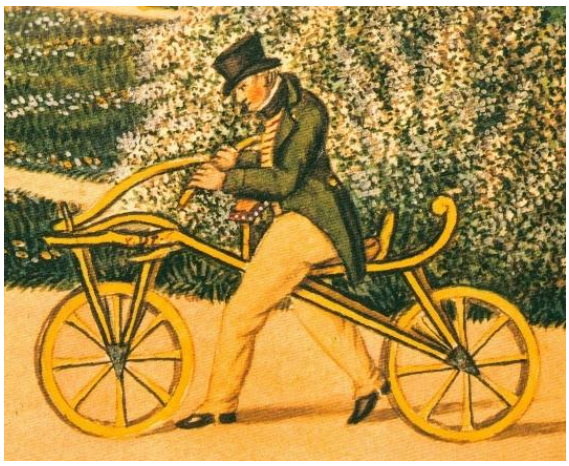

figure 1. The "running machine" invented by Karl Von Drais in 1817. Source: [4]

From Von Drais' invention, different copies of the design appeared. Denis Johnson presented the "pedestrian curricle", which implemented improvements regarding the dimensions and geometries of the structure. These designs were expensive and too uncomfortable to be driven, failing commercially. However, these set proof that the bike was able to balance during movement [3].

Figure 2. The "pedestrian curricle" invented by Denis Johnson in 1819. Source: [5]

The first major change in the invention of the bicycle is the integration of pedals. The advantage of these mechanisms lies in greater comfort and fluidity during the rotation of the pedals, compared to the violent and uncomfortable movements of the paddling. In 1839, Kirkpatrick Macmillan invented the first mechanically driven machine, which used pedals connected to the rear wheel axle. Due to its high weight, it required considerable physical effort to be driven but could be considered a precursor to indirect driving [6].

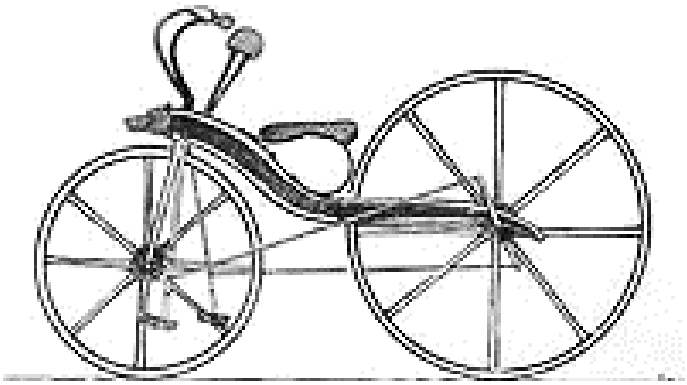

Figure 3. First mechanically driven bicycle invented by Kirkpatrick Macmillan in 1839. Source: [6]

Later, during the 1860s, different characters would work on modifications of the bicycle design with pedals. Mainly, the transmission connected to the rear wheel is changed by a crank, with two pedals, mounted on the axle of the front wheel. This design allows the mechanism to be optimized by reducing the transmission distance, since the driver applies the power directly to the wheel axle. In addition, a new design standard was established to adapt it to mass production: malleable cast steel was applied for the production, in large series, of the structural frame [7].

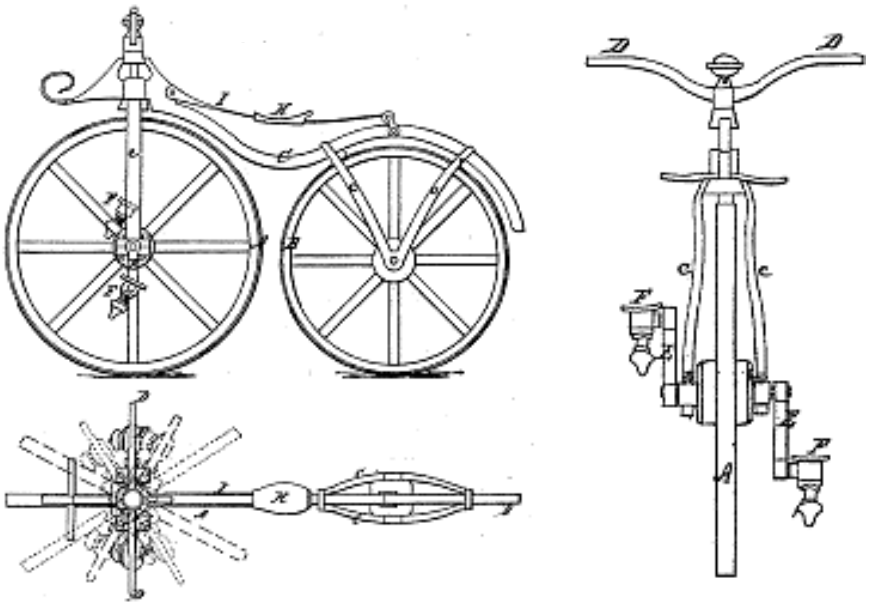

Figure 4. Pierre Lallement's patent of a pedaling system applied to a Draisienne. Source: [7]

Before 1860, cycling racing began to gain popularity, causing an increase in demand for speed-focused designs. As the direct drive was limited to a speed ratio of 1, the search for higher speed was directed towards raising the diameter of the drive wheel. A larger diameter wheel moves linearly a greater distance for each revolution. The manufacture of wheels of this size was only possible after the introduction of tension spokes by Eugine Meyer in 1869. In addition, wheels with spokes work with traction instead of compression, avoiding buckling problems [7, 8].

The new design possibility led the industry towards the invention of the high-wheel bicycle, also called "penny-farthing", which consisted of a diametrically larger front wheel. These were very popular during the 70s and 80s but, nevertheless, they were considered dangerous due to the frequency in which accidents occurred due to falls over the handlebars. In addition, the large front wheel caused handling problems on its own. As a result, many bike designers began to focus on creating safer bikes [3].

Figure 5. The "Ariel" high-wheel bicycle invented by James Starley in 1870. Source: [9]

The same year that tension cables appeared, the freewheel ratchet system was invented by William Van Anden. This mechanism consisted of installing a ratchet in the coupling between the pedals and the wheel axis, allowing it to rotate freely while not pedaling. Although currently its use has been limited to single-speed bicycles and models with cheaper gears, the freewheel can be considered the predecessor of the freehub system, widely used today for bicycles with several gears [9].

Already in the early 1870s, the technology and use of the bicycle had developed considerably. The structural frame of steel pipes, the highest quality bearings, wheels formed by steel rings, tensioning cables and rigid rubber tires, and standardized components, had become common in the industry. Using these possibilities, James Starley introduced "Ariel", the design which would become the standard of high-wheel bicycle [3].

THE TRANSMISSION SYSTEM

At this point, the next key step in the development of the bicycle known today is the implementation of indirect riding. This system allows the pedals to be placed on a different axis from the wheel, since it is responsible for transmitting the power between the two points. This transmission can be achieved in different ways: the use of gears, belts and pulleys or the shaft drive are good examples, but the most used and known today is the transmission by pinion and chain [7].

Figure 6. Transmission system examples. Left: Chain transmission; Center: Belt transmission; Right: Shaft transmission. Source: [2].

Although the belt reduces and facilitates maintenance, and the shaft transmission makes driving safer by keeping the mechanism enclosed, the chain and pinion system has always maintained the advantage in terms of efficiency and strength. However, technological development has led to the emergence of very valid options of each type [10, 11].

Figure 7. The "biciclette" invented by Henry John Lawson in 1879. Source: [9]

Around 1860, several safety bicycle patents were developed based on the chain drive. Early designs incorporated an amplifier single-speed, allowing smaller wheels to be used. The "biciclette" design, introduced by Henry John Lawson in 1879, used a rear transmission and can be considered the midpoint between the "penny-farthing" and the safety bicycle [7, 9].

In 1880, the roller chain patented by Hans Renolds became the commercial standard for bicycle manufacturing. Later, in 1885, John Kemp Starley would introduce the "rover safety", being considered the most successful and the first prototype of a modern bicycle [9, 12].

Figure 8. The "rover" safety bicycle invented by John Kemp Starley in 1885. Source: [13]

THE GEAR SHIFTING SYSTEM

The single-speed of the bicycles developed by Lawson and Kemp, among others, allows to transform the pedaling speed into a greater speed of rotation of the wheels, a requirement highly demanded for the competition. This system was very limited for other uses: on ascending slopes or to start driving it is more recommendable to use reducing gears, to facilitate pedaling.

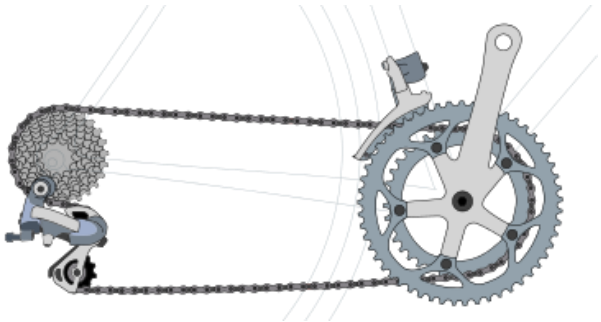

Figure 9. External shifting system illustration. Source: [21].

Based on the chain drive, different gear shift system designs appeared during the 1890s. These used the derailleur, which allowed the chain to be untensioned, moved and re-tensioned to engage it on sprockets of different dimensions. As with previous innovations, the discussion about who invented this system is inconclusive. In 1896, Edmund Hugh Hodgkinson patented a 3-speed transmission, considered one of the precursors of the modern derailleur [9, 14].

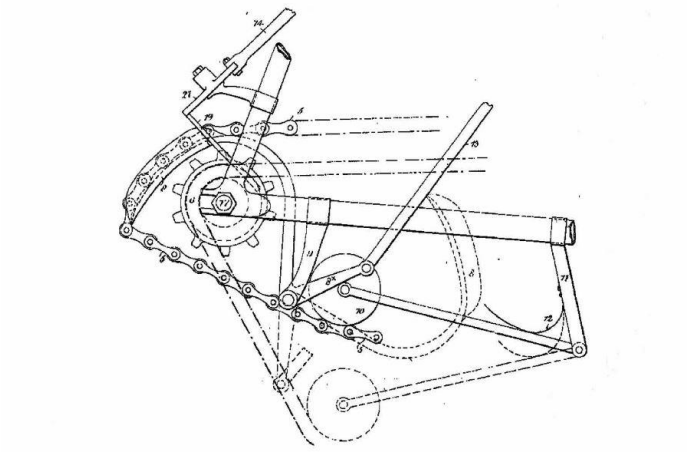

Figure 10. The “gradient” derailleur patented by Edmung Hugh Hodgkinson in 1896. Source: [15]

Nowadays, the derailleur shifting is the most used system because it offers a wide variety of speed combinations. In addition, the little space occupied by the sprockets and the chain, make it a comfortable and light system for driving. However, it is not perfect: the maintenance of the pages is strict and fundamental for their correct operation and could become dangerous due to the mechanical elements that are not covered.

On the other hand, the activation of the derailleur was made depending on the model. Most designs used rod-type selectors, such as the dual-rod "cambio corsa", marketed by Campanolo in 1946. Later, the indexed selector, which used a tensioning cable and a lever, was introduced by Hercules Herailleur. The last one has been developed, together with the derailleur, to be the most common transmission system currently in bicycles [9, 16].

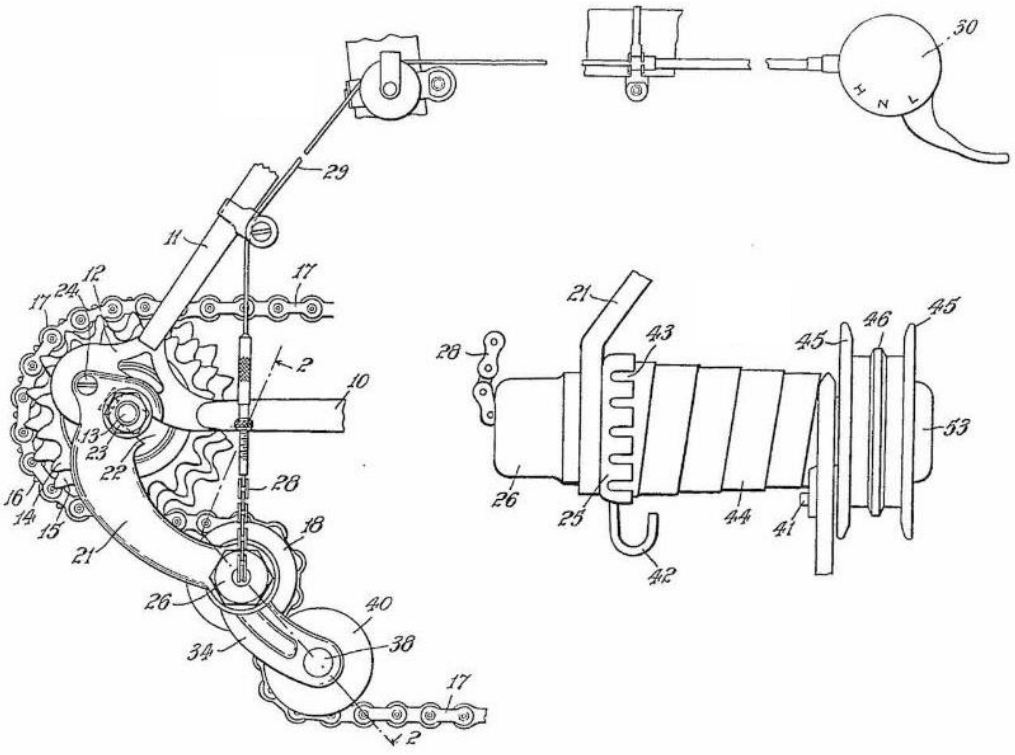

Figure 11. “Hercules Herailleur” invented by Thomas Alfred Yapp in 1949. Souce: [16]

In parallel, during the last decades of the nineteenth century, several patents for internal gearing hub were presented as an alternative to the popular derailleur. These mechanisms use a planetary set of gears and are installed on the axis of the drive wheel, being protected inside the hub [9].

The interest of this mechanism lies in the fact that it is not limited to chain transmission, since it is not directly integrated into it. Contrary to the derailleur set, internal gearing hub have a longer service life and require less strict maintenance.

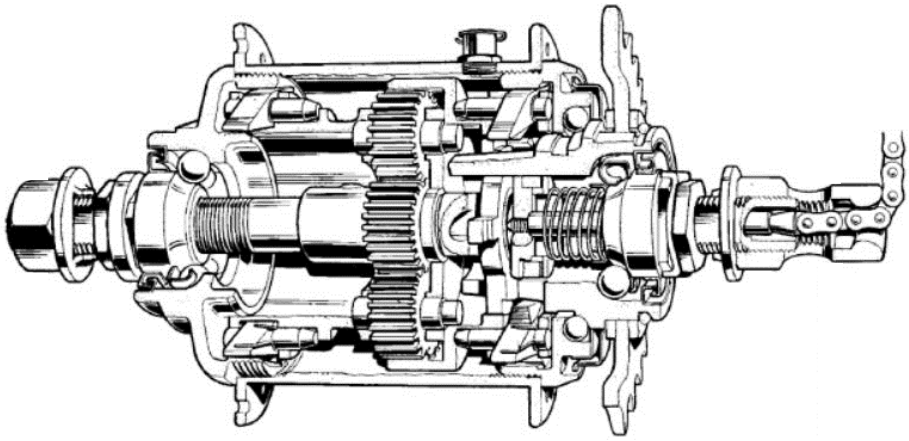

Figure 12. 3-speed internal gearing hub produced by Sturmey Archer in 1902. Source: [17]

In 1896, William Riley patented the first internal gearing hub with 2 speeds, which was a great commercial success. Its 3-speed version would be produced by Sturmey Archer in 1902 [9].

The internal transmission, which uses epicyclic gears, can set different configurations to vary its operation, granting different design possibilities according to the requirements of use of the mechanism. The 3-speed Sturmie Archer gearbox uses a solar gear, several planet gears, mounted on a planet carrier, and a ring gear. While using the sun as the central part of the rear wheel, fixed on the frame of the bicycle, the other elements allow for engaging the 3 speeds.

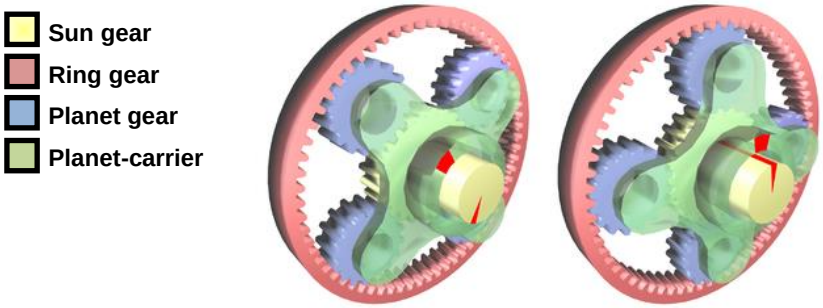

Figure 13. Epicyclic mechanism elements. Source: Own elaboration.

1.2. TYPES OF BICYCLES

In the world of bicycles there is a wide variety of models. The different requirements of use and innovation in designs allow for offering very differentiated products, while still being based on the common bicycle developed during the last centuries.

Depending on the scenario and the use given to the bicycle, 3 groups can be differentiated: road bikes, urban bicycles, and mountain bikes. The variety of models is not only limited to this classification but allows for understanding, in general terms, what are the main functions of interest of each one. In addition, some bicycles could belong to 2 groups at the time, since many applications require their use in different scenarios.

THE ROAD BICYCLE [18]

This type of bicycles is the most used for cycling sports, since they are designed to reach the highest possible speed: by minimizing the weight and volume occupied by the bicycle, aerodynamics is increased.

In addition, elements such as the handlebars, saddle and pedals are located in specific positions to ensure an optimal riding posture to reduce wind resistance. Also, the tires they use are thin, designed to reduce rolling resistance.

Figure 14. Example of road bicycle. Source: [18].

In sports such as triathlon, the geometry of the bicycle is adapted to help the driver to promote rest and avoid fatigue caused by swimming and subsequent running. It also allows the transport of some assistance resources such as spare parts or drinks.

Another type of road bike is the fixie, which uses a fixed single-speed transmission mechanism that can only be braked by offering resistance to the rotation of the pedals. This has the characteristics of a road bike, but it is known that its use is popular in cities.

THE URBAN BICYCLE [18]

Urban bicycles are designed to be driven at less strict speeds and to ensure the comfort and safety of the driver throughout the city.

The design of the structural frame is usually quite robust and is prepared for a less strict driving posture. On the other hand, the urban bicycle usually incorporates different

accessories useful for the driver such as baskets or headlights, and safety accessories such as mudguards and chainguards.

Nowadays some touring bike designs can even be folded for easy storage or transport while not in use. Others incorporate two rear wheels, between which a carrier is placed.

Figure 15. Example of urban bicycle. Source: [18].

THE MOUNTAIN BICYCLE [18]

These bikes are designed to be ridden in mountainous areas, reducing the adverse effects caused by uneven surfaces.

The most remarkable feature of these is the use of different suspension systems, which absorb the impact produced by the terrain. As for the tires, these are usually thicker and use studs or a more pronounced tread to improve grip.

Depending on the activity to be performed, mountain bikes have different types of suspension or tires. To travel soft terrain covered with snow or mud, fatbikes use tires of considerably greater thickness, while downhill bikes, or enduro, use more resistant suspensions that allow to withstand the high speeds and impacts generated in this discipline.

Figure 16. Example of mountain bicycle with double suspension. Source [19].

ELECTRIC BICYCLES (E-BIKES) [20, 21]

The electric bicycle cannot really be considered another distinct group, since it would correspond to another classification. However, technological progress has caused the revolution of the electrical system with respect to the conventional one, so it is necessary to understand its characteristics.

Figure 17. Example of electric bicycle. Source [19].

There are two types of electric bicycles depending on whether they offer a certain amount of power when pedaling or if they directly supply all the required energy. The pedal assist bike uses an electric motor which operates comfortably at high speeds at which it circulates most of the time. At low speeds, as in the case of a slope, it costs them more to circulate, if the engine is not very powerful, so it is necessary to equip them with several speed gears. In some cases, only a amplifier single-speed is used, limiting the use of the electric bicycle to roads with reduced slopes [20].

Some manufacturers include a high-powered engine or a throttle to offer an extra boost capable of climbing the slope. These elements can also be used to deliver all the power required during riding, giving rise to the direct supply bike. Since the European legislation that allows an electric bicycle to be homologated defines a maximum speed of 25 km/h, these alternatives sometimes exceed it [20, 21].

1.3. GEAR SHIFTING SYSTEM

When talking about the gearbox it is more common to think of the speed system of the car's transmission before any other machine. In particular, combustion vehicles use a good variety of gear changes, starting with the distinction between manual and automatic transmissions.

In order to understand the different designs and technologies applied to combustion vehicles, the different gearboxes that they can integrate will be explained below.

1.3.1. MANUAL GEARBOX

The manual gearbox consists in the transmission mechanism of the vehicle which does require an activation action from the driver to configure manually the working gears [22].

An optimal gearbox is essential for combustion engine vehicles. Due to the power limitations of the engine, the vehicle is unable to adjust to the road conditions in an efficient and safe way. The manual shifting system allows for turning the same rotational speed from the motor into various output speeds and torques in the driving wheels [23].

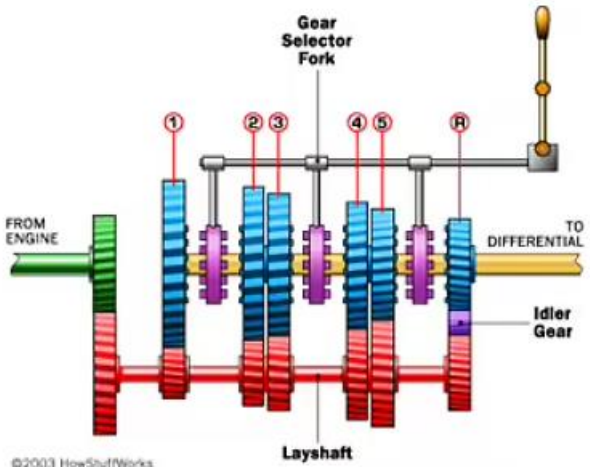

Figure 18. Manual transmission with 5 forward speeds. Source: [24]

Their main advantages, in contrast to automatic vehicles, are the lower prices and a better performance in terms of efficiency. These features have kept the manual vehicles as a shifting system standard. Even so, the innovation in electronics and automation have made possible the development of automatic gearbox with better features [25].

The manual mechanism is based on the movement transmission through several gears arranged on three shafts. The gears commonly are the fixed type, what means that they cannot slide to couple to the shaft. However, they use a sliding ring which connects to the pertinent gear by “dog teeth”.

Generally, the manual shifting system provides an average of 5 speeds, besides the reverse speed. Depending on the vehicle they could be some more or less.

SYNCHRONIZER MANUAL TRANSMISSION

Within manual shifts, the synchronizer systems are the most used. This technology solves a problem produced in the output shaft: if the “dog teeth” contact with the gear, but both are spinning at different speeds, the teeth will not couple, and a violent grinding noise will be generated [25].

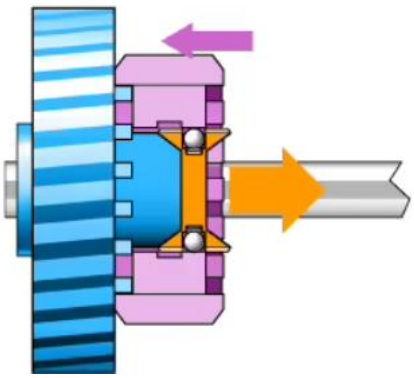

Figure 19. *Synchromesh* working system illustration. Source [24].

Synchromesh technology permits to coordinate both speeds from the output shaft and the engaged gear so that the “dog teeth” connects correctly. Before the coupling, a friction clutch, located in the inner ring, makes contact, and carries by friction the movement the output shaft, adjusting its speed to the speed of the gear.

NON-SYNCHRONOUS TRANSMISSION

This system needs the driver to manually adjust the input speed to the output speed. The non-synchronous designs are simpler but require great skills for the clutchless driving.

Because of the comparison with the synchronized transmission, the usage of non-synchronous systems has been restricted almost totally to tractors, trailers, and other heavy-weight vehicles [26].

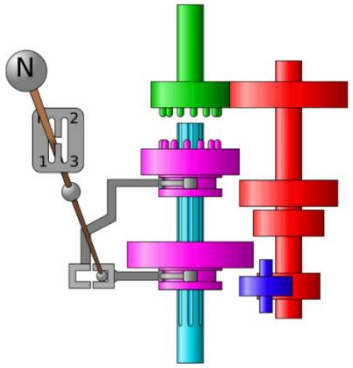

Figure 20. Non-synchronous transmission with 3 forward speeds. Source: [26].

SEQUENTIAL MANUAL TRANSMISSION

Non-synchronous manual transmission is also applied to motorcycles, *quads*, and specific vehicles (racing cars or sport-utility vehicles). These utilizes a particular system called sequential manual transmission [27].

In terms of design, this mechanism makes use of a ratchet that activates the movement of a selector drum, which has three or four machined tracks around its circumference. These tracks connect to the selector forks and guide them to engage the required gear [28, 29].

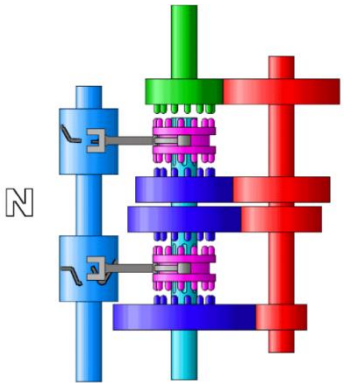

Figure 21. Sequential manual transmission with 4 forward speeds. Source: [27].

The sequential transmission implies faster shifting lapses and higher assurance in the selection, than the rest of the manual transmissions. On the other hand, it also implies a limitation in the deliberate speed selection, a lower durability, and a more demanding maintenance. Therefore, they are only used for motorcycle and competition vehicles [27].

1.3.2. AUTOMATIC GEARBOX

An automatic system handles itself the gear shifting process to make the speed of the vehicle change. The main advantage of these mechanisms is that the driver is liberated from the clutch control tasks and the manual shifting [30, 31].

In the past, the automatic shifts had worse features in relation to the manual systems. However, nowadays, latest automatic mechanisms have reached better characteristics. Moreover, the development of electric vehicles, which offer less limited values of power, and the autonomous driving innovations make the automatic shift necessary [24].

AUTOMATED MANUAL TRANSMISSION (AMT)

It is based on the mechanic design of the common manual transmission, although the clutch and the shifting system are controlled by a computer. AMTs are slow and abrupt mechanisms since they are still in development, but they are affordable choices to dispense with the clutch pedal [32].

Although it is considered a differentiated type of automatic transmission, it can be found that the other examples also use automated components in a similar way.

DOUBLE CLUTCH TRANSMISSION (DCT)

This system keeps a design similar to the common manual transmissions, but it has two transmission shafts, each of them with its own clutch working independently [33].

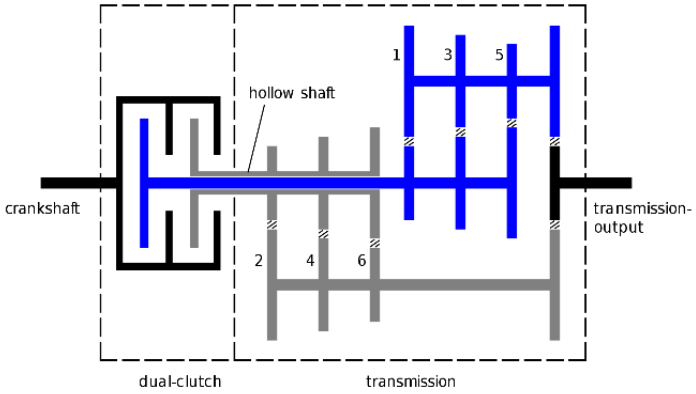

Figure 22. Double clutch transmission illustration. Source: [33].

Its working principle is to alternate the connection of each shaft while engaging the pertinent gear. The first shaft connected carries the odd gears and the other carries the even ones. Unlike the manual transmission, the control of the engaged gears is conducted by electronic and hydraulic devices.

The main advantage of DCT is the shifting speed since one shaft is ready to be coupled before the other gets disconnected. In the other hand, the main weak point is the higher prices [32].

HIDRAULIC AUTOMATIC TRANSMISSION

This is the most common automatic shift, which utilizes a torque convertor as an automatic clutch system. This mechanism is based in a planetary gearbox, and electronic and hydraulic monitoring [32].

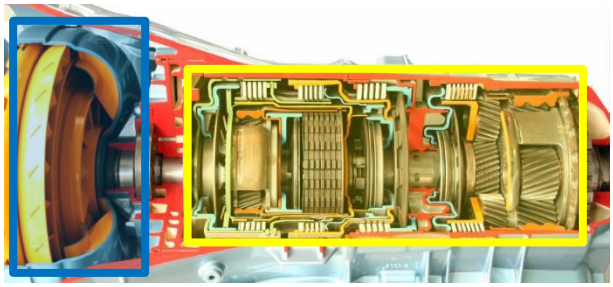

Figure 23. Hydraulic transmission elements. Blue: torque convertor; Yellow: planetary gearbox. Source: [30].

Hydraulic transmissions appeared as a not much competitive automatic technology, in relation to manual systems, but nowadays their working speed and tenderness have been quite raised [34].

CONTINUOUSLY VARIABLE TRANSMISSION (CVT)

CVT allows for shifting to any ratio value between its limits. It commonly uses 2 variable diameter pulleys connected by a belt, and an automatic clutch system [35].

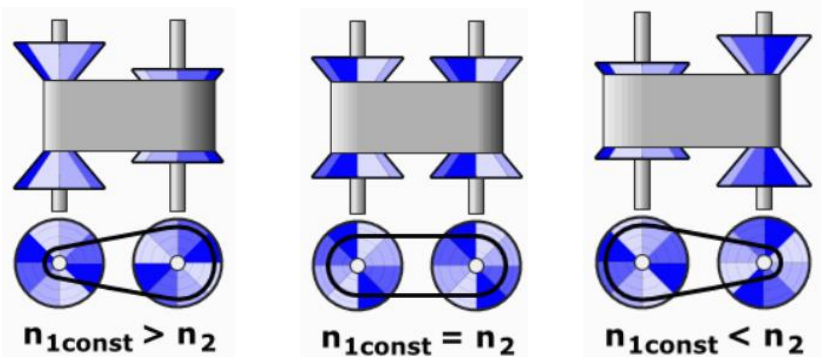

Figure 24. Working stages of the continuous variation. Source: [35].

This system is mainly used for *scooters*, surely because of its usefulness for driving through urban areas. As an advantage, CVT is an uninterrupted transmission which offers a very smooth and comfortable performance, in addition to its high efficiency [36, 37].

1.4. OVERVIEW

To conclude, two clear trends have been identified in the design of shift mechanisms for bicycles. The most commonly used is the derailleur system, while internal gearing hubs can be found on some bikes designed with a particular focus.

The following table defines the differences between these two systems, as well as the advantages and disadvantages of each. In general terms, the two systems are very different according to the type of use given to the bicycle. The design of the derailleur focuses on the stricter and more competitive use of the vehicle, while the internal transmission offers features more focused on comfort, safety, and longer service life.

GEAR SHIFTING SYSTEM	External derailleur	Internal gearing hub
Transmission compatibility	Chain and belt	Chain, belt and shaft
Bicycle models	Road and competition	Urban and touring
Strengths	Most popular Great resistance High variability of speeds	Hermetic and safe assembly Less maintanence Shift while pedalling
Weaknesses	Excessive maintenance Risk of entanglement	Mechanically more complex Lower speed varibility Heavier assembly

Table 1. Comparison of gearing systems. Source: Own elaboration.

As a relevant characteristic, internal gearing hubs are defined as more complex assemblies, given the operation of the epicyclic gears and the number of parts that this contains. Taking into account that, below, different design proposals will be developed about the type of product chosen, the internal change turns out to be more interesting for the process of ideation. Specifically, the original 3-speed Sturmey Archer design is very interesting, which is still used residually by some enthusiasts.

Additionally, the research has also studied different gearing mechanisms used in motor vehicles. Although the proposals will focus on the internal hub for bicycles, these designs will serve to give a broader perspective of ideas to integrate.

2. DESIGN DEFINITION

In the following section, the ideas obtained from the 3-speed gearing hub, and from the different concepts studied during the research, are explained. From these, the required aspects of the design are developed and, as well as the reasons why they are discarded or selected as the final proposal.

Among the requirements that the proposal must accomplish, the design is expected to imply a functional improvement in the product, considering that it is a system focused mainly on the comfort and safety of the driver. In addition, it is expected to implement several of the systems studied during the information research. These elements must be compatible in order to develop a viable and coherent proposal.

2.1. PROPOSAL 1

First, the possibility of adapting the transmission with internal gearing hub to the operation of the electric bicycle is raised, specifically those with a power motor lower than 250 watts, and without accelerator. Since they are limited during driving on high slopes, it is necessary to equip them with a reductor gears system, which allows for transmitting greater torque to the wheels.

As explained above, the 3-speed gearbox uses a solar gear, several planet gears, mounted on a planet carrier, and a ring gear. Using the sun as the central part of the rear wheel, fixed on the frame of the bicycle, the other elements allow for using the 3 speeds.

Although the use of only one solar gear and one ring gear is very common in transmissions using the planetary system, this configuration is not the only one. It is possible to use 2 pieces of the same type, sun or ring, as long as they engage with planets of different section. Otherwise, the number of effective gears would be reduced by one. That is to say, as both planets have coincident diameter, they work just like a single planet.

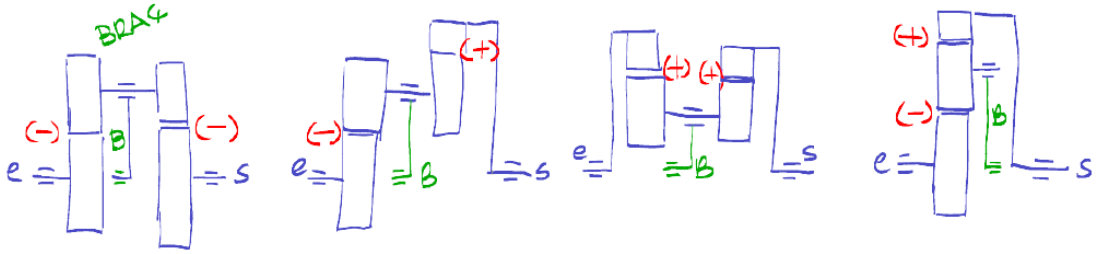

Figure 25. Basic planetary types. Source: [38].

On design terms, the use of the solar gear as a fixed element, assembled to the structure of the bicycle, is the most intuitive. However, it is not strict for the operation of the planetarium either. Theoretically, both the ring and the planet-carrier could serve as a fixed element, giving rise to a higher variety of possible mechanisms.

For the proposed design, it is necessary to study a new configuration that has 2 different gears and dispense with the amplifier gear. However, one of the main properties of the planetary mechanism is the speed ratio, defined for each gear by the following formulas.

Lower speed: $i_1 = \frac{R}{S+R}$ [f.1]

Direct speed: $i_2 = 1$

Higher speed: $i_3 = \frac{S+R}{R}$ [f.2]

$R - Number\ of\ teeth\ of\ the\ ring\ gear.$
$S - Number\ of\ teeth\ of\ the\ ring\ sun\ gear.$
$These\ formulas\ are\ also\ valid\ if\ the\ variables\ are\ used\ as\ the\ pitch\ diameter.$

As followed by the formulas [f.1] and [f.2], the lower gear and the higher gear have inverse values, one corresponding to the reduction and the other to the speed amplification. Taking this behavior into account, it is gathered that is not possible to design such a planetarium with 2 reducing speeds. This conclusion can also be extended to the different configurations of planetarium: all of them, in addition to their particularities, have this speed ratio arrangement.

$$i_1 = 1/i_3 \qquad [f.3]$$

2.2. PROPOSAL 2

On the other hand, there are models of electric bicycles that are limited to using a single-speed transmission, commonly amplifier. As explained, this gear is more suitable to be used at high speeds on regular terrain without slope, or with a downward slope. These models are designed exclusively for these conditions, offering a more relaxed and smooth drive.

As an alternative proposal, the incorporation of the internal gearing hub system to the bicycle with amplifier single-speed is suggested. As the planetarium used already integrates an amplification gear, the single-speed transmission can be replaced by a direct transmission.

In summary, the resulting mechanism would be based on a direct transmission $(i = 1)$ connected to the internal gearing hub, which uses the amplification gear for the start of the riding, equivalent to the amplifier single-speed. Additionally, the direct and reducing gears of the internal change are activated to offer greater impulse as the slopes are more inclined.

The integration of this mechanism in the electric bicycle with single-speed involves different modifications of the transmission elements. Bicycles marketed with these characteristics use specific components that adapt to the operation of the single-speed.

Instead of using chain drive, these models take advantage of the lack of axial movements in the transmission, replacing it with the belt. This system is not compatible with external changes but with the planetary mechanism of internal change. In addition, the development of new technologies and materials has allowed the manufacture of high-

quality belts, equating them to the chain. This combined with certain advantages such as the reduction in noise generated or the required maintenance, make the belt drive an ideal choice for a single-speed bike. Under this condition, the design would involve a redesign of the sprocket to be able to engage the serrated belt.

On the other hand, the single-speed electric bicycle uses a rear electric motor, which is designed to be mounted on the rear wheel hub. This position of the engine is incompatible with the internal gearing hub, previously defined since they should occupy the same location on the bicycle.

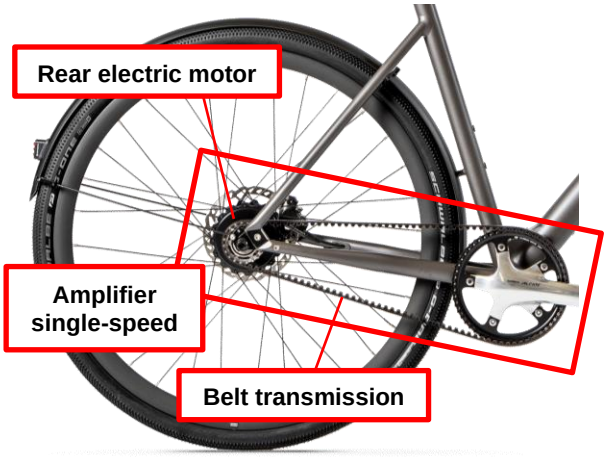

Figure 26. Single-speed electric bike transmission. Source: [39].

Therefore, to integrate the planetary mechanism to the system, it would be necessary to apply one of the following options: to modify the entire motor assembly, combining the two components in the same location, or to redesign the internal change to place it as part of the pedal axle.

Since both options would increase the complexity of the design, this proposal does not adapt to the requirement set as the objective of the project. In conclusion, the proposed integration of the internal gearing hub to an electric bicycle is discarded, and finally a common mechanical bicycle will be used for the development of the project.

2.3. PROPOSAL 3

Leaving aside the electric bicycle, internal changes are considered a good alternative to external transmission. The comfort and safety that characterizes them make them an ideal mechanism for urban bicycles, touring, or other models designed for driving conditions without high demand.

Specifically, the *AW 3-speed gear* from Sturmey Archer, was the first model of this type to be marketed successfully, and today is considered one of the main references in terms of its design. The integration of the planetary assembly to the transmission of the bicycle, complemented by the clutch and speed selection mechanisms, offered great functionality and robustness. However, after a prolonged use, some products ended up with failures in the speed selector system.

This mechanism is operated by a tensioning cable and a compression spring, which are connected to the clutch part to move it through its different positions. Once this piece is

in the correct position, it is held only by the balance of forces applied by the cable and the spring.

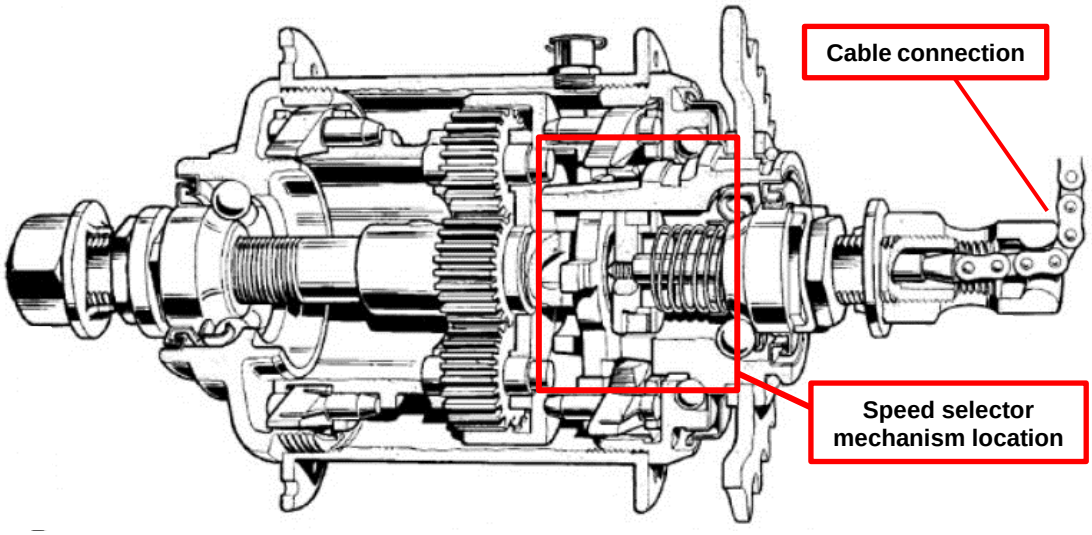

Figure 27. Clutch and speed selection system located inside the clutch mechanism.

Source: own elaboration from [17].

To ensure the correct performance of the mechanism, the tensioning cable must be mounted and adjusted with great precision. Otherwise, it is very likely that errors will occur when selecting the gears. An adequate quality control process allows to avoid this type of situation; however, the same problem frequently appears after several cycles of use of the product as a result of the loss of tension of the cable and, ultimately, due to the lack of a lock mechanism for each running position [40].

In order to correct this error, it is proposed to define a new design of speed selector system, which should include a locking mechanism to avoid incorrect displacement of the sliding clutch.

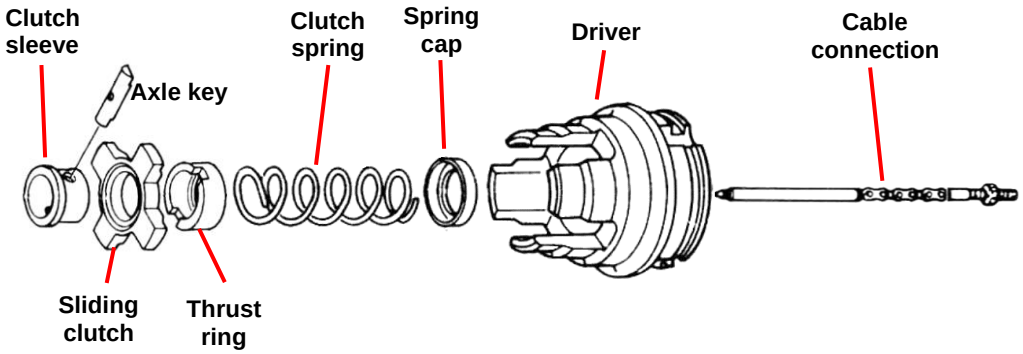

Figure 28. Clutch and speed selection parts. Source: own elaboration from [17].

The first ideas considered is based on the integration of a selector drum. The selector drum is one of the elements integrated in the gearbox of some vehicles with sequential transmission. This mechanism allows the controlled movement of the selector lever, activated by the driver, to be translated into an axial displacement of the forks that engage the gears. The drum, as a transmission element, takes the rotation of the lever and, by means of a series of superficial notches, pushes the forks to the position

corresponding to each speed [28].

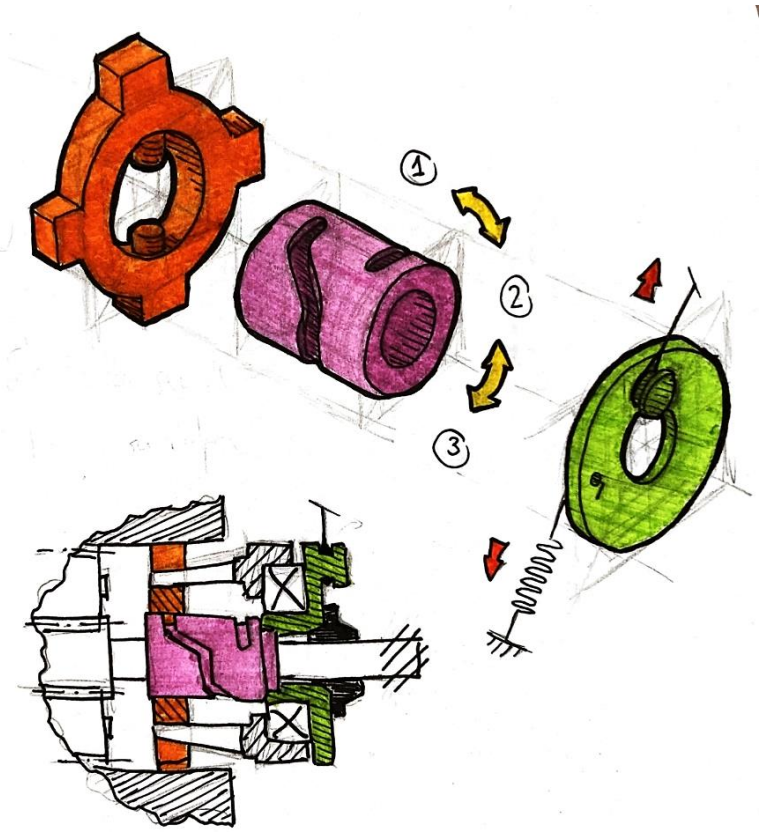

Figure 29. Explanatory drawings of the selector drum proposal. Source: own elaboration.

In the case of internal transmission, the drum would be placed in the hole of the sliding clutch, inside the driver, and would be connected from the outside by a spring and the tensioning cable. In any case, this proposal is finally discarded because doubts arise about whether the displacement of the star through the notches is totally viable.

However, the motorcycle's selector system integrates different elements into its assembly. To control the rotation of the drum, and to avoid improper displacement of the forks, the transmission includes a ratchet mechanism. This is responsible for transforming the small movements of the lever in the rotation of the selector drum to the required position. As the angular position of the drum is restricted by the ratchet teeth, the working gears remain locked.

Figure 30. Explanatory pictures of the ratchet mechanism of a selector drum. Source: [41].

From the ratchet concept, arises a new proposal based on a crank-rod-piston type mechanism, where the indicator rod fulfills the function of piston and the selector drum as the crank. Its rotation will be limited to three positions by a ratchet part, which will engage and activate the required speed.

This new assembly will be coupled to the side of the shaft, entering through the bored access to the clutch. Therefore, the proposal does not require the modification or deletion of any internal element of the internal change. Only the indicator rod part will be redesigned so that it can connect both mechanisms.

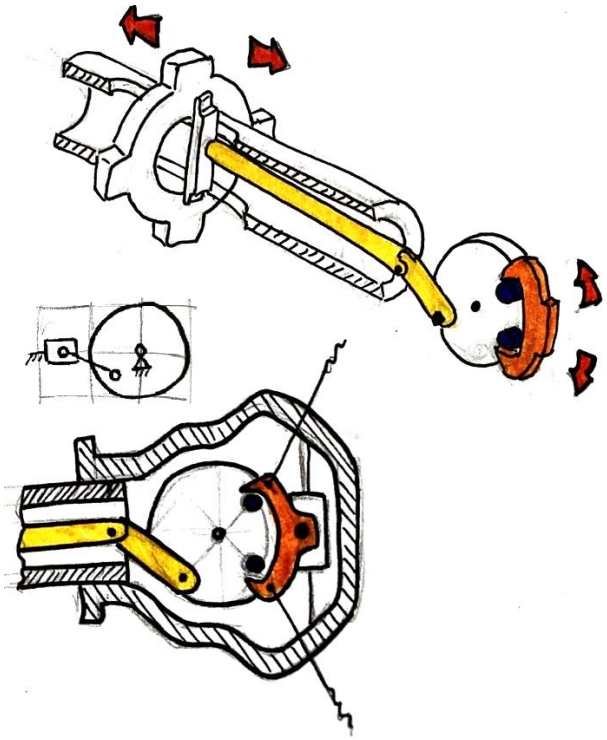

Figure 31. Explanatory drawings of the selector ratchet proposal. Source: own elaboration.

As for the cable connection, the direct transmission to the indicator rod will be eliminated and the actuation system will be connected to the ratchet part. Since the ratchet must be able to be activated in both directions, the system will be connected by two cables which will be mounted oppositely to the moving part.

The defined mechanism also requires the use of elements such as springs, bearings, and screws. The features of these parts, the materials used, and other technical aspects of the proposal will be defined as a section of the mechanical design, developed below.

2.4. PROPOSED SOLUTION

As explained, only one of the proposals completely fulfills the requirements stablished initially. The proposed redesign of the selector clutch system integrates both the selector drum and the ratchet system, which are components of the sequential manual transmission studied in the previous research section. Furthermore, the proposal focuses on solving the troubleshooting, which generates problems during the speed shift operation.

Regarding the rejected proposals, although the integration of the internal hub in the system of an electric bicycle aims to adapt the internal system for a more optimal operation, it has been concluded that these two elements have poorly compatible designs.

Regarding the rejected proposals, although the internal change and the electric bicycle are elements that can be combined to give interesting results, they are formed by incompatible designs, as concluded above.

3. MECHANICAL DESIGN AND SIMULATIONS

The following sections describe the design process of the parts and the decisions made regarding the technical aspects of the proposal, supported by drawings, explanatory schemes, calculations, and simulations.

3.1. TECHNICAL ASPECTS OF THE PROPOSAL

The internal gearing hub uses the central axle, assembled to the bicycle, as structural support to assemble the rest of the parts. This, in addition to the frame, can be considered the bench of the assembly. The machined $M10$ threads at each end of the shaft allow the mounting of nuts, washers or other auxiliary elements used to fix it on the bicycle bench.

The assembly of the design will be done in order, first connecting the indicator rod with the clutch mechanism, through the side bore, and then isolating the rest of the assembly inside a case. This case must finally be fixed on the threaded shaft.

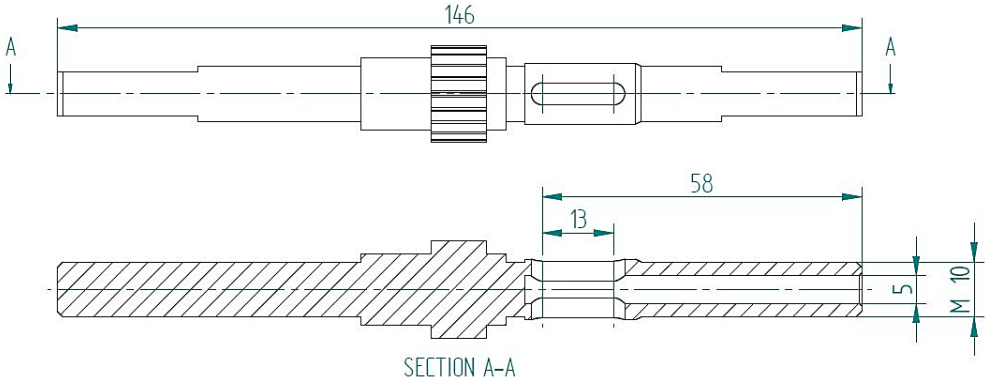

Figure 32. Dimensions of the central axle of the AW -3speed gearing hub. Source: own elaboration.

According to the dimensions of manufacture of this product, the shaft can be found with a $146\,mm$ length, although there is a discontinued $159\,mm$ model. On the other hand, the free width between the rear forks of the bike depends on the model. This measurement can take two values: $142\,mm$ and $148\,mm$; and therefore, the shaft is not long enough. Since the variety of axles is high, the design process will focus on the original $146\,mm$ long shaft, considering that for other models the dimensions will have to be adapted [42, 43, 44].

As shown in figure 32, the maximum travel of the clutch pin is $13\,mm$, or $6.5\,mm$ from each speed to the next one. Moreover, the distance from the pin in the amplifier position, with respect to the end of the shaft is $58\,mm$ and, together with the $5\,mm$ diameter of the bore, they are relevant measurements for the design of the indicator rod.

On the other hand, a problem arises in the design of the crank-rod-piston mechanism: taking as reference the second speed, corresponding to the midpoint of the travel of the indicator rod, this should be moved $6.5\,mm$ each direction, to activate the other speeds.

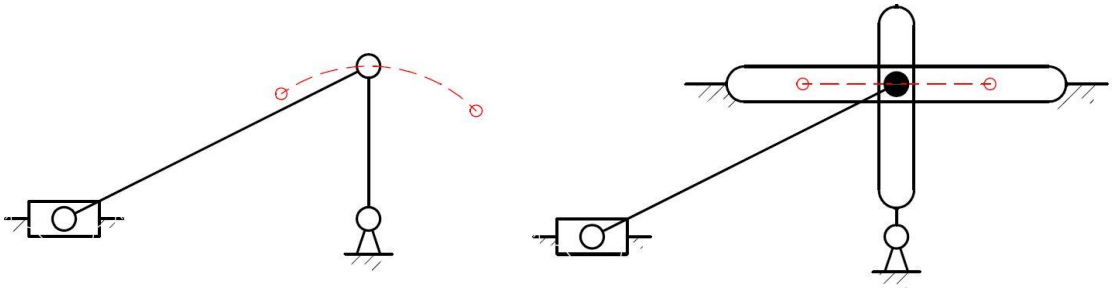

Figure 33. Crank-rod-piston mechanism variations. Source: own elaboration.

Due to the geometry of the mechanism, for the displacement condition to be achieved, the crank part must rotate at different angles in each direction, defining an asymmetrical trajectory. Such asymmetry complicates the design of the ratchet part, making it ineffective. Figure 33 shows this problem, along with the solution adopted.

Instead of connecting rod and crank through a simple articulation, the end of the connecting rod will be restricted on a horizontal guide fixed to the bench. The crank, on the other hand, will be responsible for moving the connecting rod through the fixed guide.

Another variable of importance regarding the analysis of the parts, are the loads that are applied externally to allow the operation of the mechanism. The proposed design is driven entirely by the ratchet part, which will move due to the tension of the cables. These cables are responsible for transmitting the force applied by the driver's thumb from the gear lever, located on the handlebar, to the point of application.

As for the load used for the analysis, a value will be estimated from the effort that any individual of the human population can make with the thumb. In studies in this regard, minimum values among 3 and $5\ kg$ have been obtained. Considering that the gear lever assembly can integrate a reductor pulley system, the minimum load finally applied to the lever is estimated at about $2\ kg$, which results on a $4\ kg$ load transmitted by the cable [45].

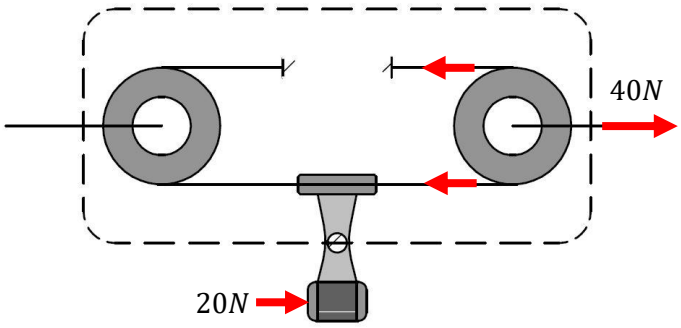

Figure 34. Scheme of pulley transmission in shifting lever. Source: own elaboration.

On the other hand, among the parts of the ratchet, different springs are also used, with the goal of recovering the initial position after the cable is deactivated. These include a pair of compression springs mounted next to the slider and another pair of torsion springs mounted on the joint. The features of the springs used, as well as the forces generated by them, will be defined together with the free body diagram of every affected part.

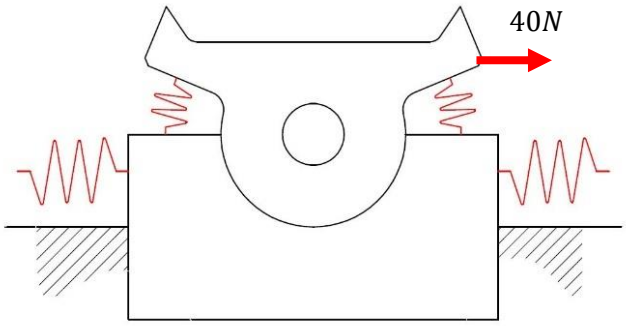

Figure 35. Schematic drawing of ratchet mechanism with springs. Source: own elaboration.

Finally, to begin with the design and analysis of the parts, it is necessary to define the material used to produce them. The properties of these materials will be important to check if the parts are suitable to withstand the stresses which they are exposed to during the operation of the mechanism.

In the selection of materials, different factors must be considered, which can be assessed in different order according to the project to be developed. For the proposal, the selection of materials will be followed according to the common method used by most designers nowadays, in which the criteria are divided into 3 groups: the property profile (mechanical strength and durability), the process profile (physical, manufacturability and costs) and the environmental profile.

As can be seen below, practically all the parts studied are loaded the most by bending momentums, and less by axial or lateral forces. According to the property criteria, facing bending loads, it is more interest to use materials with a high rigidity, in addition to guaranteeing an optimal yield strength [46].

Physical Properties	Metric
Density	7.872 g/cc

Mechanical Properties	Metric
Hardness, Brinell	86
Hardness, Knoop	103
Hardness, Rockwell B	49
Hardness, Vickers	88
Tensile Strength, Ultimate	295 MPa
Tensile Strength, Yield	165 MPa
Elongation at Break	30 %
Reduction of Area	55 %
Modulus of Elasticity	206 GPa
Bulk Modulus	163 GPa
Poissons Ratio	0.29
Machinability	50 %
Shear Modulus	80.0 GPa

Table 2. AISI 1006 steel properties. Source: [47].

Steels are very interesting materials for their low density and variety of applications, in addition to their mechanical properties. These maintain high Young's modulus values

(above $200\ GPa$), while yield strength and ultimate strength values depend on the composition and concentration of the alloy.

As a first selection, AISI 1006 steel will be used, which is considerably rigid with relatively low strength. During the mechanical study of the parts, if the material failure is proven, being unable to validate the part, two types of measurements can be taken: to modify the part to adapt it to the efforts generated or to select a new material with greater properties [47].

3.2. SWITCHING MECHANISM

The ratchet assembly is the system that collects the force from the cable to transmit it to the rest of the mechanism. Leaving aside the bench, it is formed by a sliding part, a switching pawl, and the articulation shaft. In addition, it includes a series of springs that maintain the initial position of the assembly, a requirement for the mechanism to work.

First of all, in order to identify the free body diagrams of the parts, it is necessary to define which loads are external forces applied to the mechanism, and which ones should be calculated as reactions. The following figure shows these parts and their distribution of forces.

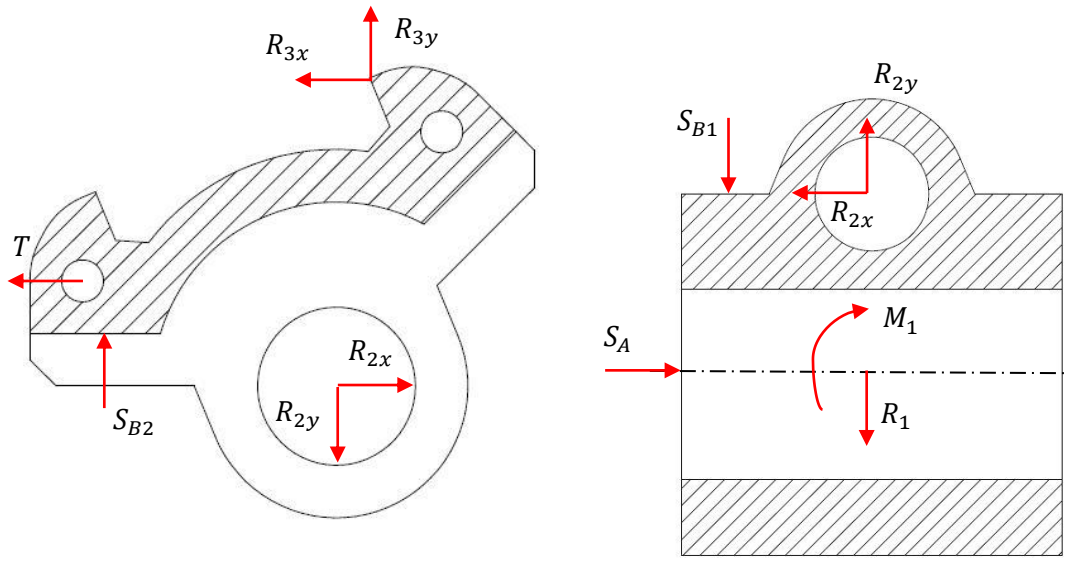

Figure 36. Free body diagram of the switching mechanism. Source: Own elaboration.

In the figure, the tension applied by the cable is represented by T, while the loads applied by the springs are indicated by S. For the selection of springs, the catalogue of commercial springs has been considered, which are produced from the appropriate DIN standards.

For the axial displacement of the sliding piece, a couple of compression spring is mounted. The selection must follow the dimensional conditions established by both switching parts. The sliding part must be moved at least a $10\ mm$ distance in each direction, and it must also have an internal diameter larger than $5\ mm$ and an external diameter lower than $9\ mm$.

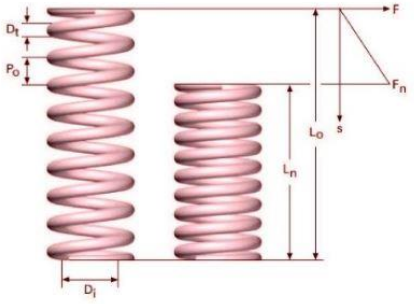

Ficha técnica

LONGITUD LIBRE	15
DIAMETRO EXTERIOR	7.45
DIAMETRO INTERIOR	6
DIAMETRO DEL HILO	0.6
ESPIRAS UTILES	4.55
ESPIRAS TOTALES	6.3
CONSTANTE "K"	0.96
Material	EN 10270-1 SH

Figure 37. Dimensions and features of the slider part. Source: [48].

Figure 37 shows the features of the selected spring, which have a 0.96 spring coefficient. To calculate the forces produced by a spring, formulas [f.4] or [f.5] must be used. From this calculation it is obtained that the force generated by the spring is a $9.60\ N$ load, applied to the slider at the maximum point of its travel.

$$\underline{Compression\ spring}:$$

$$F = kx \qquad [f.4]$$

$$S_A = kx = 0.96\frac{N}{mm} \cdot 10\ mm = 9.60\ Nmm$$

$$\underline{Torque\ spring}:$$

$$T = k'\alpha \qquad [f.5]$$

$$T_S = k\alpha = 96\frac{Nmm}{rad} \cdot 22.5° \cdot \frac{\pi\ rad}{180°} = 37.70\ Nmm$$

$F - Force\ [Nmm]$.
$T - Torque\ [Nmm]$.
$k - Force\ spring\ coeficient\ \left[\frac{N}{mm}\right]$.
$k' - Torque\ spring\ coeficient\ \left[\frac{Nmm}{rad}\right]$.
$\alpha - Torque\ angle\ [rad]$.

On the other hand, due to the dimensional construction of the parts, the torsion springs used in the articulation cannot be obtained directly from the catalog but will be based on one of its models. Taking as reference a $3\ mm$ shaft diameter, the spring used will be $0.4\ mm$ thick and have a $0.096\ Nm/rad$ spring coefficient. From the calculated torque, the load generated at the contact point is calculated [49].

$$S_{B1} = \frac{M_S}{R} = \frac{37.70}{3.85} = 9.79\ N$$

$$S_{B2} = \frac{M_S}{R} = \frac{37.70}{3.30} = 11.42\ N$$

$R - Radius\ to\ contact\ point\ [rad]$.

Once these results are substituted into the free body diagram, the reactions can be calculated using the equilibrium equations. As three of the variables in the diagram have been defined, there are a total of five unknown forces to be calculated. Since it is possible to use up to three equilibrium equations for each part, it follows that the diagrams presented are correct.

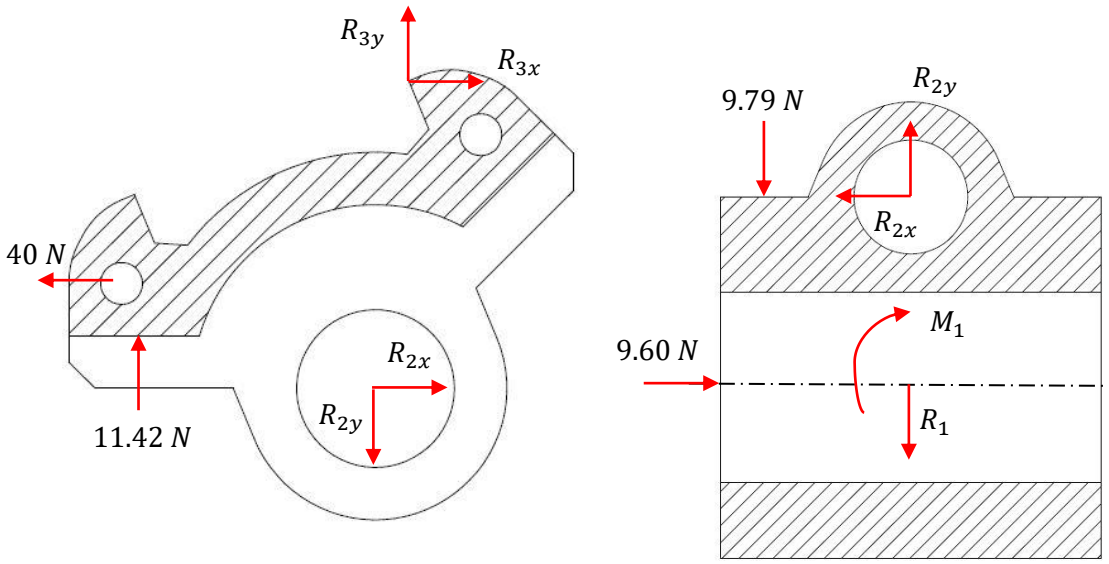

Figure 38. Unsolved free body diagram produced on the switching mechanism. Source: Own elaboration.

As an observation, the equilibrium of each part cannot be solved separately and, therefore, it is necessary to combine the calculations made on the two pieces simultaneously. The equilibrium equations used are as follows.

Sliding part:

$$\sum F_x = 0 \qquad R_{2x} = 9.60\ N$$

Switching pawl part:

$$\sum F_x = 0 \qquad R_{3x} + 40 = R_{2x}$$

$$R_{3x} = R_{2x} - 40 = 9.60 - 40 = -30.40N$$

$$\sum M = 0 \qquad R_{3y} \cdot 0.63 + R_{3x} \cdot 5.86 + 40 \cdot 1.657 = 11.42 \cdot 3.15$$

$$R_{3y} = \frac{11.42 \cdot 3.15 - R_{3x} \cdot 5.86 - 40 \cdot 1.66}{0.63}$$

$$= \frac{11.42 \cdot 3.15 + 30.40 \cdot 5.86 - 40 \cdot 1.66}{0.63} = 234.47N$$

$$\sum F_y = 0 \qquad R_{2y} = R_{3y} + 11.42 = 234.47 + 11.42 = 245.89N$$

$$\underline{Sliding\ part:}$$

$$\sum F_y = 0 \qquad R_{2y} = R_1 + 9.79$$

$$R_1 = 245.89 - 9.79 = 236.10N$$

$$\sum M = 0 \qquad 9.60 \cdot 5 - 9.79 \cdot 3.85 = 85.69Nmm$$

In addition to the calculated variables, which are represented in figure 39, a momentum has also been obtained as the result of the last equation above. This appears as a reaction in the tubular surface of the slider, due to the real distribution of forces in it.

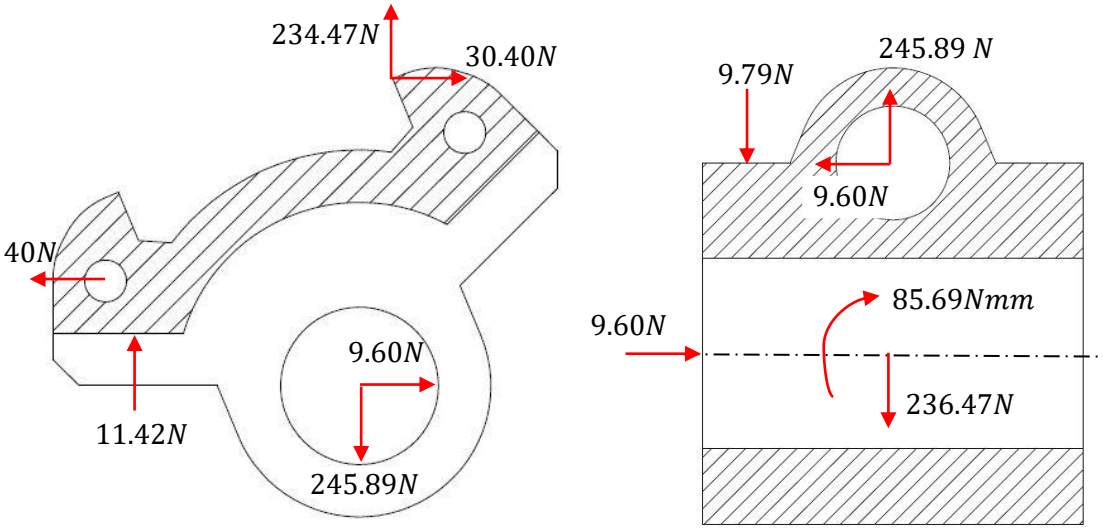

Figure 39. Solved free body diagram produced on the switching part. Source: Own elaboration.

3.2.1. SLIDER PART

The slider is the part that allows the translation movement of the pawl. This element, as well as the rest of the ratchet assembly, is mounted on a cylindrical guide assembled to the bench. Figure 40 shows the geometry and dimensions of the part, which incorporates a pair of side flaps to avoid inadequate rotations on the guide axis.

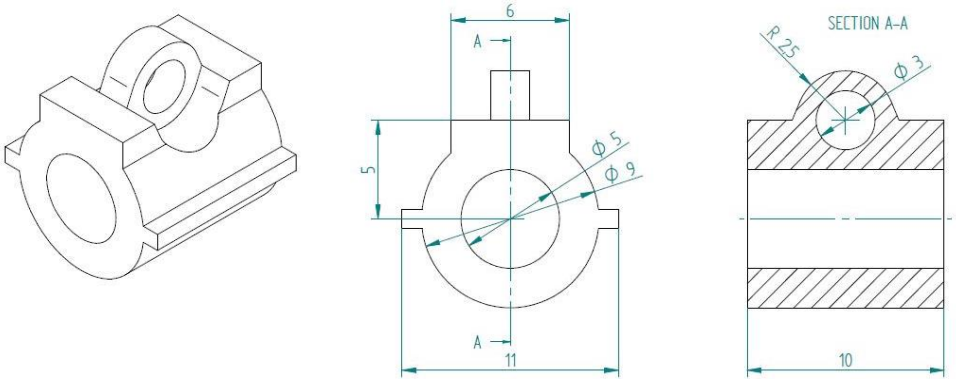

Figure 40. First dimensional model of the slider part. Source: Own elaboration.

STATIC ANALYSIS

From the free body diagram, presented in figure 39, the loads that appear along the slider are defined. The calculated forces give rise to bending and shear loads in the sections of the part. These strains are shown below in the diagrams in figure 41.

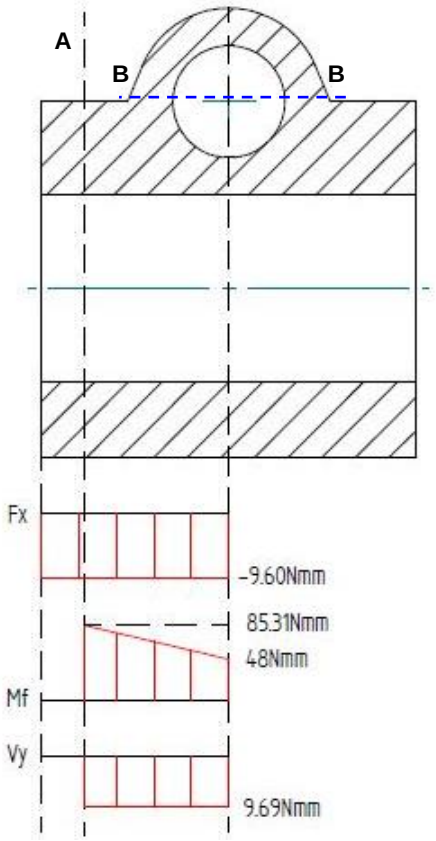

Figure 41. Strain diagrams for the slider part. Source: Own elaboration.

It is important to comment that the bending moment diagram depend on the direction of calculation, obtaining an equal but inverted line. In any case, the critical section and the strains studied would be the same.

From the stress diagram it is determined that section A is the most compromised of the main body of the part. In addition, the behavior of section B will be analyzed, since it has reduced dimensions compared to the rest of the part.

$$\sigma_{Tmax} = \frac{F}{A} = \frac{F}{\pi(R^2 - r^2)} \qquad [f.6]$$

$$\sigma_{Fmax} = \frac{M_F \cdot x}{I_y} = \frac{4M_F R}{\pi(R^4 - r^4)} \qquad [f.7]$$

$$\tau_{Vmax} = \frac{V_x \cdot Q}{I_y \cdot t} = \frac{8V_x(R^3 - r^3)}{3\pi(R^4 - r^4)(R - r)} \qquad [f.8]$$

$\sigma_{Tmax} - Maximum\ axial\ stress\ [MPa]$.
$F - Axial\ load\ [N]$.
$R - Larger\ area\ Radius\ [mm]$.
$r - Smaller\ area\ radius\ [mm]$.
$\sigma_{Fmax} - Maximum\ flection\ stress\ [MPa]$.

$M_F - Bending\ momentum\ [Nmm]$.
$x - Distance\ to\ the\ neutral\ fibre\ [mm]$.
$I_y - Inertia\ momentum\ [mm^4]$.
$\tau_{Vmax} - Maximum\ shear\ stress\ [MPa]$.
$V_x - Lateral\ load\ [N]$.
$Q - Statical\ moment\ of\ area [mm^3]$.
$t - Length\ of\ the\ shear\ fibre [mm^4]$.

$$\sigma_{VM} = \sqrt{\sigma^2 + 3 \cdot \tau^2} \qquad [f.9]$$

The calculation of maximum stresses of section A, which has a tubular area, is determined by formulas [f.6], [f.7] and [f.8], which are derived from the formulas used for circular areas.

Table 2 shows the results obtained by applying formulas [f.6], [f.7] and [f.8]. Furthermore, since neutral fiber combines axial and lateral stresses, as shown in figure 42, the failure theory, suitable for ductile materials, must be used. According to maximum distortion energy theory, the Von Mises stress must be calculated using the formula [f.9], which is valid to be compared with the yield strength of the material.

	Section A
Axial load [N]	-9,6
Lateral load [N]	9,79
Bending moment [Nmm]	85,69
Axial stress [Mpa]	-0,22
Maximum bending stress [Mpa]	1,32
Maximum shear stress [Mpa]	0,85
Von Mises stress in neutral fiber [Mpa]	1,48
Principal stress in edge fiber [Mpa]	-1,54

Table 3. Results of the analysis on the A section of the slider part. Source: Own elaboration.

According to the diagrams in figure 42, the stresses generated along section A are considerably low, with a $1.54\ MPa$ maximum compression stress applied to the upper fiber. Neither this value, nor the $1.48\ MPa$ von mises stress on the neutral fiber, can be considered troubling for the performance of the slider.

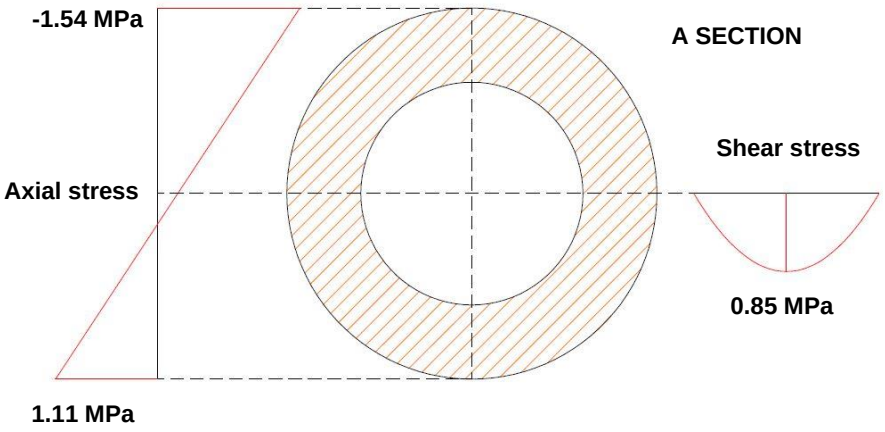

Figure 42. Diagrams of maximum stresses in the A section of the slider part. Source: Own elaboration.

In reference to the section B, is required to consider the stress concentration, which appears at this kind of articulated geometries. For the calculation of stresses in concentration, an extra factor related to the dimensions of the part must be considered. This value of the stress concentration factor is determined with the graph in figure 43. For a $5\,mm$ wide and $2\,mm$ thick part with a hole of $3\,mm$ diameter, the stress concentrator coefficient is $K_t = 2.25$.

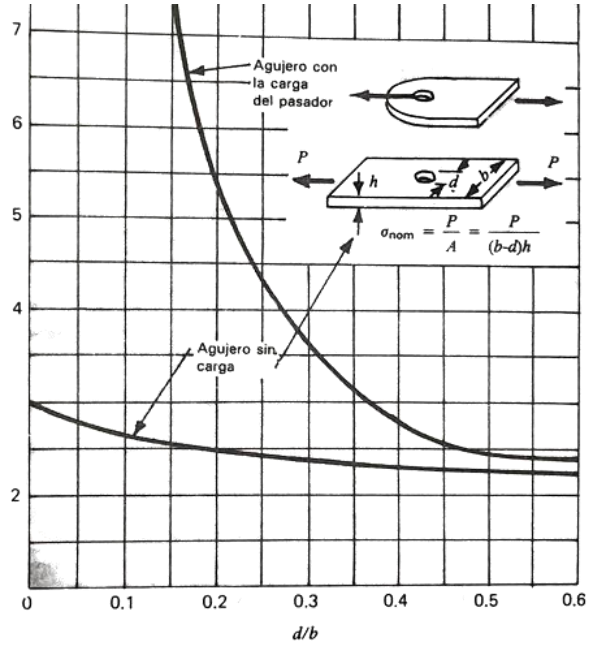

Figure 43. Graph for calculation of stress concentration factor. Source: [50].

Since the area of section B is formed by two separate rectangles, the formulas used will be [f.10], [f.11] and [f.12], which allow for calculating the maximum stresses that appear in a rectangular section.

$$\sigma_{Tmax} = \frac{F}{A} = \frac{F}{HB} \qquad \text{[f.10]}$$

$$\sigma_{Fmax} = \frac{M_F \cdot x}{I_y} = \frac{6M_F}{HB^2} \qquad \text{[f.11]}$$

$$\tau_{Vmax} = \frac{V_x \cdot Q}{I_y \cdot t} = \frac{3V_x}{2HB} \qquad \text{[f.12]}$$

$\sigma_{Tmax} - Maximum\ axial\ stress\ [MPa]$
$F - Axial\ load\ [N].$
$H - Thickness\ of\ the\ section\ [mm].$
$B - Width\ of\ the\ section\ [mm].$
$\sigma_{Fmax} - Maximum\ flection\ stress\ [MPa]$
$M_F - Bending\ momentum\ [Nmm].$
$x - Distance\ to\ the\ neutral\ fibre\ [mm].$
$I_y - Inertia\ momentum\ [mm^4].$
$V_x - Lateral\ load\ [N].$
$Q - Statical\ moment\ of\ area [mm^3].$
$t - Length\ of\ the\ shear\ fibre [mm^4].$

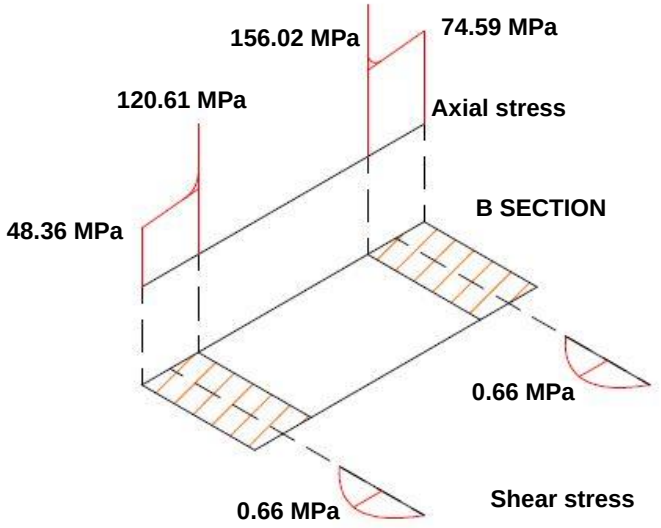

Figure 44. Diagrams of maximum stresses in the B section of the slider part. Source: Own elaboration.

As results, for the points which are not affected by concentrations, the stress produced is a $74.59\,MPa$ maximum bending stress. Considering the concentration factor, the maximum stress is $156.02\,MPa$, generated in the inner bore fiber. Compared to the material properties, the safety factor obtained is 1.1, which is too low for the part to performance safely. As a design requirement, a 1.4 minimum value is established for the safety factor.

	Section B	Section B'
Axial load [N]	245,89	245,89
Lateral load [N]	9,6	9,6
Bending moment [Nmm]	85,69	85,69
Axial stress [Mpa]	61,47	40,98
Maximum bending stress [Mpa]	13,12	8,16
Maximum shear stress [Mpa]	0,66	1,16
Von Mises stress in neutral fiber [Mpa]	71,97	47,15
Principal stress in edge fiber [Mpa]	74,59	49,14
Principal stress in bore fiber [MPa]	156,02	100,08

Table 4. Results of the analysis on the B section in the slider part. Source: Own elaboration.

As a solution to the overload, it is proposed to modify the dimensions of the part to increase the section and reduce the maximum stress in the critical fibers. The following calculation table shows the resulting values if the $5\,mm$ external radius is increased to $7\,mm$. Be notable that the maximum stress value has been greatly reduced and the stress at the concentration point is even lower. The safety factor obtained is 1.6.

DYNAMIC ANALYSIS

The dynamic analysis will focus on the critical points of section B, which has proven to be the most strained. Since the load applied to the joint varies depending on the direction of activation of the cable, the stress generated in the inner fiber follows the curve of the figure 45.

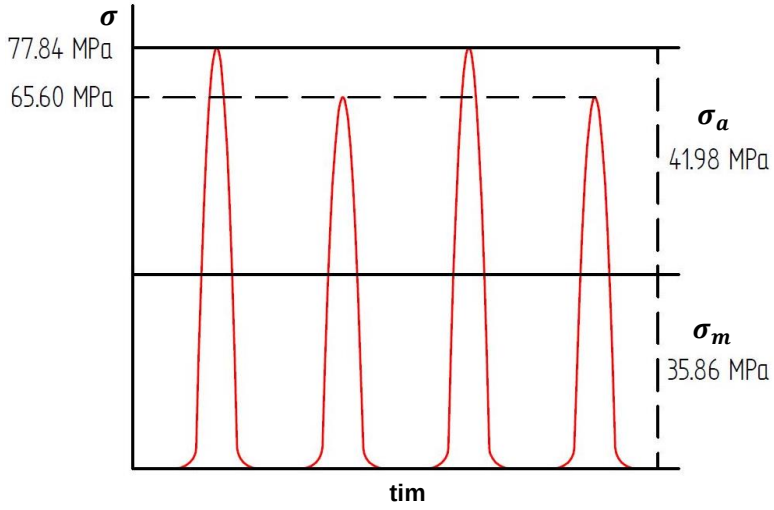

Figure 45. Graph of dynamic stresses in the critical fiber of section B. Source: Own elaboration.

Be noted that these values correspond to a correction of the stresses obtained in the static analysis, since the concentration factor used is different for each behavior. Using the formula [f.13], where it is estimated $q = 0.6$ for the material used, these values are corrected.

$$K_f = 1 + q \cdot (K_t - 1) \quad \text{[f.13]}$$

$q - Notch\ sensitivity.$
$K_f - Dynamic\ stress\ concentration\ factor.$
$K_f - Static\ tress\ concentration\ factor.$

From these strains, the average stress and the alternating stress are calculated. They will be compared to the material features, using the Goodman diagram method.

The fatigue performance of the material depends on different conditions, which are considered in the calculation by applying coefficients related to the design of the part. These coefficients are represented in formula [f.14] by K and correspond to the dimensions of the loaded sections, the kind of force applied, and the surface treatment used in the part. The values of these modifiers will be obtained by using the graphs and conditions defined in the annex, for all the parts designed.

For the steel used, which is produced by forging, the fatigue strength is defined as the $40\ \%$ of the ultimate strength ($\sigma_u = 295\ MPa$). The following formulas determine the value of the fatigue strength of the joint, as well as the part.

$$\sigma_{F,afr} = 0.4 \cdot \sigma_u$$

$$\sigma_{fat} = K_f \cdot K_l \cdot K_d \cdot K_s \cdot \sigma_{F,afr} = K_l \cdot K_d \cdot K_s \cdot 0.4 \cdot \sigma_u \qquad [f.14]$$

$\sigma_u - Ultimate\ strenght\ of\ the\ material.$
$K_t - Load\ factor.$
$K_d - Dimensional\ factor.$
$K_s - .Surface\ factor$

Since the slider part must be produced by machining, and the section B, which have a $3.19\ mm$ equivalent diameter, is loaded by stretching strains, the result obtained for the formula [f.14] is $95.58\ MPa$.

The Goodman diagram allows for comparing dynamic loads with the fatigue properties of the material, to determine whether failure will appear or not. Figure 46 shows that the working point is at a considerable distance from the Goodman line. The 1.4 safety factor is enough for the part to work properly.

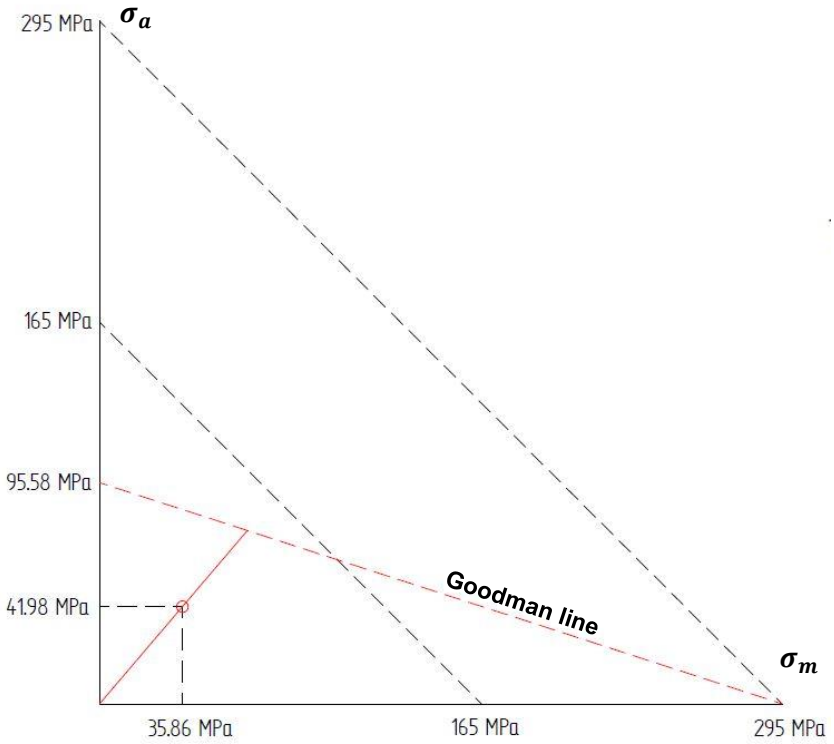

Figure 46. Goodman diagram for the section B of the slider part. Source: Own elaboration.

MECHANICAL SIMULATIONS

Finite element simulations allow for validating the calculations and checking if the behavior of the part is adequate. From the results, the part will be considered suitable for the defined operation, if they are favorable, or measures can be taken to improve the behavior of the part, in case they are unfavorable.

The simulation is settled by fixing one of the loaded points and applying the rest of the forces. For the slider part, the internal surface of the tube body is fixed, and the articulation is loaded by the calculated force.

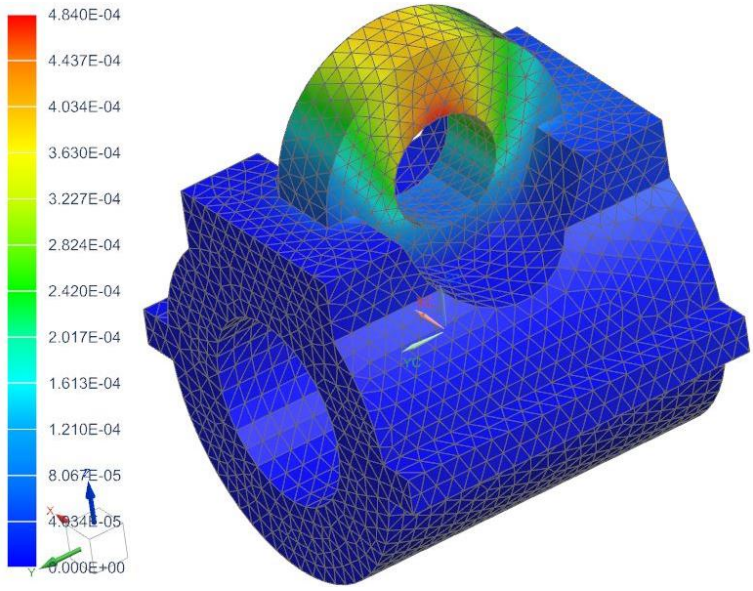

Figure 47. Resulting deformations obtained for the slider part. Source: Own elaboration.

As shown in figure 47, the most relevant deformations are found in the upper part of the joint. Since the maximum values are about $10^{-4}\ mm$ they are considered marginal.

Regarding the stresses, it is observed that the study of stress concentration in the joint was correct, while the values were considerably lower than those calculated. The maximum stress is $34.25\ MPa$ obtaining a safety factor of 4.2.

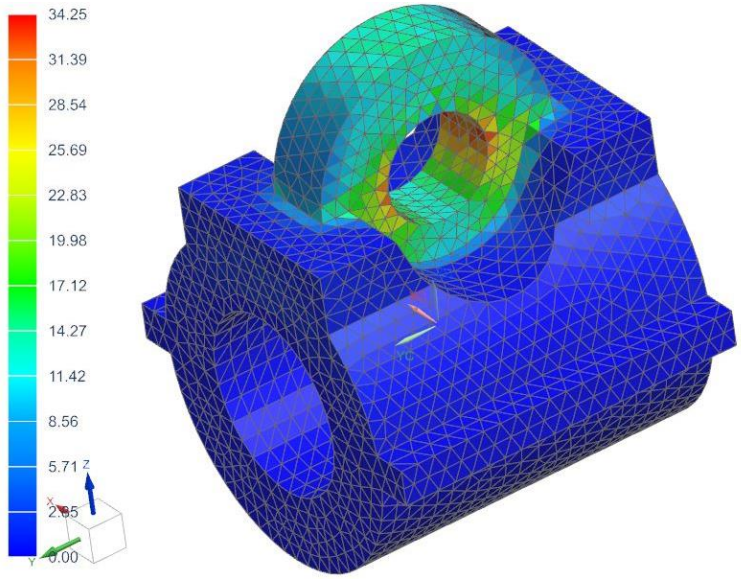

Figure 48. Resulting Von Mises stresses obtained for the slider part. Source: Own elaboration.

3.2.2. JOINT SHAFT

The switching pawl is articulated with the slider through a pin which acts as a shaft in the joint. The force of $246.07\ N$ is transmitted through this shaft, which is applied by the pawl part in two contact points, dividing the force. With respect to the slider, the joint is unique resulting in an axis requested by transverse forces at three points.

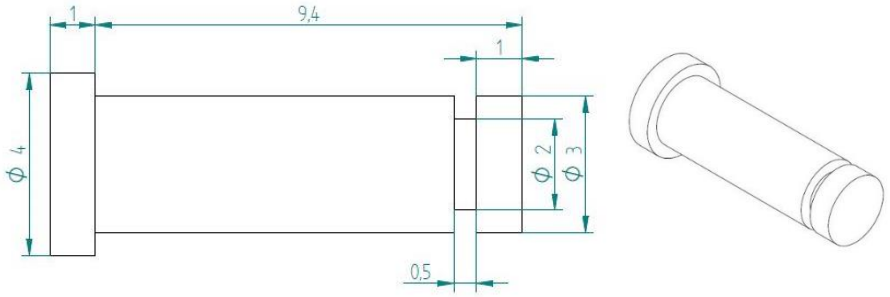

Figure 49. First model dimensions of the shaft. Source: Own elaboration.

Regarding the assembly of the shaft, the pin will be fixed axially by a Seeger ring, and therefore will be machined with a section reduction at its end. As an initial diameter has been chosen the one corresponding to the smallest Seeger ring, which is $3\ mm$. If shaft failure is proven, the diameter shall be increased according to the ring with the next larger diameter.

STATIC ANALYSIS

The diagram of bending moments and shear forces shows that the most strained section is at the midpoint of the axis length, in other words, the joint with the slider.

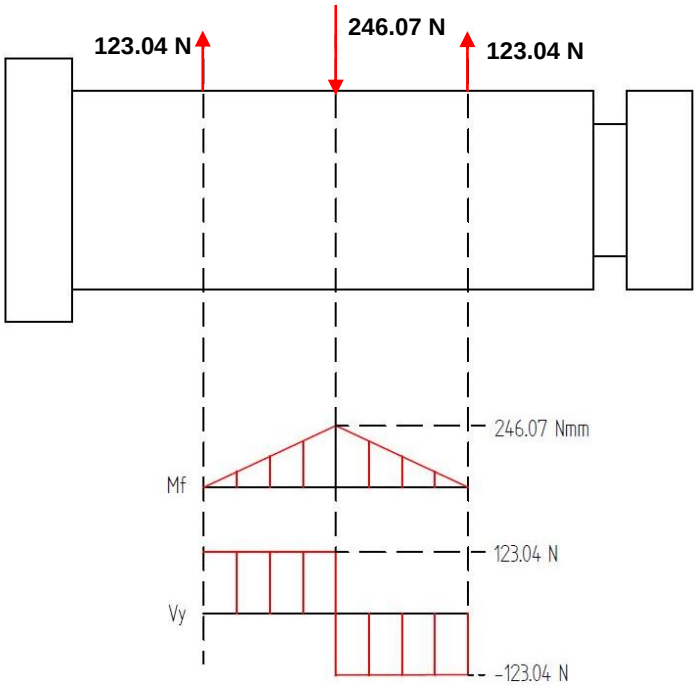

Figure 50. Strain diagrams for the joint shaft. Source: Own elaboration.

For the stress analysis of a circular section, the formulas to be used for the calculation of maximum stresses are as follows. The strains obtained from them are the maximum bending stress, which appears at the peripheric points, and the maximum shear stress located in the center of the neutral fiber.

$$\sigma_{Tmax} = \frac{F}{A} = \frac{F}{\pi R^2} \qquad \text{[f.15]}$$

$$\sigma_{Fmax} = \frac{M_F \cdot x}{I_y} = \frac{4M_F}{\pi R^3} \qquad \text{[f.16]}$$

$$\tau_{Vmax} = \frac{V_x \cdot Q}{I_y \cdot t} = \frac{4V_x}{3\pi R^2} \qquad \text{[f.17]}$$

$\sigma_{Tmax} - Maximum\ axial\ stress\ [MPa]$
$F - Axial\ load\ [N].$
$R - Area\ Radius\ [mm].$
$\sigma_{Fmax} - Maximum\ flection\ stress\ [MPa]$
$M_F - Bending\ momentum\ [Nmm].$
$x - Distance\ to\ the\ neutral\ fibre\ [mm].$
$I_y - Inertia\ momentum\ [mm^4].$
$V_x - Lateral\ load\ [N].$
$Q - Statical\ moment\ of\ area [mm^3].$
$t - Length\ of\ the\ shear\ fibre [mm^4].$

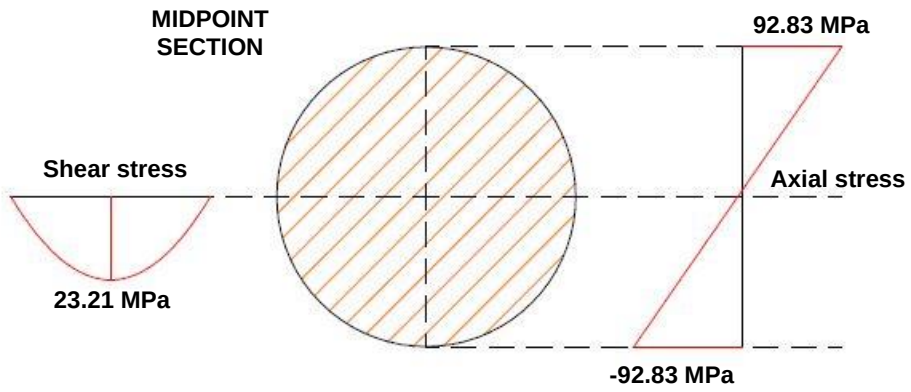

Figure 51. Diagrams of maximum stresses in the midpoint section of the shaft. Source: Own elaboration.

As shown in the stress diagrams, as well as the calculation table, the main stresses are those that are generated at the top and bottom points as a result of the bending. Compared to the strength of the steel used, these stresses give a 1.8 safety factor.

	Critical section
Lateral load [N]	123,04
Bending moment [Nmm]	246,07
Maximum bending stress [Mpa]	92,83
Maximum shear stress [Mpa]	23,21
Von Mises stress in neutral fiber [Mpa]	40,20
Principal stress in edge fiber [Mpa]	92,83

Table 5. Results of the analysis on the leg coupled to the cable. Source: Own elaboration.

DYNAMIC ANALYSIS

For the dynamic analysis of the shaft, this part is considered to be fixed to the slider, while the pawl part rotates on it. This last one has a total travel of $45°$, causing the studied force to swing along $4.72°$.

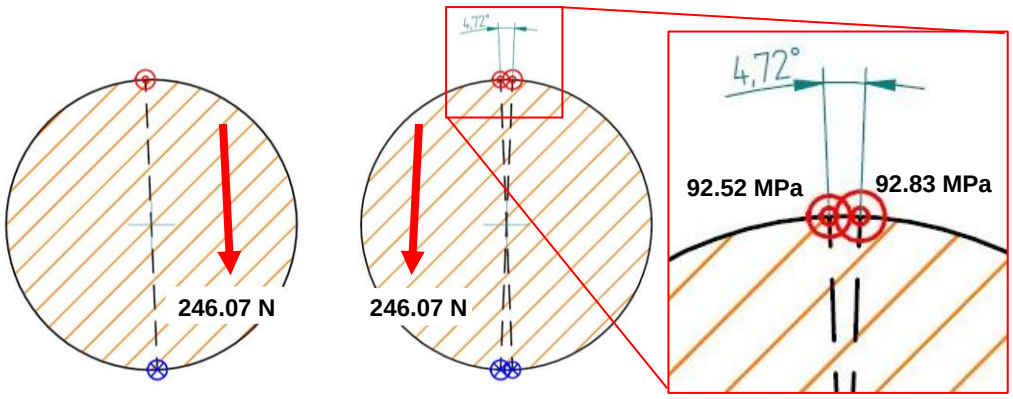

Figure 52. Working stages of the joint shaft on the midpoint section. Source: Own elaboration.

Since the swing angle is minimal, the stresses generated in the same fiber, for both working stages, are practically the same. Unlike the slider, the shaft does not contain any conflicting geometry which could generate stress concentrations. Considering this and the features of the material, the surface treatment and the pure bending, the fatigue strength obtained for the shaft is $106.20\ MPa$.

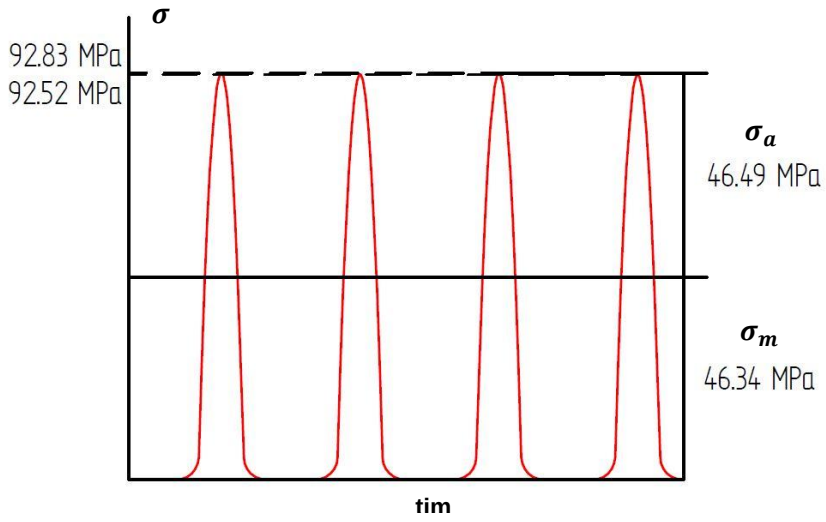

Figure 53. Graph of dynamic stresses in the midpoint of the joint shaft. Source: Own elaboration.

After applying the Goodman method, the safety value obtained is 1.7, which is adequate so that the part does not suffer during its work.

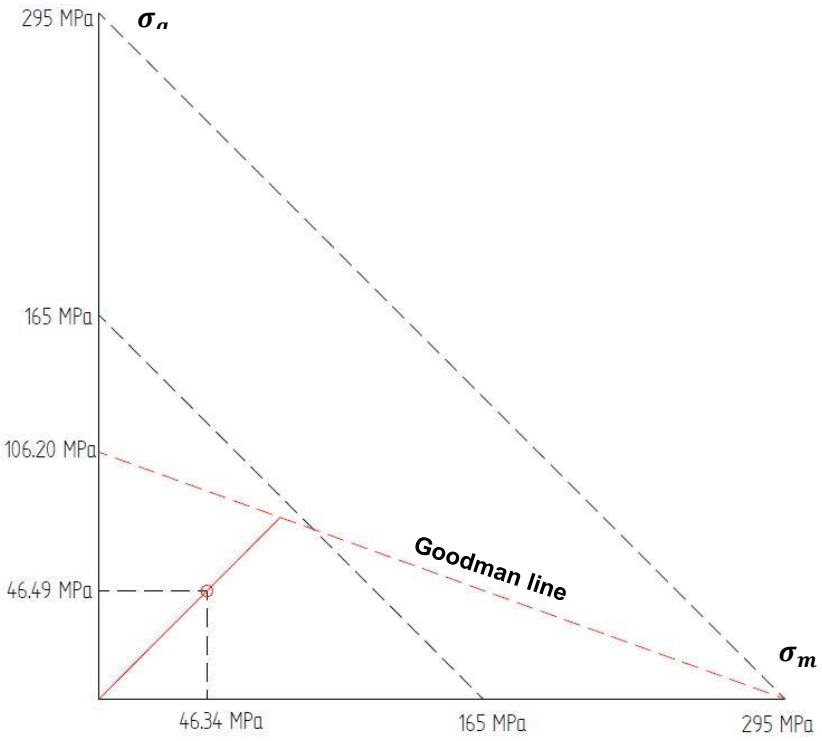

Figure 54. Goodman diagram for the midpoint section of the joint shaft. Source: Own elaboration.

MECHANICAL SIMULATIONS

The values calculated must be compared with those obtained by simulations. First, the simulations show that the most stressed points appear along the contact surface of the slider joint, which is placed in the midpoint of the shaft length.

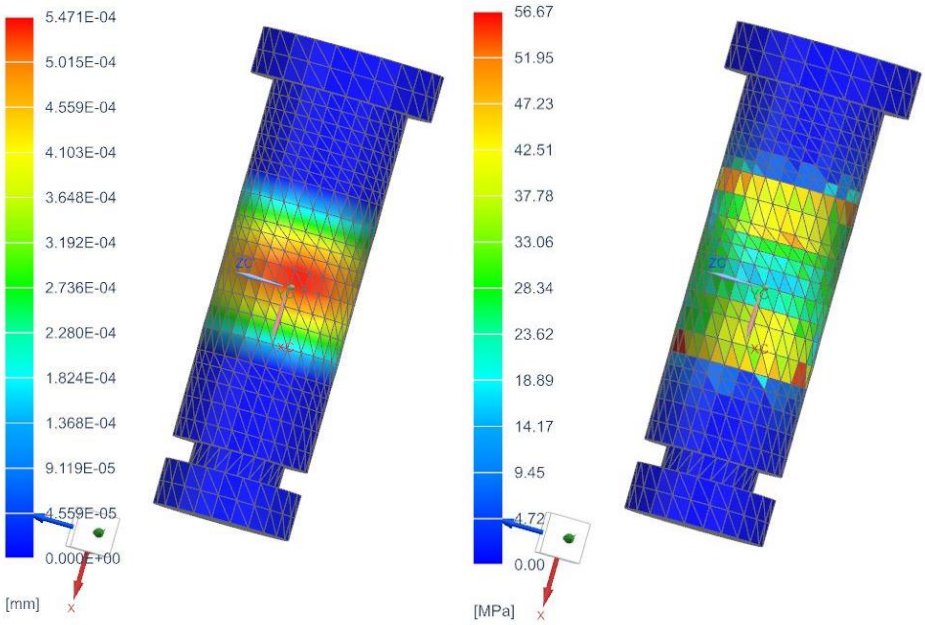

Figure 55. Resulting deformations and stresses obtained for the joint shaft. Source: Own elaboration.

As shown, the $56.67\ MPa$ obtained and the $92.83\ MPa$, calculated in the static analysis, contrast. This difference exists because the simulation has been configured more precisely compared to the manual calculation, in which they have been defined as point forces and not as distributions along the contact surface with the axis. In any case, the results are favorable for the performance of the shaft.

3.2.3. SWITCHING PAWL PART

The switching pawl is the part that transmits the tension, applied by means of the activation cable, to the rest of the mechanism. It is articulated to the sliding part and is geometrically designed with two legs at the top, which engage with the selector drum once they reach the maximum travel in their rotation.

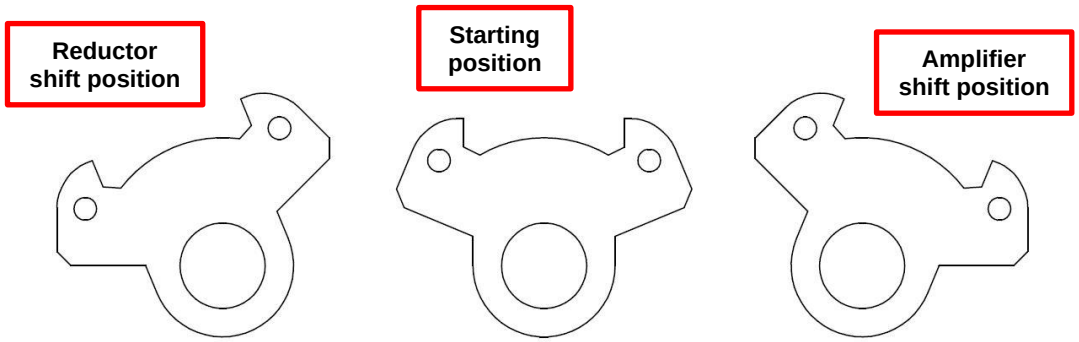

Figure 56. Different actuation states of the switching pawl part. Source: Own elaboration.

As a dimensional reference the selector drum, which is engaged by the pawls, has a $10\ mm$ diameter contact section. Considering this measure, the geometry of the part has been defined. The construction of the legs allows for coupling the drum after a rotation of $22.5°$ for each direction, with a maximum travel range of $45°$. They are designed to avoid contact during the activation and the recovery operations.

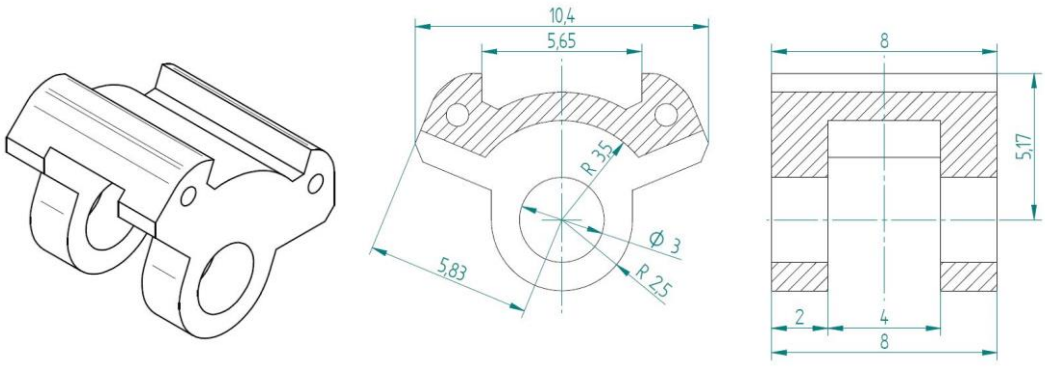

Figure 57. First model dimensions of the switching pawl part. Source: Own elaboration.

STATIC ANALYSIS

For the switching pawl, free body diagram shows several reactions in different directions. This, together with the geometric complexity of the part, adds difficulty to the analysis. Instead of focusing on defining the most strained points, the analysis will be based on studying different sections of interest. From the results, the points where the part suffers the most will be revealed.

As shown in figure 58, the pawl is mainly loaded at three points: the leg in contact with the selector drum, the leg driven by the cable, and the joint. Considering these points, the study will focus on both legs separately, as well as the joint section.

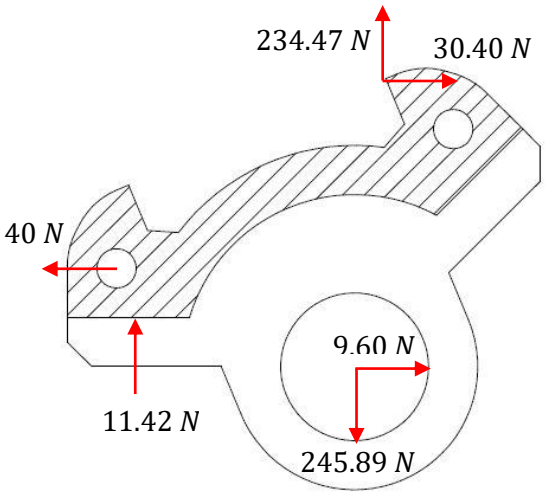

Figure 58. Equilibrium of the rigid body produced on the switching pawl part. Source: Own elaboration.

Since the part is constructed principally from rectangular and square sections, most stress calculations will be based on the formulas used for the joint section in the slider part analysis. For section with a greater complexity, the formulas used might be modified to consider its shape.

$$\sigma_{Tmax} = \frac{F}{A} = \frac{F}{HB} \qquad \text{[f.15]}$$

$$\sigma_{Fmax} = \frac{M_F \cdot x}{I_y} = \frac{6M_F}{HB^2} \qquad \text{[f.16]}$$

$$\tau_{Vmax} = \frac{V_x \cdot Q}{I_y \cdot t} = \frac{3V_x}{2HB} \qquad \text{[f.17]}$$

$\sigma_{Tmax} - Maximum\ axial\ stress\ [MPa]$
$F - Axial\ load\ [N].$
$H - Thickness\ of\ the\ section\ [mm].$
$B - Width\ of\ the\ section\ [mm].$
$\sigma_{Fmax} - Maximum\ flection\ stress\ [MPa]$
$M_F - Bending\ momentum\ [Nmm].$
$x - Distance\ to\ the\ neutral\ fibre\ [mm].$
$I_y - Inertia\ momentum\ [mm^4].$
$V_x - Lateral\ load\ [N].$
$Q - Statical\ moment\ of\ area [mm^3].$
$t - Length\ of\ the\ shear\ fibre [mm^4].$

In the contact leg, the section A is considered relevant. Since the loads are applied to the end of this piece, the highest bending stresses will appear in the fibers of the considered section. Figure 59 shows the stresses produced in the section, where the highest value is $43.68\ MPa$ in the top fiber.

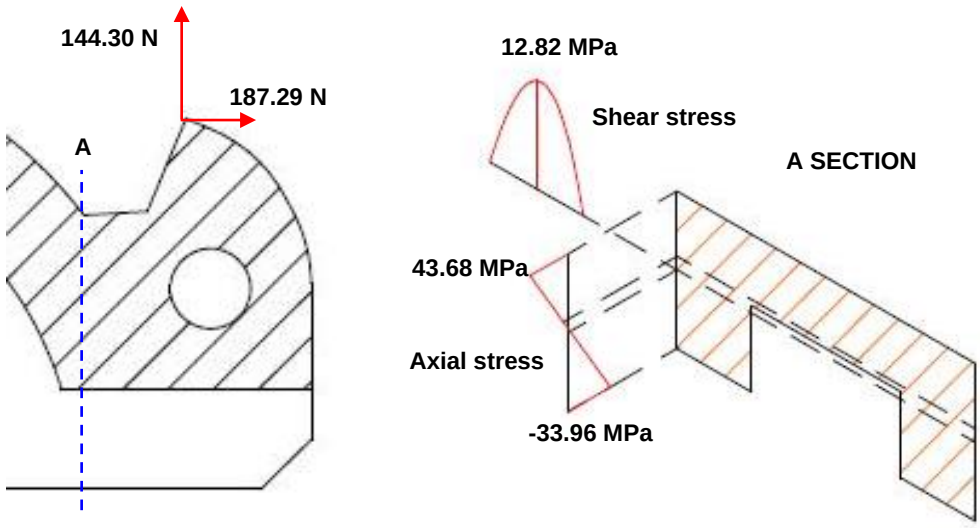

Figure 59. Left: Sections and forces applied to the leg in contact to the drum; Right: Diagrams of maximum stresses in section A. Source: Own elaboration.

In the case of the other leg, loads are applied due to cable tension and the contact with the torque spring. From these forces, axial and lateral strains are generated along the leg, in addition to a bending stress that is maximized up to section B.

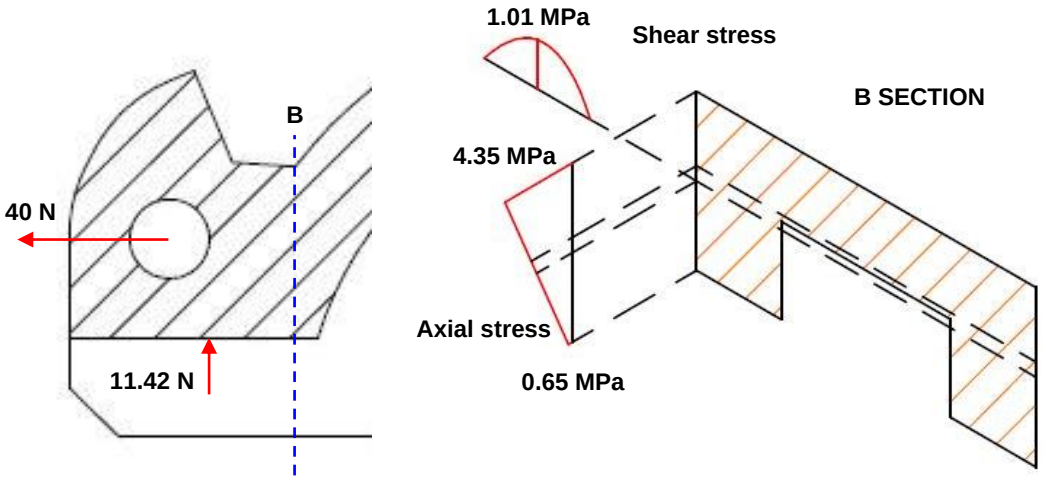

Figure 60. Left: Sections and forces applied to the leg coupled to the cable; Right: Diagrams of maximum stresses in section B. Source: Own elaboration.

Figure 60 shows the distribution of the stresses generated in section B. Compared to the other leg, this section works lighter. This is probably due to the magnitude and distribution of forces.

As the last point to study, the joint is dimensioned in the same way as in the sliding piece. For the switching pawl, the load is divided into two contact points. Since this articulation is formed by two contact points, as shown in figure 57, and therefore the strain applied to section C for a single one of them must be half.

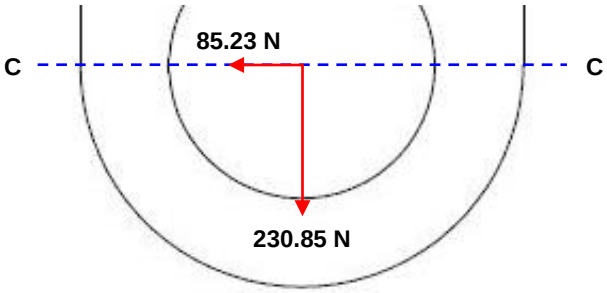

Figure 61. Sections and forces applied to the joint of the switching pawl. Source: Own elaboration.

Applying the same concentration factor as for the slider, the distribution of stresses in section C is the shown in figure 62. To conclude the static analysis of this part, the overall maximum stress is $64.93\ MPa$, which is produced in the inner bore fiber of section C. Comparatively, the material properties keep the part safe from any static failure, with a safety factor of 2.5.

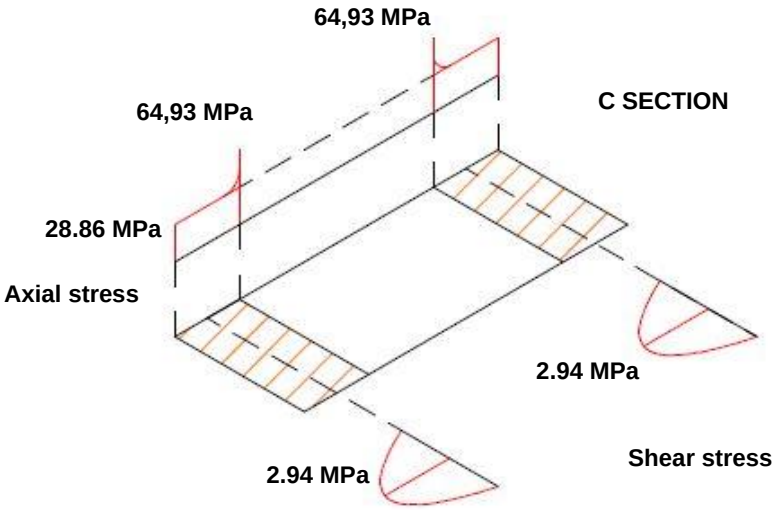

Figure 62. Diagrams of maximum stresses in section C. Source: Own elaboration.

DYNAMIC ANALYSIS

Dynamically, the part has two working states. Depending on the driven cable, the equilibrium diagram, which has been studied statically, may be presented in two symmetrical directions. Bearing in mind that these efforts appear during the instant that the pawl is engaged with the drum, the dynamic analysis will focus on the effect of the back and forth movement on its performance.

In addition, as the concentrated load is the same in the two fibers of the hole, the development of the dynamic load is as shown in figure 63. It also considers the corrected stress concentration coefficient for fatigue.

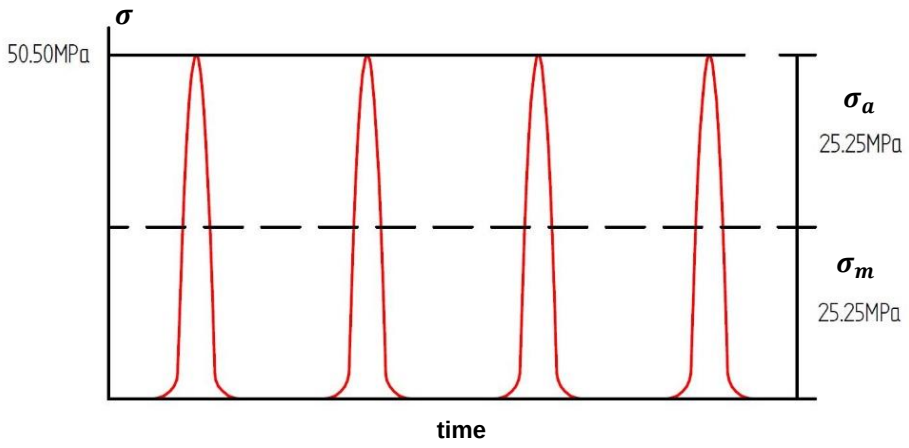

Figure 63. Graph of dynamic stresses in the section C of the switching pawl part. Source: Own elaboration.

As the dynamic loads are based on a pulsating axial force that does not vary in maximum value, the tensions of interest coincide, since they are half this value.

Considering the factors used for the sliding part, the same $95.58\ MPa$ fatigue strength can be used. As shown in figure 64, the margin for the fatigue work is significantly high.

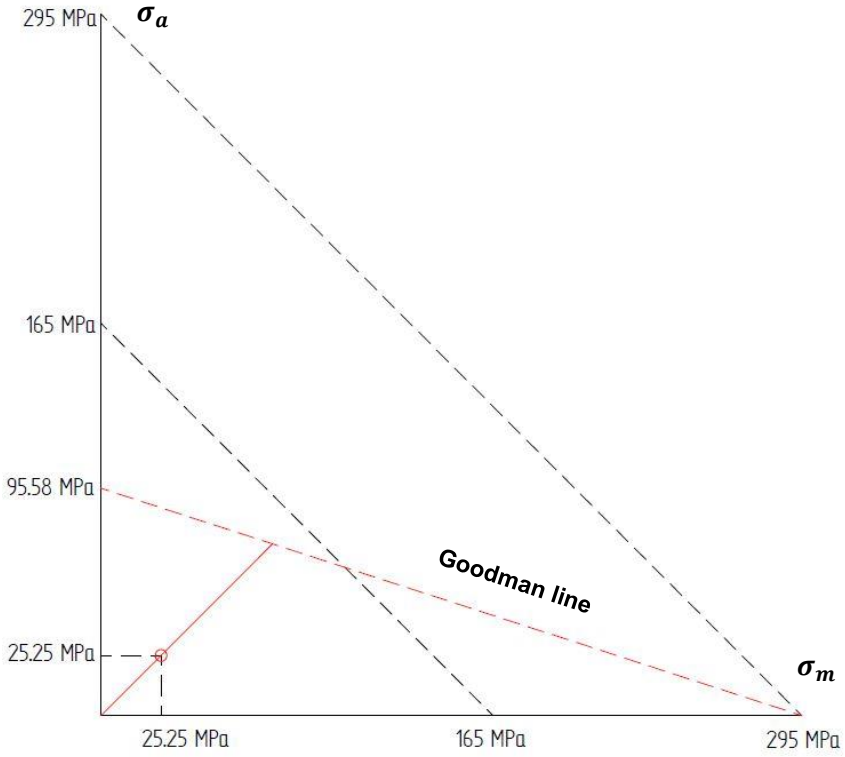

Figure 64. Goodman diagram for the section C of the switching pawl. Source: Own elaboration.

MECHANICAL SIMULATIONS

For the simulation, joint surfaces are settled as fixed points while the forces obtained for each leg are generated.

According to the results, the values obtained by calculations are valid: the leg connected to the cable is almost unstrained, while the sections in the joint and the contact leg reach stresses around $40\ MPa$.

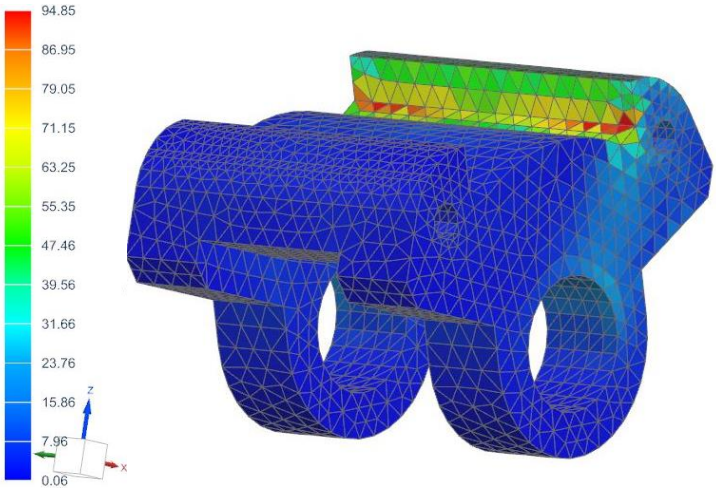

Figure 65. Resulting Von Mises stresses obtained for the switching pawl. Source: Own elaboration.

Regarding the $94.85\ MPa$ maximum stress shown in the figure 65, it is produced as a concentration due to the irregular geometry and the location of the cable connection bore. However, the safety factor obtained is 1.7 and, therefore the part is considered suitable.

3.3. SELECTOR MECHANISM

Once the switching assembly is activated, the forces are transmitted to the selector system. This mechanism is based on the modified crank-rod-piston assembly and consists of the selector drum, which works as a crank, the horizontally guided pin, the connecting rod, and the indicator rod in the piston role.

According to the design of the mechanism, it has three operating positions, from which different states of transmission are generated. For the analysis of the parts, these positions and states must be considered, since they influence in the static and dynamic behaviors of the parts.

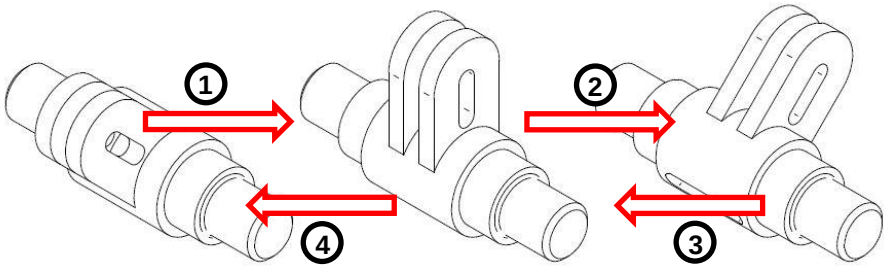

Figure 66. Selector drum positions. Source: Own elaboration.

First of all, the selector drum, which is in contact with the ratchet pawls, moves between three positions giving rise to four different equilibrium states:

1. Second speed activation from the first position.
2. Third speed activation from the second position.
3. Second speed activation from the third position.
4. First speed activation from the second position.

Since the contact forces transmitted by the switching pawl part are the same for all four states, the resulting force equilibrium coincide symmetrically, in pairs. And therefore, the study of the drum can be reduced to two different free body diagrams.

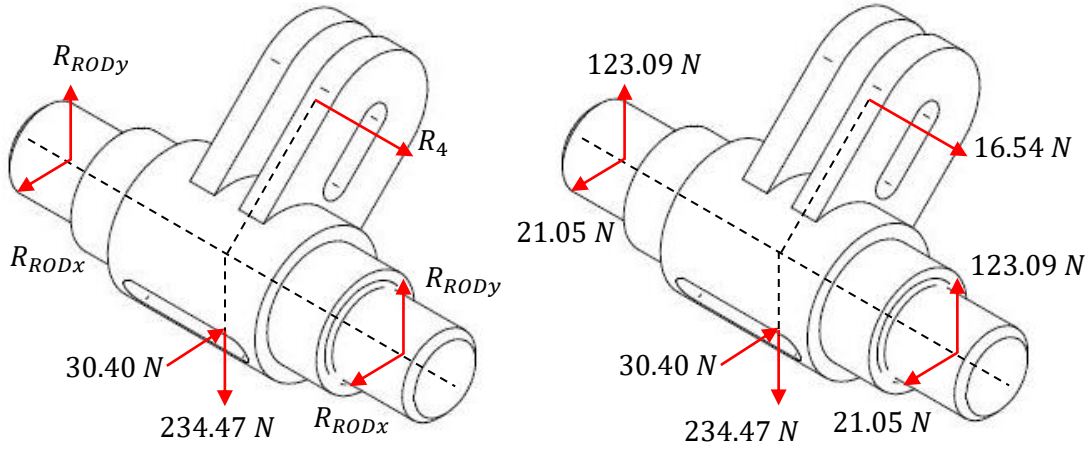

Figure 67. Equilibrium of the rigid body produced on the selector drum during the states 1 and 3. Source: Own elaboration.

$$\sum M = 0 \qquad R_4 \cdot 9.19 = 30.40 \cdot 5$$

$$R_4 = \frac{30.40 \cdot 5}{9.19} = 16.54N$$

$$\sum F_x = 0 \qquad 2 \cdot R_{RODx} = R_4 \cdot \cos(45°) + 30.40$$

$$R_{RODx} = \frac{16.54 \cdot \cos(45°) + 30.40}{2} = 21.05N$$

$$\sum F_y = 0 \qquad 2 \cdot R_{RODy} = R_4 \cdot \sin(45°) + 234.47$$

$$R_{RODy} = \frac{16.54 \cdot \sin(45°) + 234.47}{2} = 123.08N$$

Figure 67 presents the rigid solid equilibrium for states 1 and 3, along with the equilibrium equations used to solve it. As shown, the reactions generated in bearing sections, located at each end of the part, are also included.

In the following figure, the free body diagram for states 2 and 4 is represented. Comparatively, the reactions obtained in the bearings are higher for the diagrams above, while the reaction generated in the guide is greater for the second one.

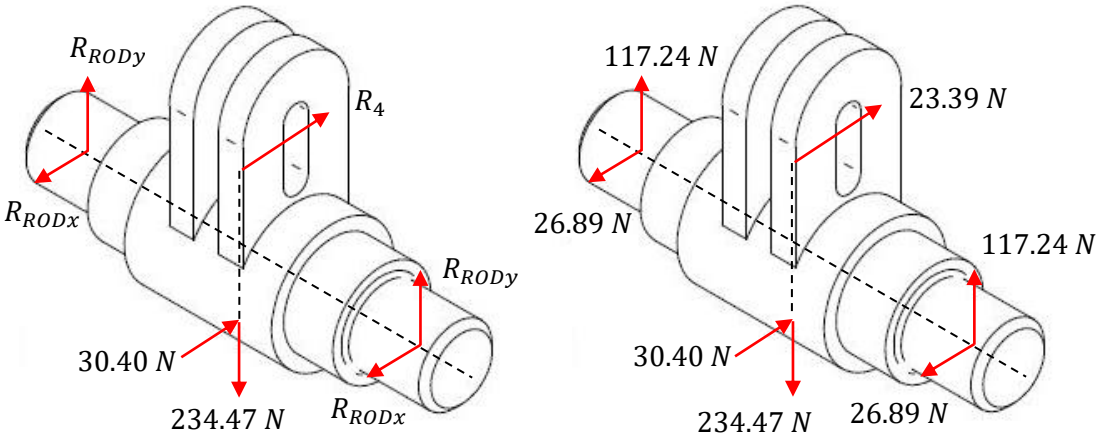

Figure 68. Equilibrium of the rigid body produced on the selector drum during the states 2 and 4. Source: Own elaboration.

$$\sum M = 0 \qquad R_4 \cdot 6.5 = 30.40 \cdot 5$$

$$R_4 = \frac{30.40 \cdot 5}{6.5} = 23.38N$$

$$\sum F_x = 0 \qquad 2 \cdot R_{RODx} = R_4 + 30.40$$

$$R_{RODx} = \frac{23.38 + 30.40}{2} = 26.89N$$

$$\sum F_y = 0 \qquad 2 \cdot R_{RODy} = 234.47$$

$$R_{RODy} = \frac{234.47}{2} = 117.24N$$

As for the guided pin, the reactions that appear also vary according to the gear driven, with the difference that the equilibrium states are all different. Figure 69 shows the four states already resolved. To define them, only the equilibrium equations corresponding to the vertical and horizontal forces are necessary.

In this part, the reactions that appear result from the contact with the guides on the bench, which generate a vertical load at the ends. Moreover, a reaction is generated in the midpoint by transmission to the connecting rod, which is permanently angled to 19°, and therefore the force also has this direction.

Furthermore, be also noted that, due to the geometric construction of the drum, the force transmitted by the drum is distributed at two contact points with the pin, as shown in the following figure.

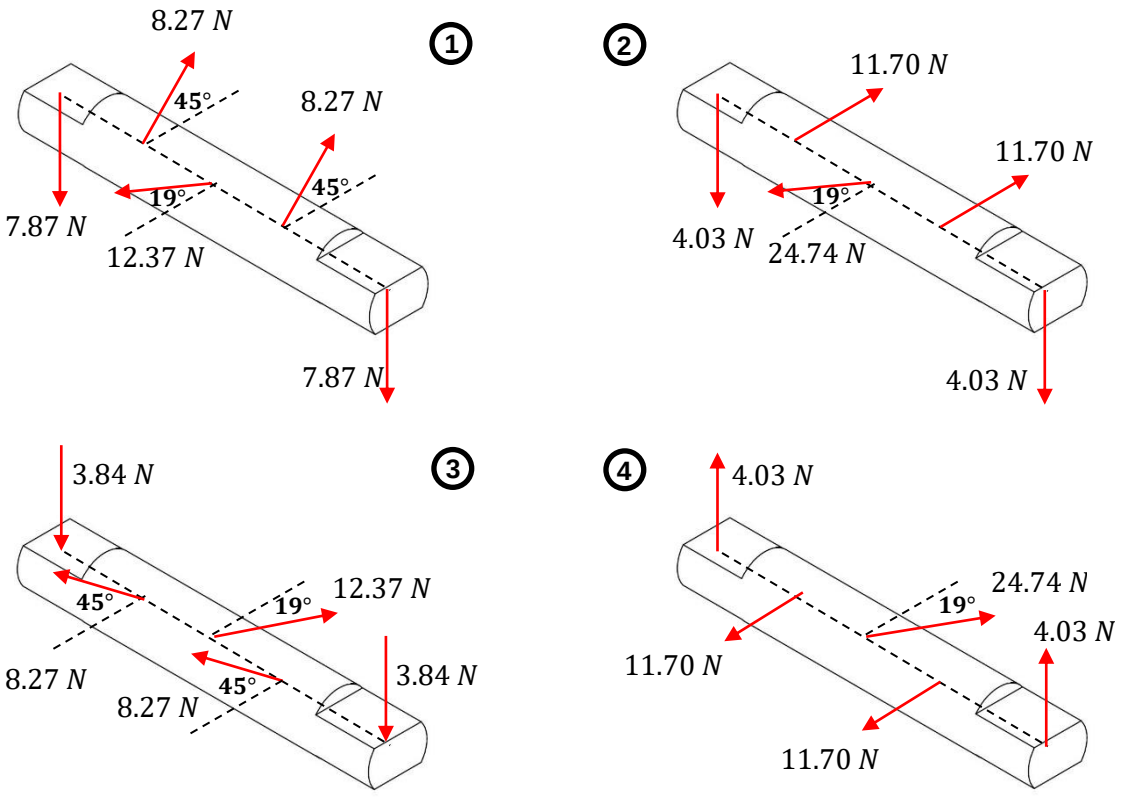

Figure 69. Equilibrium of the rigid body produced on the drum pin for every state. Source: Own elaboration.

As explained, the reaction obtained through the union with the connecting rod must have the same direction as this part, since it is only loaded at both joints. This 19° angulation corresponds to the segment formed by these points.

On the other hand, the shape of the rod is not straight but have an elbow shape. This is because, when operating the first speed, the connecting rod is pulled by the drum reaching contact and making it impossible to move.

Figure 70 shows the states produced in connecting rod. The rod works at a $24.74N$ maximum load, both compression and stretching, when the mechanism moves from the second speed.

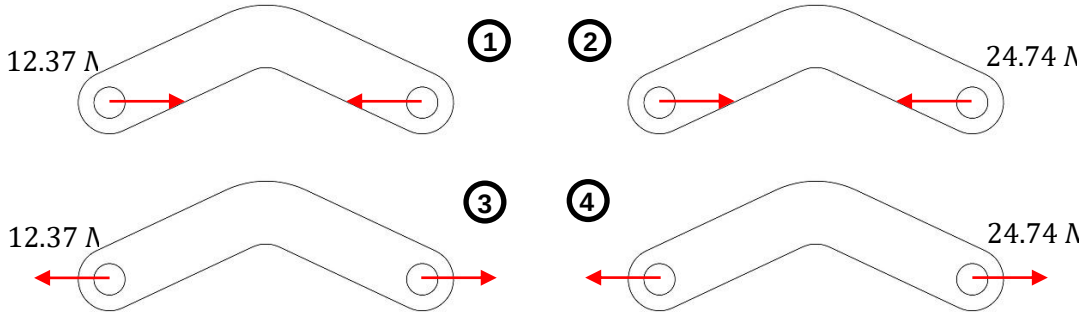

Figure 70. Equilibrium of the rigid body produced on the connecting rod for every state. Source: Own elaboration.

To conclude the free body calculations, the indicator rod receives the load transmitted by the connecting rod resulting in the equilibriums of the following figure. As represented in figure 71, the part is affected by a bending moment as a reaction to the vertical component of the load.

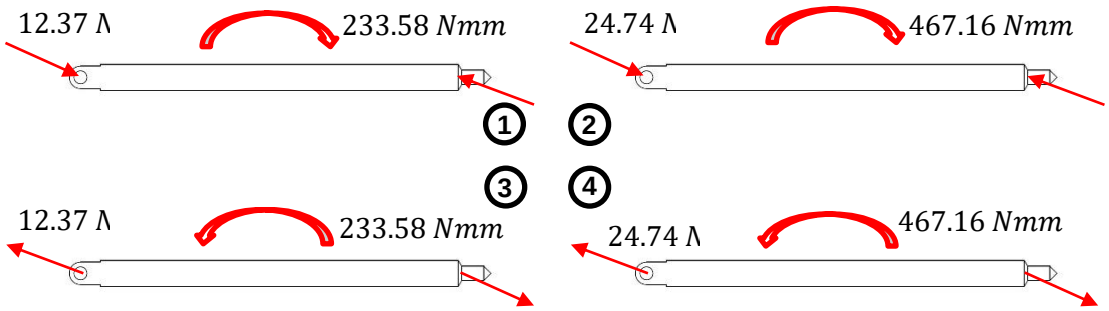

Figure 71. Equilibrium of the rigid body produced on the indicator rod for every state. Source: Own elaboration.

As for the connecting rod, the maximum reactions appear during states 2 and 4, when the mechanism is placed in the second speed position.

3.3.1. RATCHET DRUM

The geometry of the drum is formed by a cylindrical shaft with different circular sections. This is designed to be mounted on two bearings, located at each end of the part. For displacement of the guided pin, the shaft has an eccentric geometry with through notches. At the opposite point, the shaft is machined with two notches to allow the coupling of the pawl.

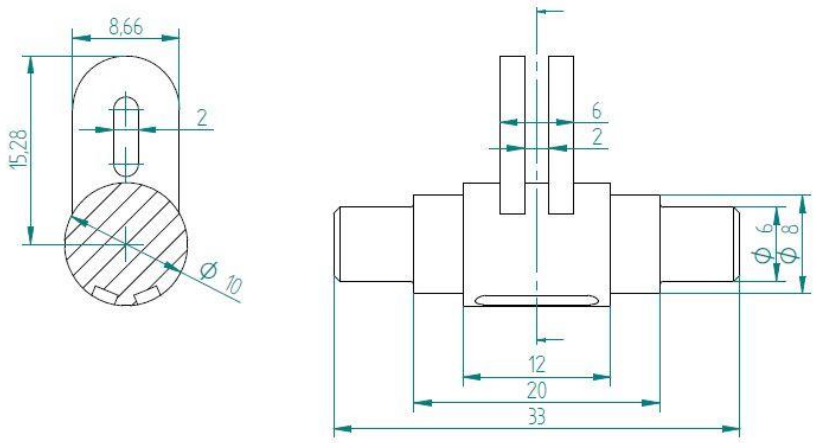

Figure 72. First model dimensions of the ratchet drum part. Source: Own elaboration.

STATIC ANALYSIS

The analysis of the mechanical performance will focus on studying specific sections of the drum. Since the part is formed by a longitudinal axle body, this geometry must be evaluated to obtain the most strained.

Furthermore, as the eccentric guiding geometry have reduced areas, compared to the axle body, this may affect the functioning of the part, even producing mechanical failures. In figures 73 and 74 are presented the reactions produced among the drum, as well as the sections to be analyzed, for every free body diagram.

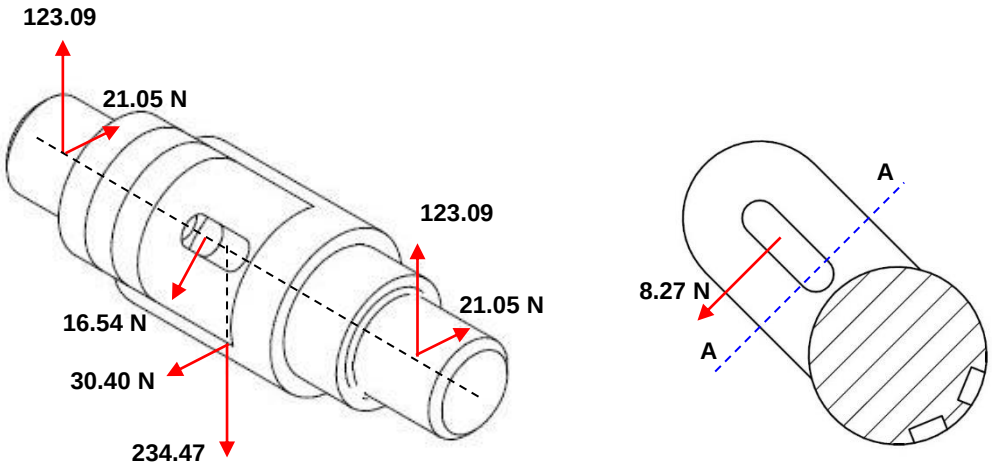

Figure 73. Left: Equilibrium produced in the selector drum during the states 1 and 3; Right: Section and force applied to the contact point of the guided pin. Source: Own elaboration.

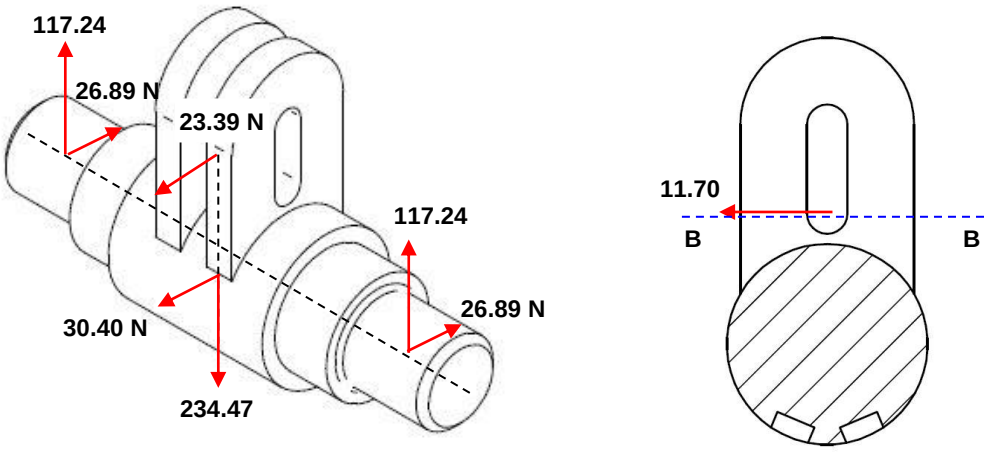

Figure 74. Left: Equilibrium produced in the selector drum during the states 2 and 4; Right: Section and force applied to the contact point of the guided pin. Source: Own elaboration.

To begin with, sections A and B are strained by a lateral load that generates a shear stress. In addition, in section A, a bending momentum is also generated which gives rise to axial stresses. The following figures show the calculation results obtained using the formulas [f.16] and [f.17].

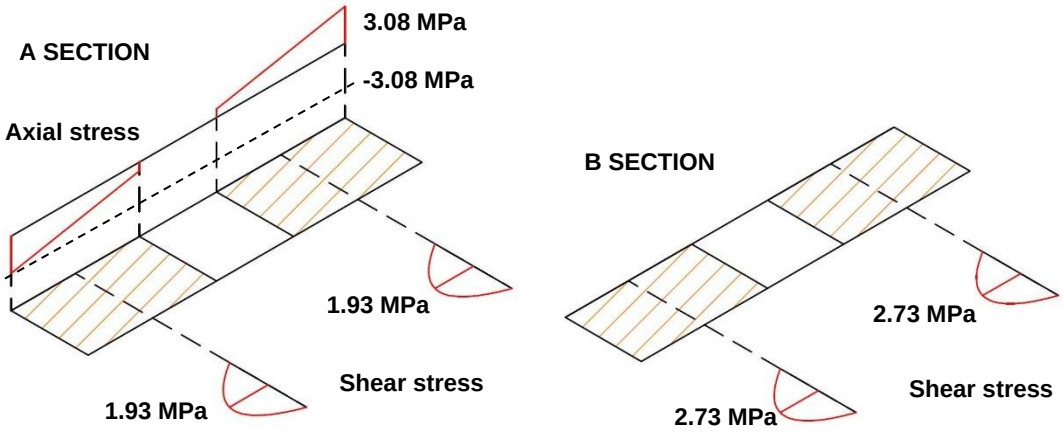

Figure 75. Diagrams of maximum stresses in section A and B. Source: Own elaboration.

As shown in table 5, the resulting stresses do not compromise the part. Be noted that the values obtained, according to the theory of Von Mises, for neutral fibers are greater than the main stresses of other points.

	Section A	Section B
Lateral load [N]	8,27	11,7
Bending moment [Nmm]	22,25	0,00
Maximum bending stress [Mpa]	1,06	0,00
Maximum shear stress [Mpa]	1,93	2,73
Von Mises stress in neutral fiber [Mpa]	3,51	4,73
Principal stress in edge fiber [Mpa]	1,06	0,00

Table 6. Results of the analysis on the eccentric guide. Source: Own elaboration.

On the other hand, with respect to the cylindrical body of the drum, the free body diagrams allow to calculate the different bending and shear loads that are generated along its length. Figure 76 shows the loads in equilibrium together with the bending and shear diagrams. Also be noted that loads distanced from the center, such as the contact load in the guide, have been moved to the center for calculation.

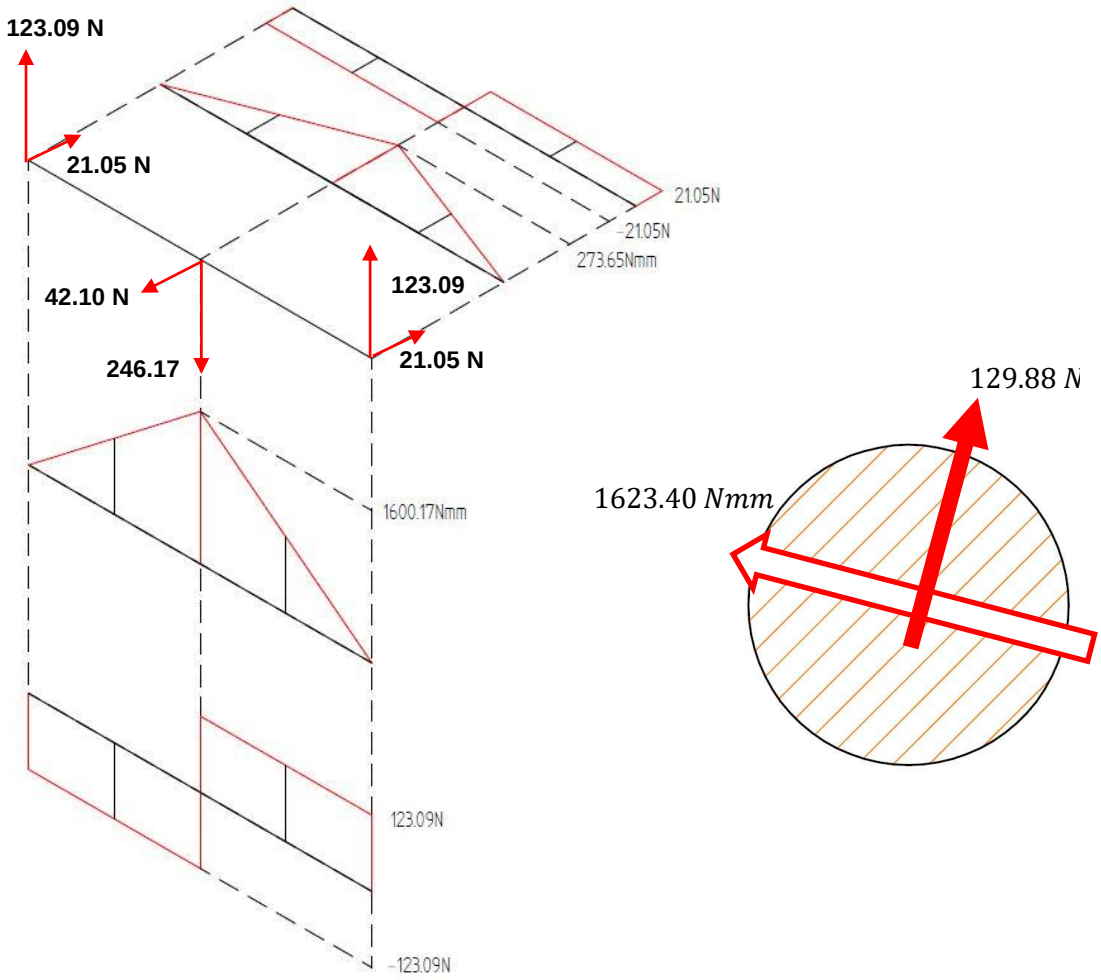

Figure 76. Left: Diagram of bending and shear strains of the drum for the states 1 and 3. Right: Reaction produced on the midpoint of the shaft. Source: Own elaboration.

The figure represents the loads generated during states 1 and 3, since during them the loads obtained reach the maximum value. In addition, the most strained section of the part is represented, which is the central point of its length. This condition also occurs during the other states of work.

The formulas [f.16] and [f.17] calculate the maximum stresses in the critical section. The following figure presents these results, obtaining a maximum value de 16.54 MPa produced by bending at the top and bottom points.

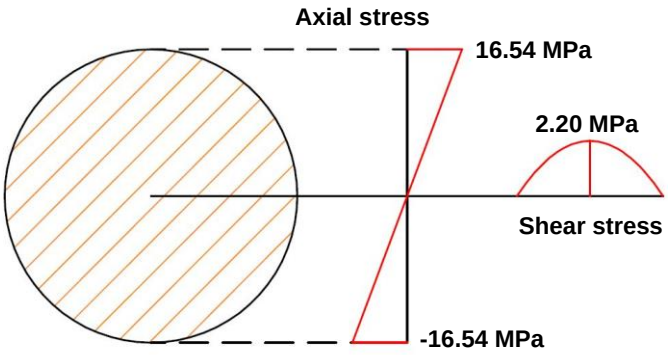

Figure 77. Diagrams of maximum stresses in the midpoint section of the drum shaft. Source: Own elaboration.

To sum up the static analysis, none of the stresses obtained in the sections studied, generate a risk of failure in the performance of the selector drum.

DYNAMIC ANALYSIS

Dynamically, the maximum performance points, studied in the static analysis, have dynamic load curves as presented in figure 78. From them, alternating stress and average stress are obtained.

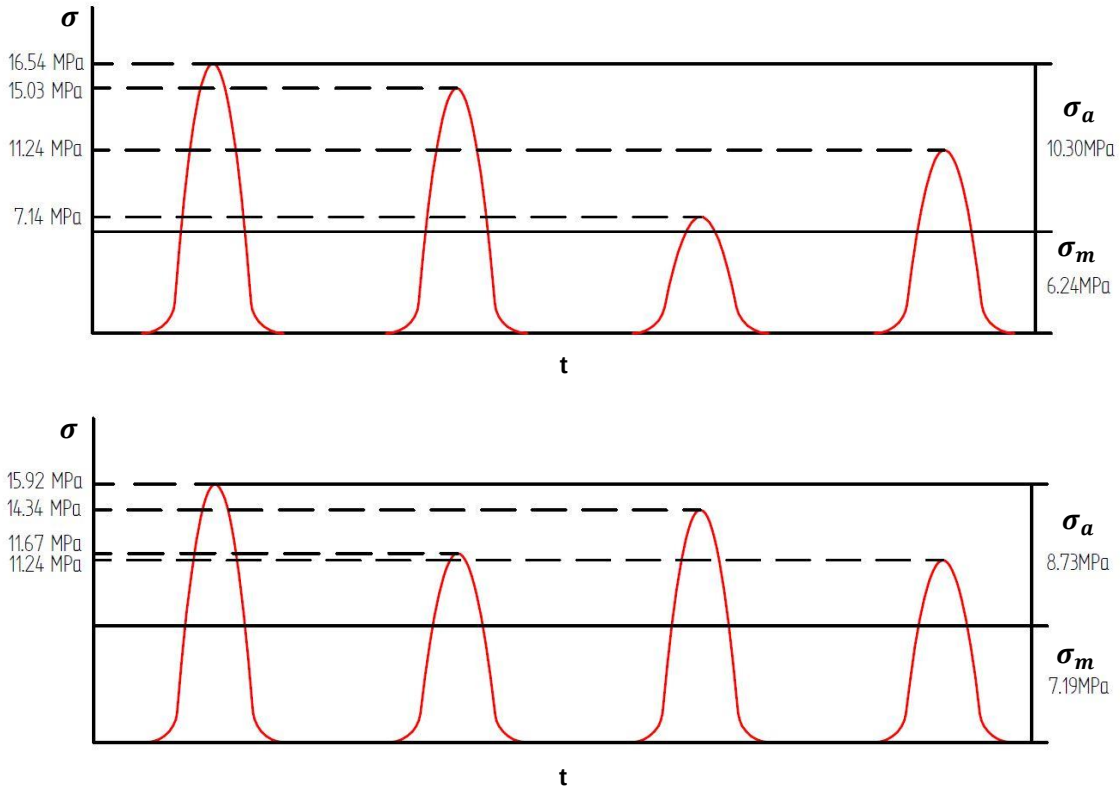

Figure 78. Graph of dynamic stresses in the midpoint of the joint shaft. Top: States 1 and 3; Bottom: States 2 and 4. Source: Own elaboration.

Since the drum rotates at intervals of $22.5°$, as the stresses change, each affected fiber is affected by different strains. Due to the variation of values in the graphs, it is unknown which of the two points work the worst due to fatigue. Therefore, both will be analyzed using the Goodman diagram.

For the calculation of fatigue strength, must consider the features of the part and the critical section. The drum must be machined by rectifying, while the critical section, with $10\,mm$ diameter, works by pure bending. Under these conditions, the fatigue strength obtained, for the material selected, is $90.27\,MPa$.

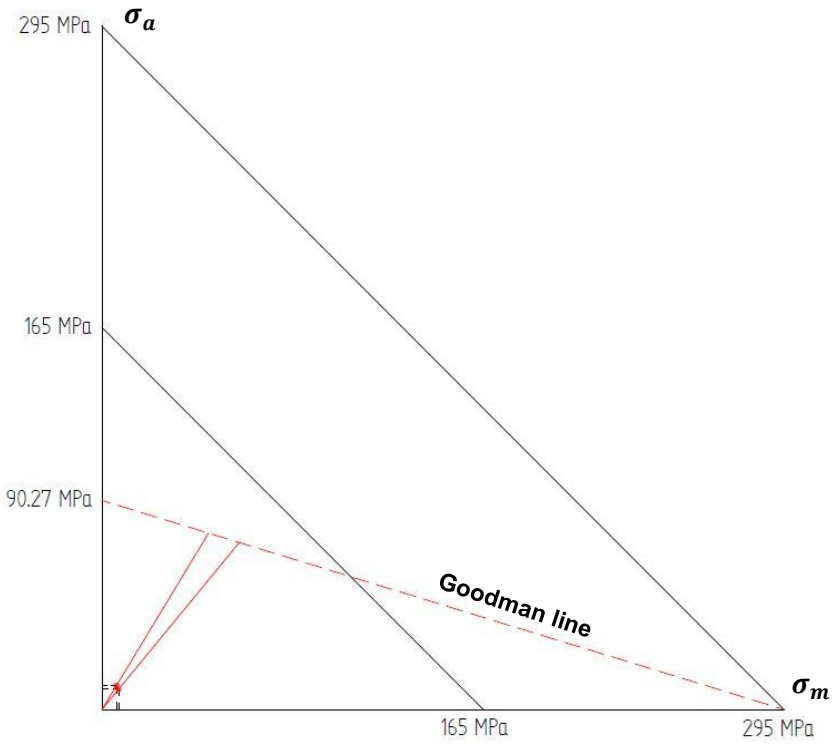

Figure 79. Goodman diagram for the midpoint section of the joint shaft. Source: Own elaboration.

The diagram of figure 79 shows that the drum part is loaded significantly under the Goodman limit line, with a safety factor calculated to be around 7.

BEARING CALCULATIONS

To conclude the design of the ratchet drum, the work of the bearings must be evaluated by calculations in relation to their life expectancy. The bearing dimensions are $6\,mm$ internal diameter, $19\,mm$ external diameter and $6\,mm$ width.

Figure 80. Rendered view of model 626 of standard bearings. Source: [51].

According to static analysis, the reaction generated is higher during states 1 and 3. As shown in the figure 76 the load applied to the shaft is a $124.88\,N$ radial force. On the other hand, the axial reaction of the bearing is zero, since the shaft does not apply any load in that direction.

To make the calculations, two bearing features must be considered: the static load capacity C_o and the dynamic load capacity C. Formula [f.18] calculates the safety factor for static bearing work, while formula [f.19] is used for dynamic analysis.

$$Safety\ factor = \frac{C_o}{P_o} \quad \text{[f.18]}$$

$$L = \left(\frac{C}{P}\right)^p \quad \text{[f.19]}$$

$C_o - Static\ capacity\ [N]$.
$P_o - Static\ load\ [N]$.
$C - Dynamic\ capacity\ [N]$.
$P - Dynamic\ load\ [N]$.
$L - Bearing\ useful\ lifetime\ [10^6\ revolutions]$.
$p - Life\ factor\ (3\ for\ rigid\ ball\ bearings)$.

Regarding the static capacity, which is $1040\,N$ for the bearing used, the safety factor obtained is 8.3. As for its service life, applying the load of $124.88\,N$ and the $2550\,N$ dynamic capacity in the formula [f.19], the resulting value is $8.5 \cdot 10^9$ total revolutions. Keeping in mind that for every activation of the mechanism, the drum rotates $22.5°$, the bearing is able to withstand $136 \cdot 10^9$ gear changes.

Since these service life values are so extremely high, it can be considered that the bearing will never fail throughout its use, as other parts of the bicycle would normally fail first.

For example, assuming a total use of twenty gear shifts per bicycle routine and three trips per week as use frequency, the bearings will be able to withstand up to $40 \cdot 10^6$ years.

MECHANICAL SIMULATIONS

In the simulations, both ends of the shaft, where the bearings are mounted, are defined as fixed points, while the forces are defined for the contact points of the pawl and the guided pin.

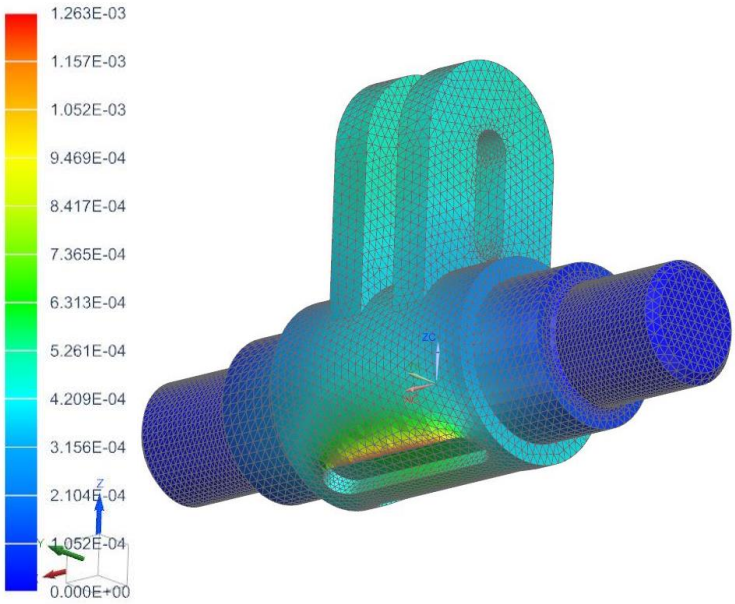

Figure 81. Resulting deformations obtained for the ratchet drum. Source: Own elaboration.

Regarding the simulations, the maximum deformations obtained are about $10^3\ mm$. Besides, the resultant figures present unexpected critical points. The point of contact with the pawl, stresses up to $94.11\ MPa$ are produced, while the rounded section of the bearings present a stress concentration around $30\ MPa$. The 1.8 safety factor is considerably high.

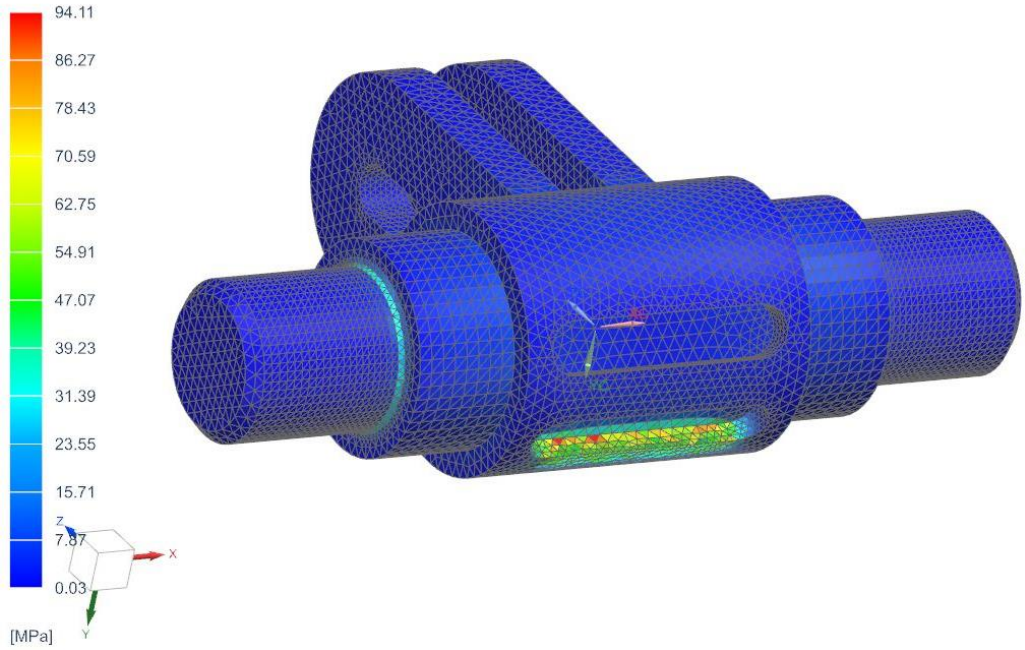

Figure 82. Resulting stresses obtained for the ratchet drum. Source: Own elaboration.

3.3.2. GUIDED PIN

The eccentric guide of the drum has the function of moving the articulated joint of the connecting rod, transmitting the movement to the rest of the mechanism. Since a movable guide confers two degrees of freedom on the joint, this part of the connecting rod must be restricted to one single degree of freedom, by another horizontal fixed guide. In this way, the rotary movement of the selector drum allows the joint to move through the fixed guide.

To accomplish these conditions, the design proposal integrates a cylindrical pin that, mounted on the moving guide of the drum and the fixed guide on the bench, transmits the horizontal movement to the rest of the mechanism.

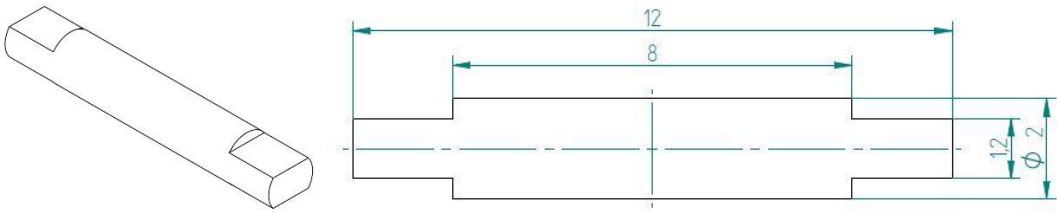

Figure 83. First model dimensions of the guided pin part. Source: Own elaboration.

STATIC ANALYSIS

As calculated above, the guide pin, as well as the rest of the parts, have different free body diagrams depending on the position and movement in which they are operating. Therefore, the static analysis will focus mainly on the state that presents the highest strains.

After drawing and comparing the stress diagram for every state, the forces generated reach its maximum value for state 2, when the third gear is activated. On the other hand, regardless of its position, the critical section of the part is located at the midpoint of the axis. In this, bending and shear forces are generated.

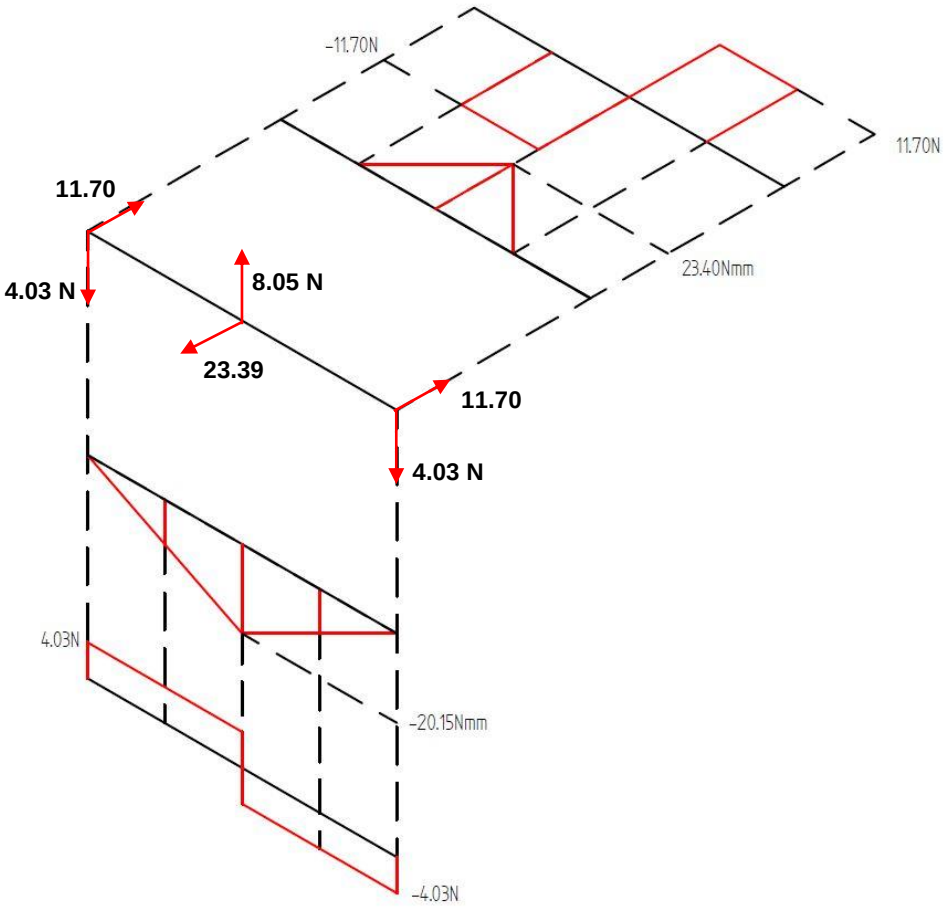

Figure 84. Diagram of bending and shear strains of the drum for the state 2. Source: Own elaboration.

Figure 85 shows the stresses generated in the critical section of the pin. Be noted that, when expressing the bending and shear loads in a single force, they take different directions. Therefore, both vectors are separated by a $22°$ angle. Considering this, the figure is not entirely accurate. However, in order to avoid failure, and since the angle is small, these values will be used to calculate the safety factor, by means of the Von Mises' failure theory.

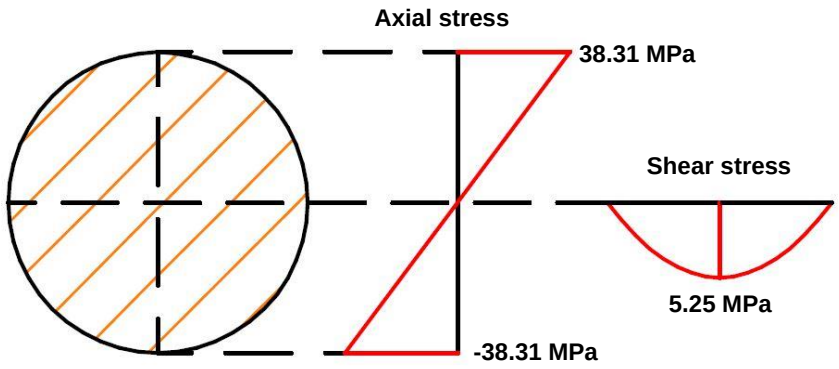

Figure 85. Diagrams of maximum stresses in the midpoint section of the guided pin. Source: Own elaboration.

Table 6 shows the resulting Von Mises stress. During the actual work of the pin, this bending and shear stresses do not coincide in the same point, but since they are the maximum values for each type, this result can be considered. The safety factor obtained is 4.1.

	Critical section
Lateral load [N]	12,38
Bending moment [Nmm]	30,09
Maximum bending stress [Mpa]	38,31
Maximum shear stress [Mpa]	6,11
Von Mises stress in neutral fiber [Mpa]	39,74

Table 7. Results of the analysis on the guided pin. Source: Own elaboration.

DYNAMIC ANALYSIS

The dynamic work of the guided pin is based on the shift between the three speeds, which generate four different free body states. For each state, the values and directions of the bending loads are varied, and some of them are negligible. As for the shear stresses, their influence is minimal, as shown in table 6, and therefore, they will not be considered for the fatigue analysis.

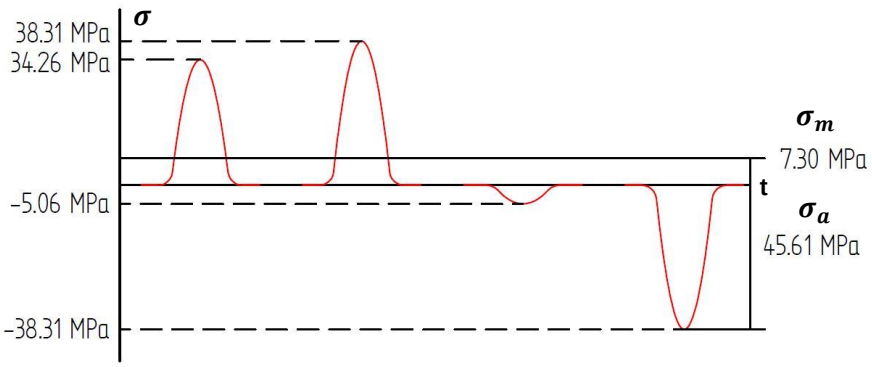

Figure 86. Graph of dynamic stresses in the midpoint of the guided pin. Source: Own elaboration.

The figure shows the dynamic load curve that appears in the critical fiber studied during the static analysis. From these, the values of alternating stress and average stress are also obtained.

For the calculation of fatigue strength, new conditions shall be taken into consideration. The $2\,mm$ width diameter, the machined manufacturing, and the pure bending, are the conditions that affect the fatigue strength of the pin. As a result, a $106.20\,MPa$ limit is obtained.

As shown in the Goodman diagram, in this analysis the average stress is not as relevant as the alternating stress. Regarding the performance of the part, it works at a 2.2 safety factor, which is a very suitable value.

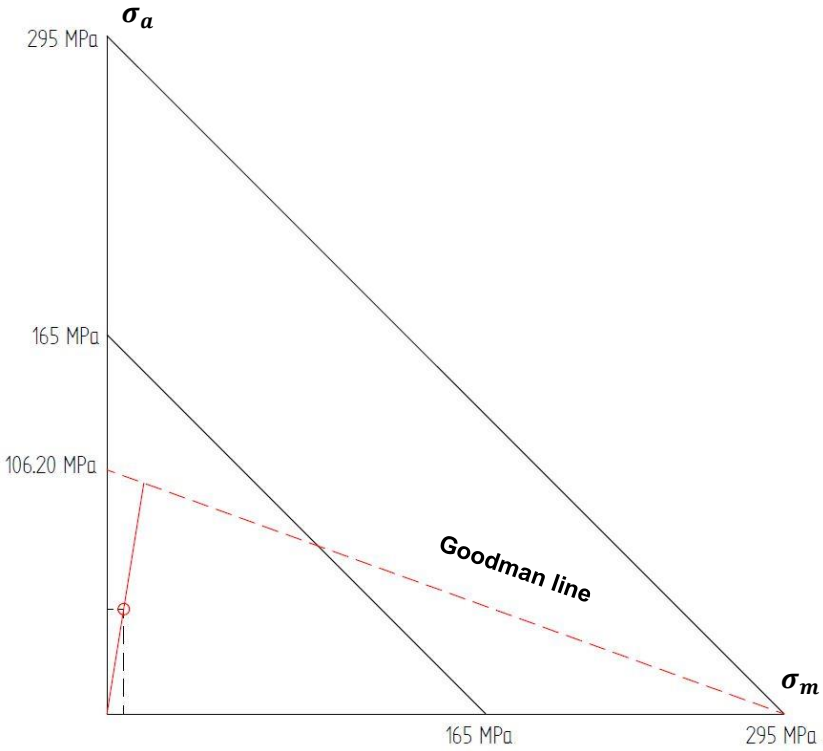

Figure 87. Goodman diagram for the midpoint section of the guided pin. Source: Own elaboration.

MECHANICAL SIMULATIONS

As shown in figure 88, the results in the simulations are very close to the values calculated theoretically. These do not appear at the midpoint of the length of the piece, but they do occur in the contact area of the connecting rod.

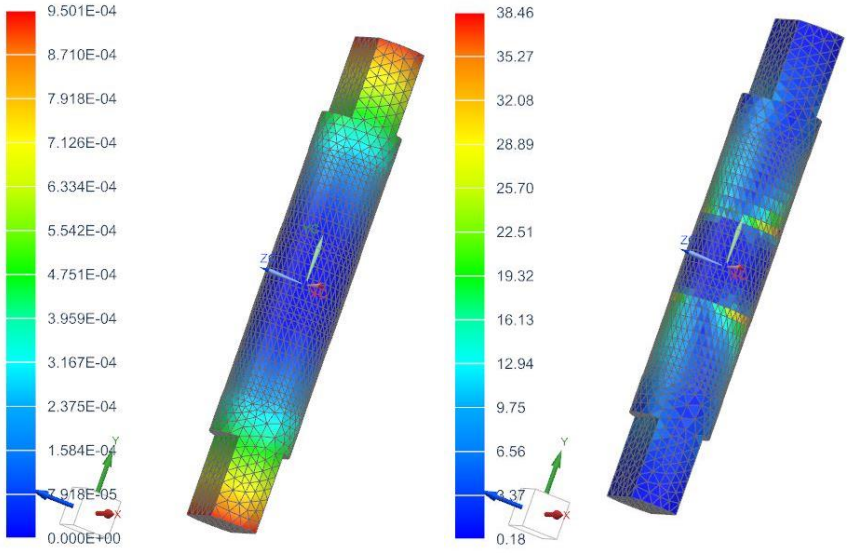

Figure 88. Simulation results obtained for the guided pin. Source: Own elaboration.

3.3.3. CONNECTING ROD

The connecting rod is the part that transmits the rotating movement from the drum to the indicator rod, as translation displacement. Since this part is only loaded in two articulated points, the force transmitted has the same direction as this segment.

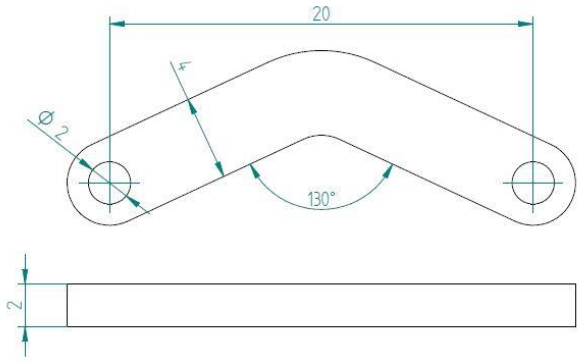

Figure 89. First model dimensions of the connecting rod. Source: Own elaboration.

STATIC ANALYSIS

As calculated above, this rod works the hardest during the state 4, when the mechanism moves from the second speed to the first one. In these, the axial load applied to the joints of the part is a $24.74\ N$ stretching force. During the state 2, this load is applied as a compression force. Since the stretching load would produce a stress concentration, this will be the state studied.

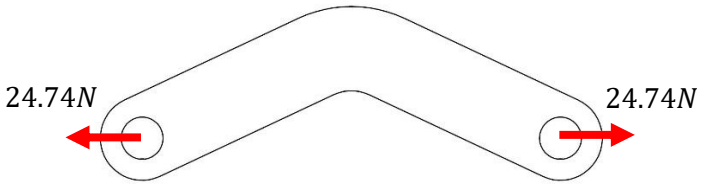

Figure 90. Connecting rod equilibrium for the state 4. Source: Own elaboration.

As the part is shaped with a $130°$ elbow, this may produce a bending stress in the midpoint sections. Therefore, the section of the elbow, as well as the joint section, will be analysed.

As the $24.74\ N$ stretching force is displaced $4.25\ mm$ from the neutral fiber of the midpoint section, it produces a $105.15\ Nmm$ momentum. Both loads produce a $42.52\ MPa$ maximum stress in the internal fiber, as shown in figure 91. For the compression case, the diagram would be drawn symmetrically.

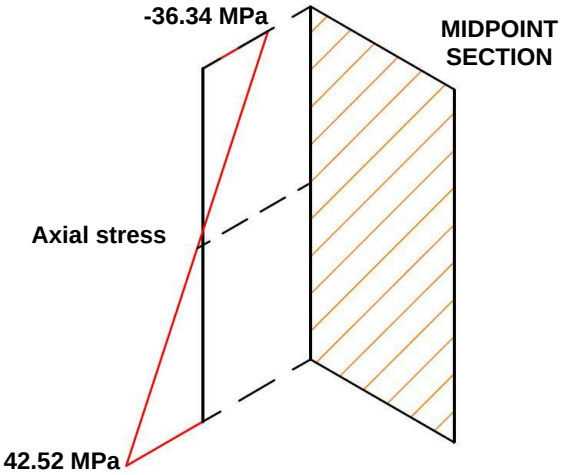

Figure 91. Diagrams of maximum stresses for the elbow section of the connecting rod. Source: Own elaboration.

By means of the graph in the figure 43, it has been defined a 2.2 value for the stress concentration factor. As shown in the following figure, the axial stress produced in the joint, in normal conditions, is a $6.19\ MPa$ stretch, while the concentrated stress, generated in the bore fibers has a $13.61\ MPa$ total value.

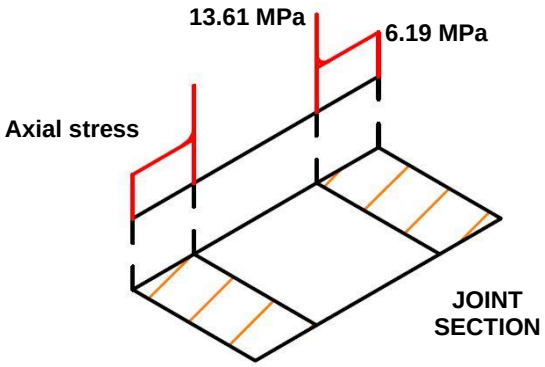

Figure 92. Diagrams of maximum stresses for the joint section of the connecting rod. Source: Own elaboration.

As the concentrated stress does not exceed the ones produced by the bending, the midpoint section can be considered the critical work point of the rod. From the resulting maximum stress, a 3.8 safety factor is obtained.

DYNAMIC ANALYSIS

Considering the four states, the dynamic load graph is drawn as shows the figure 93. The parabolic curves, which form the graph, are symmetric about the abscissa axis. This means that the average stress is cero, while the alternate stress coincides with the highest value on the curve.

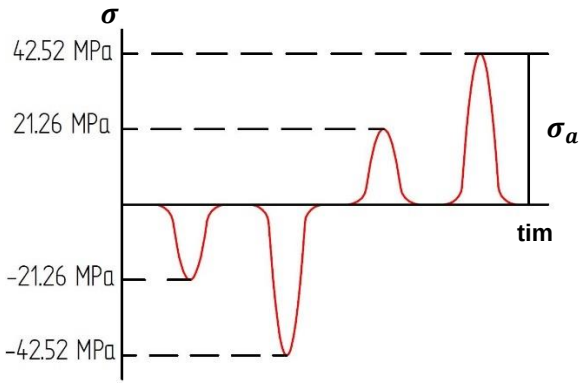

Figure 93. Graph of dynamic stresses in the midpoint of the connecting rod. Source: Own elaboration.

Since the design and manufacturing characteristics of the connecting rod are the same as for the slider and switching parts, the fatigue strength obtained is $95.58\ MPa$.

Figure 94 shows the consequence of the values obtained for the average and alternating stresses. As the average is zero, it has no effect on the dynamic work of the part. On the contrary, the alternating stress have greater relevance since it moves the working point towards the Goodman line. Even so, the working point is at a safe distance from the fatigue limit line.

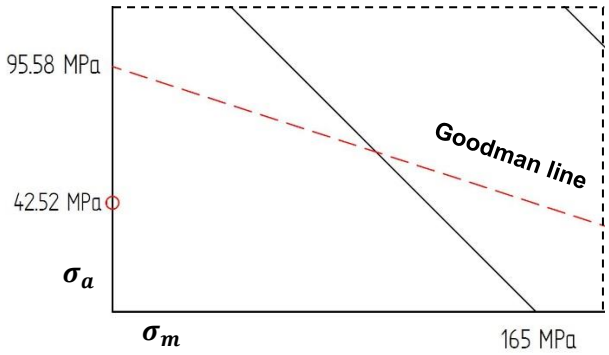

Figure 94. Goodman diagram for the midpoint section of the connecting rod. Source: Own elaboration.

MECHANICAL SIMULATIONS

The configuration of the connecting rod for simulation is simple since the applied loads are reduced to the two articulated points. While one of them must be kept fixed, the load is placed on the free joint, in the direction described by both ends.

For the simulations, both the stretching and the compression situations have been studied. The figure 97 shows how the connecting rod is strained by a $34.59\ MPa$ maximum stress, for both situations. This value contrast with the calculated since it is lower. In conclusion, the rod works correctly with a high safety factor.

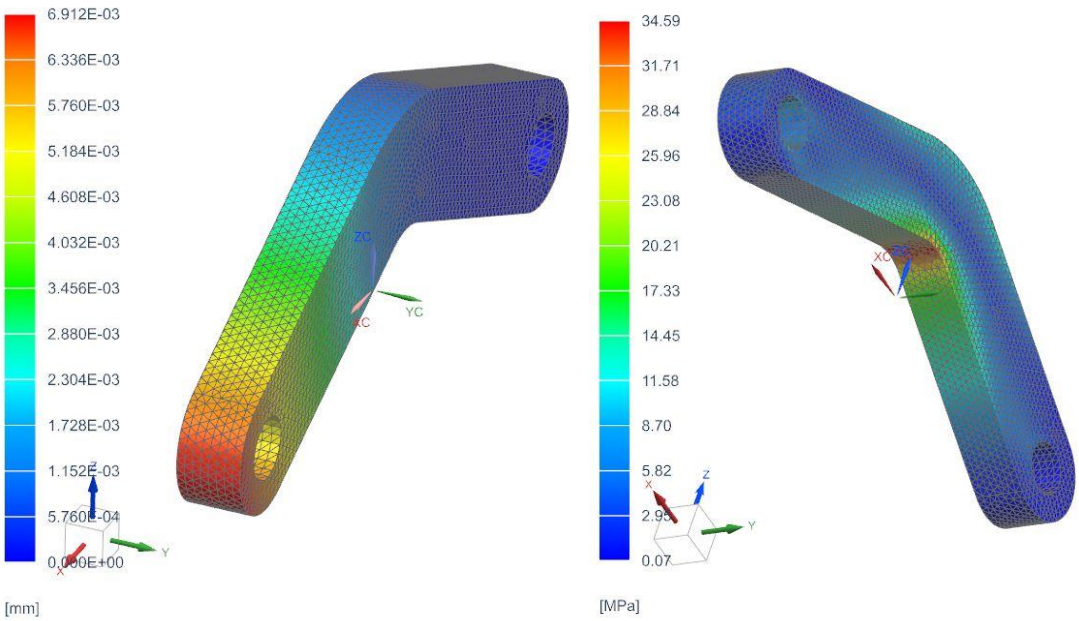

Figure 95. Simulation results obtained for the connecting rod. Source: Own elaboration.

3.3.4. INDICATOR ROD

The indicator rod is the part that connects the designed mechanism with the internal system of the gearing hub. This is connected to the connecting rod by means of a tubular rivet and is coupled to the clutch pin from a $M2{,}3$ metric thread.

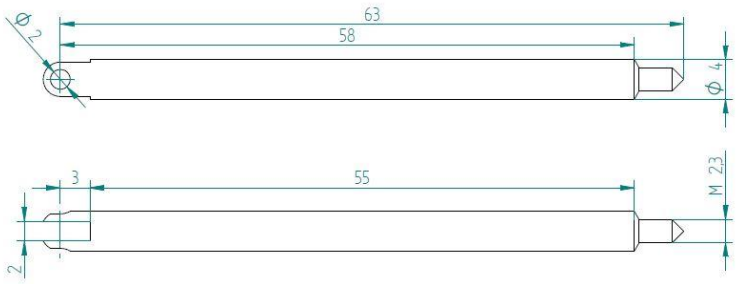

Figure 96. First model dimensions of the indicator rod. Source: Own elaboration.

STATIC ANALYSIS

The indicator rod works in a similar way to the connecting rod. The transmitted force is the same but, since it is angled with respect to the axis of the piece, a bending reaction applied to the whole body appears.

As well as the connecting rod and the guided pin, the indicator rod is affected by different loads depending on the working state of the mechanism. These loads reach their maximum during states 2 and 4, in which a $24.74\ N$ force is transmitted and a bending reaction of $466.90\ Nmm$ is produced. Considering that during state 4 the piece works by stretching, the analysis will focus on this to consider the stress concentrations.

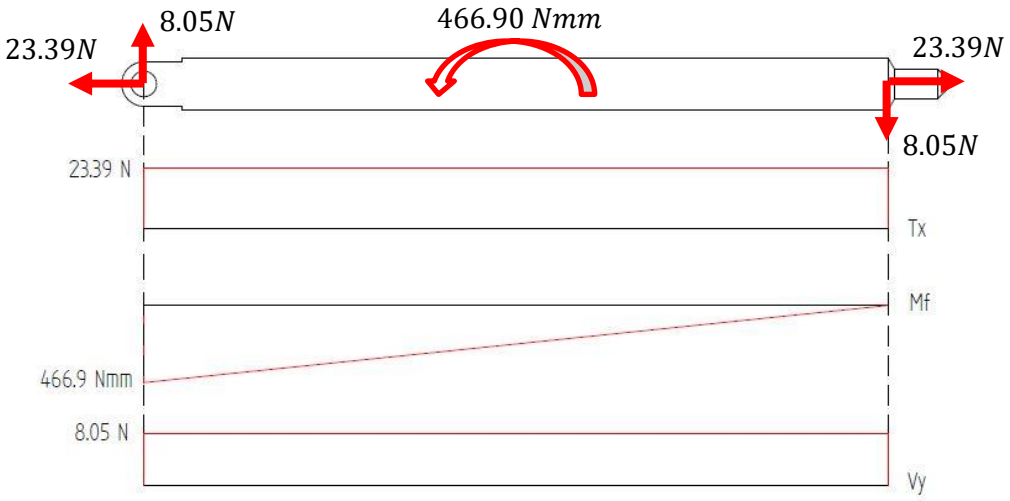

Figure 97. Diagram of strains produced on the indicator rod for the state 4. Source: Own elaboration.

Although, as shown in figure 97, the bending moment diagram appears to be reduced in value at the threaded joint, this is an effect produced by the bending moment of $466.90\ Nmm$, which is constant along the part. If the same calculation of diagrams is performed in the opposite direction, the results are the opposite: the threaded joint is fully loaded while the joint is not affected. In any case the maximum value in the entire part can be considered the same.

For the analysis, the two joints of the piece will be considered, since these have smaller dimensions than the main cylindrical body. Figure 98 shows the section of the articulated joint, in which the bending stresses are significantly high. When compared to the properties of the material, it turns out that these stresses cause failure with great certainty. Since the part seems to fail due to the reduced working area, a new geometric proposal is made for this rod.

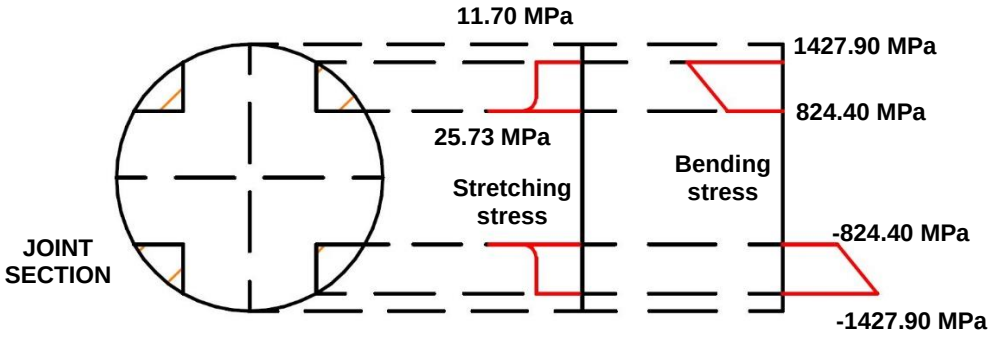

Figure 98. Diagrams of maximum stresses for the joint section of the indicator rod. Source: Own elaboration.

The proposed modification is based on the redesign of the joint end. The new indicator rod has a section change, with square area, at this end. By means of this change, the working area is larger, and its moment of inertia increases.

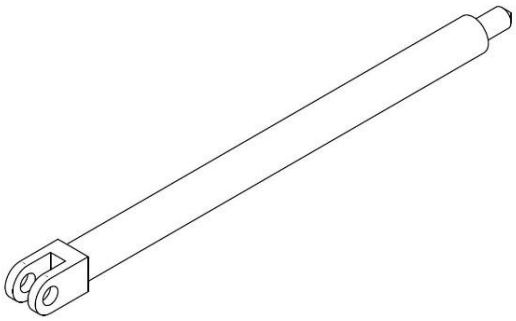

Figure 99. Isometric view of the new model of indicator rod. Source: Own elaboration.

Figure 100 shows the new section of the joint and the stresses produced. Adding the stretching and bending, the maximum stress is $105.90\ MPa$. The safety factor obtained is 1.6.

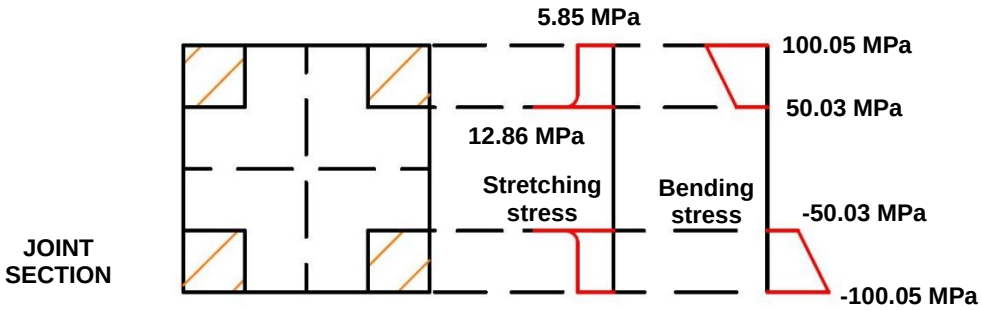

Figure 100. Diagrams of maximum stresses for the new joint section of the indicator rod. Source: Own elaboration.

Regarding the threaded joint, the tensions obtained are those shown in the following figure. Again, the bending of the piece causes the greatest strains, reaching a maximum value of $396.51\ MPa$.

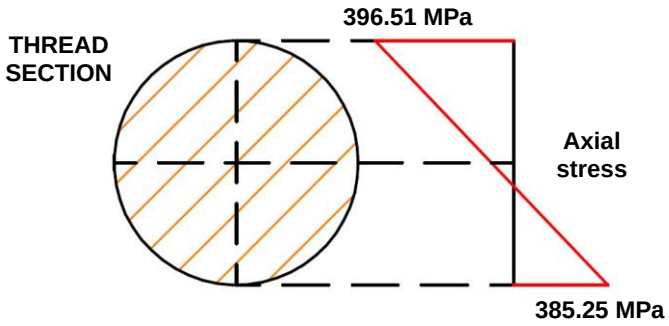

Figure 101. Diagrams of maximum stresses for the threaded joint section of the indicator rod. Source: Own elaboration.

This stress exceeds the elastic limit of the material and therefore a new corrective measure must be taken. Since the part must be attached to the clutch pin, which already exists, the failure area cannot be modified and therefore a change of material for one with better properties must be considered. To obtain a 1.4 safety factor, the yield strength of the material must be over $555\ MPa$. However, considering the following dynamic analysis, the chosen material must have even greater properties.

DYNAMIC ANALYSIS

The following graph shows the dynamic strains produced in the most loaded section, in the threaded joint. Be noted that this is the same case as for the analysis of the connecting rod, where the parabolic curves are symmetric. Therefore, when applying the Goodman method, the relevant stress is simplified to the alternating component. In conclusion, for the analysis only the alternating stress must be lower than the fatigue capacity calculated.

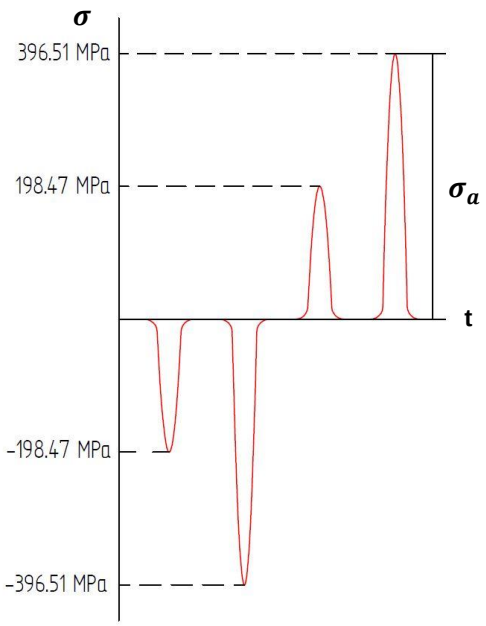

Figure 102. Graph of dynamic stresses in the midpoint of the indicator rod. Source: Own elaboration.

Considering the dimensions of the part, the application of the axial load and the manufacturing by grinding process, the fatigue strength for the stablished material is $95.58\ MPa$. Since the maximum stress is $396.51\ MPa$, the failure of the part will eventually happen.

In order to avoid this failure and accomplish the safety factor, the material must have a $1370\ MPa$ minimum ultimate strength. The water quenching and the tempering are processes used to produce hardened steels, of which ultimate strength can reach $1680\ MPa$ and higher [52].

MECHANICAL SIMULATIONS

As results of the simulations, both the strain values and the maximum stress obtained are highlighted. The maximum deformation is $0.25\ mm$, which is considerably higher than those obtained for the other parts. However, it is not considered to be a dangerous deformation for the operation of the mechanism.

Regarding stresses, the results coincide with the expected according to calculations. These are produced in the thread section with a maximum $378.79\ MPa$ stress. For the water quenched steel with a $1500\ MPa$ yield strength, the safety factor is calculated to be 3.8.

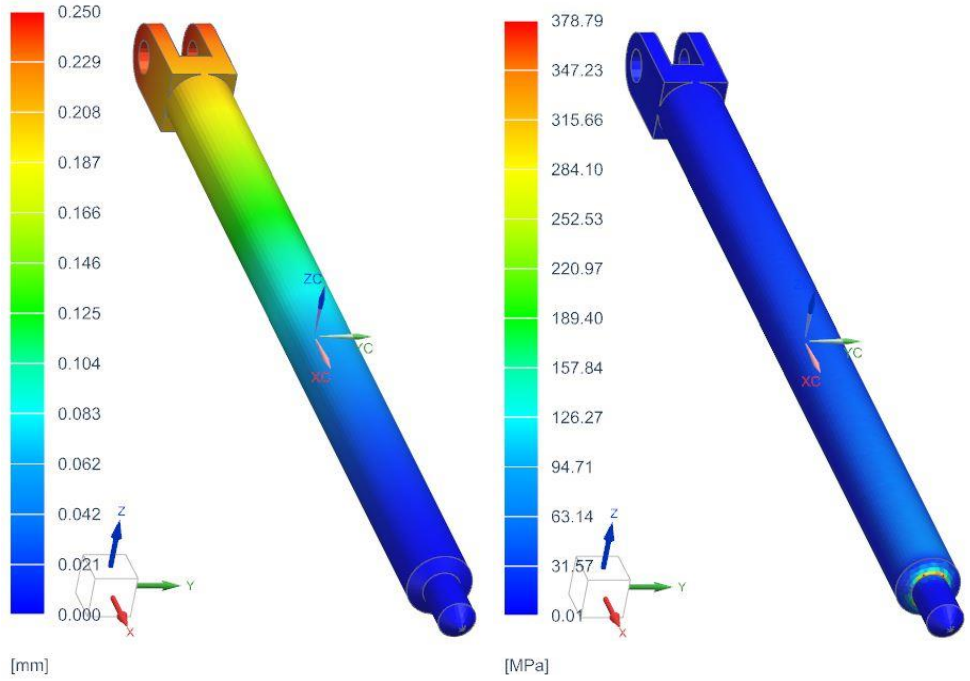

Figure 103. Simulation results obtained for the indicator rod. Source: Own elaboration.

3.4. CASE DESIGN

From the mechanism already designed, it is only necessary to define the bench elements, which will function as the structural base of the product and will allow the whole assembly to be fixed in its correct position.

Within this group, the parts that must be designed are the axle on which the sliding piece moves, and the set of housings that encloses all the other elements. Apart from these, the housing must be fixed by threaded elements, such as bolts and nuts.

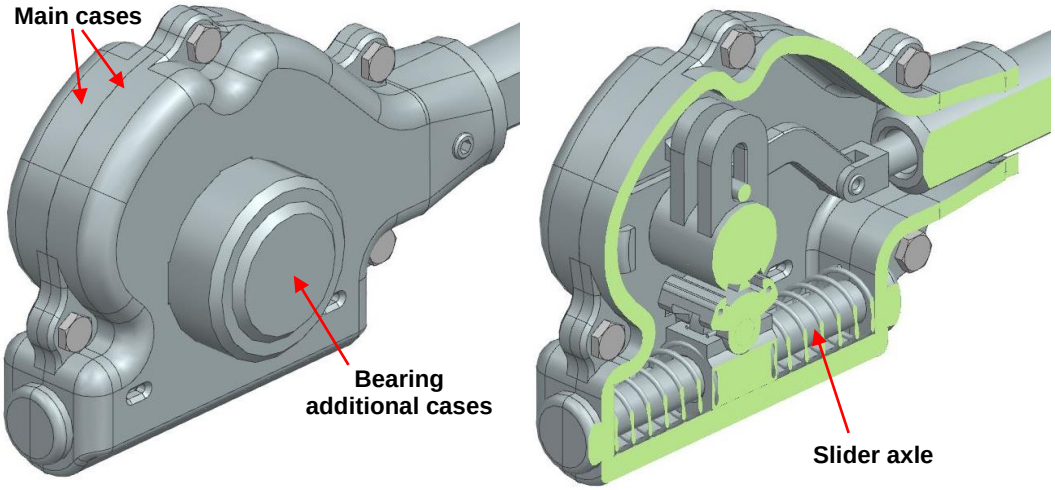

Figure 104. First 3D model of the case assembly. Source: Own elaboration.

3.4.1. SLIDER AXLE

This part is based on a simple $44\,mm$ length cylindrical shaft. This is mounted fixed to the housing, on two contact points, one at each end. On the other hand, the sliding part moves through the shaft exerting a load through it.

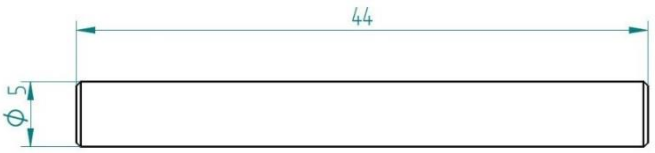

Figure 105. First model dimensions of the slider axle. Source: Own elaboration.

STATIC ANALYSIS

The initial position of the slider is at the midpoint of the axis. When the mechanism is activated, the switching pawl engages the selector drum transmitting the forces to the slider part and its axle.

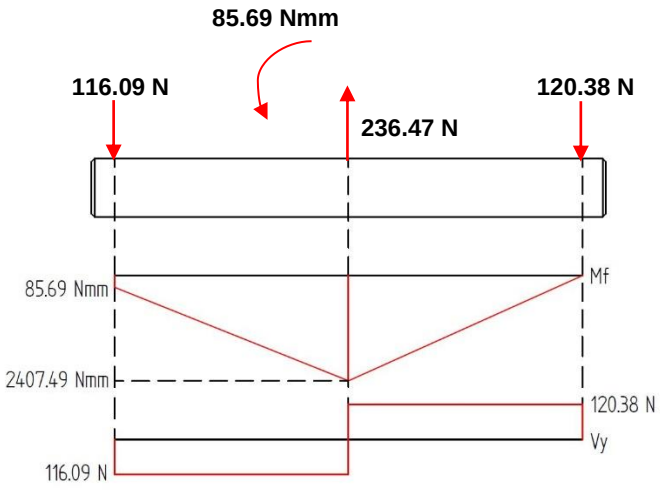

Figure 106. Diagram of strains produced on the slider axle. Source: Own elaboration.

Figure 106 shows the $236.47\ N$ force and the $85.69\ Nmm$ moment, applied by the slide at the instant of the pawl contact. In practice, the vertical load is distributed along the contact surface between the two parts, but it is considered a point force since the resulting stresses are higher in this case, increasing the margin with respect to the failure.

As reactions, vertical forces appear at the points fixed to the bench. From these loads, bending and shear diagrams show that the most strained section of the part is the midpoint of the axle length. In the critical section appears a $2407.49\ Nmm$ bending momentum and a $120.38\ N$ lateral load, maximum values throughout the axle. Figure 107 represents this section, where the maximum stresses reach $196.18\ MPa$.

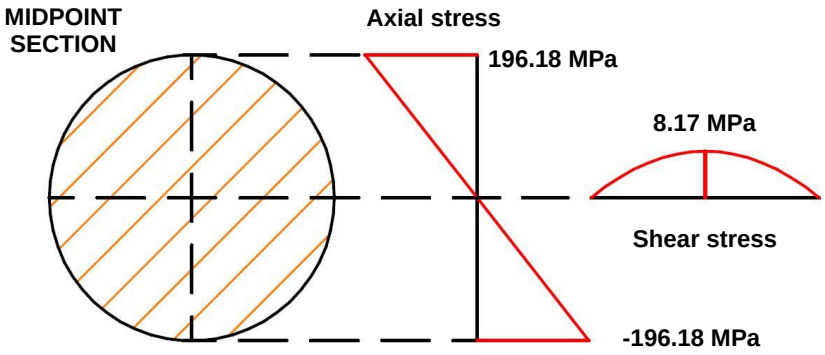

Figure 107. Diagrams of maximum stresses for the midpoint section of the slider axle. Source: Own elaboration.

Considering the material, with a $165\ MPa$ yield strength, the part will fail due to the bending load. To avoid failure, the proposed solution is to use a new material with similar properties, but a higher elastic limit. AISI 1010 steel, with $305\ MPa$ yield strength, allows the part to work with a 1.6 safety factor [53].

DYNAMIC ANALYSIS

From the operation of the mechanism, the dynamic loads applied to the axle are reduced to the same as those that appear in the static analysis. As the mechanism is activated in both directions, from the same position of the switching set, the load distribution is exactly the same. However, as the critical section is located at the midpoint of the axis, there is no influence of the different distributions on the values of the dynamic loads.

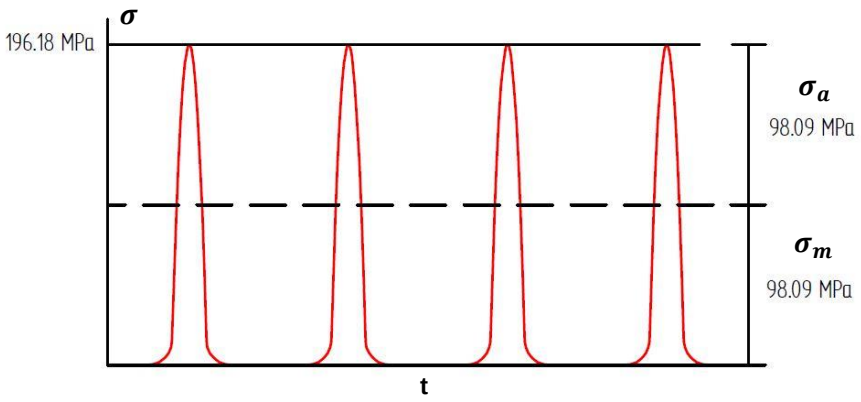

Figure 108. Graph of dynamic stresses in the midpoint section of the slider axle. Source: Own elaboration.

Figure 108 shows the progress of stresses along various speed shifts. Be noted that the maximum loads applied have the same value, resulting in equal average and alternating stresses.

For the calculation of the fatigue strength, the following aspects will be considered. The axle will be polished in order to reduce the friction between parts. Moreover, the new material is a forged steel, which reduces its fatigue limit to 50% of the ultimate strength. Since AISI 1010 have $365\ MPa$ limit, the fatigue strength of the part is calculated to be $182.5\ MPa$.

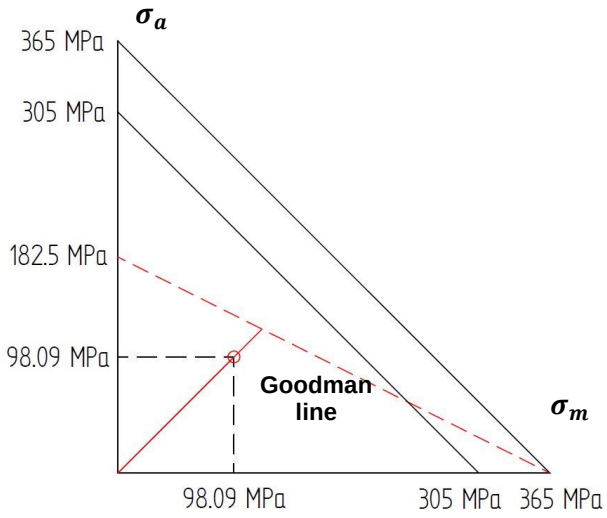

Figure 109. Goodman diagram for the midpoint section of the slider axle. Source: Own elaboration.

Theoretically, the dimensional and load factors must also be considered, but since the

diameter of the critical section is lower than $7.6\,mm$ and the loads only produce pure bending, these factors have no influence in the fatigue strength.

The Goodman diagram in the figure 109, shows that the working point is under the limit line. However, the safety factor is 1.2, which is considered too poor to reach a proper performance of the part.

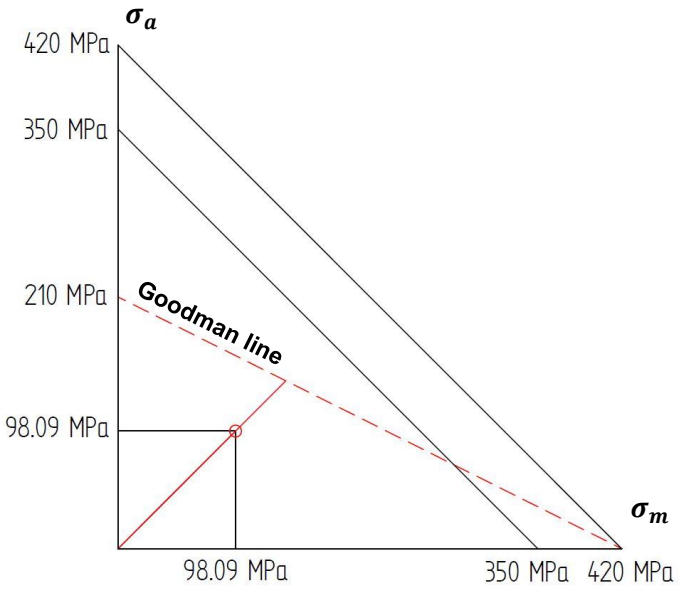

Figure 110. Goodman diagram for the midpoint section of the slider axle for the new selected material. Source: Own elaboration.

Once again, the material properties are not strong enough to allow for the correct work of the axle. In this case, the fatigue strength depends on the ultimate strength of the material used, and therefore the new material selection must focus on raising this property. AISI 1016 steel, which is produced by cold drawn, have a $420\,MPa$ strength, while its yield strength is $350\,MPa$, and have a $205\,GPa$ rigidity [54].

Diagram in figure 110 shows the influence of the new selection on the fatigue performance of the part. Be noted that the working point have moved away from the Goodman line, obtaining a more suitable 1.4 safety factor.

MECHANICAL SIMULATIONS

From the results of the simulations the maximum stresses are highlighted, which appear at the points of contact with the slider. These are lower than the values obtained in the analysis, as expected, since the load distribution used in the static analysis is not exact.

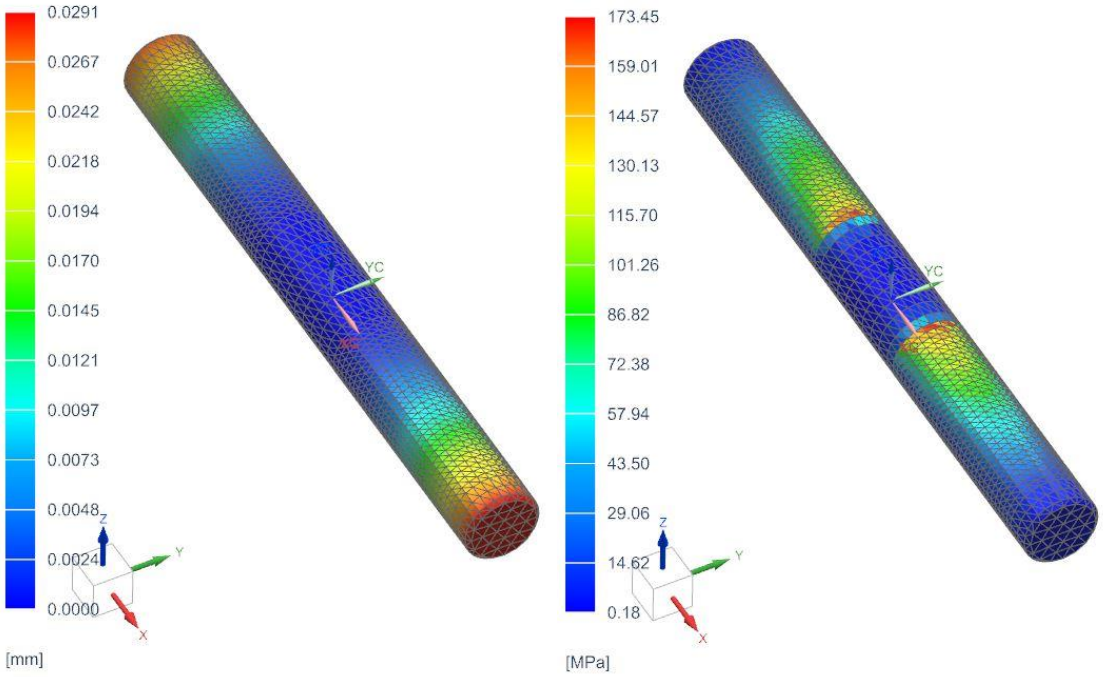

Figure 111. Simulation results obtained for the slider axle. Source: Own elaboration.

3.4.2. CASE ASSEMBLE

As for the case of the product, it will be formed by two protective pieces screwed together by some bolts. Finally, these assembly will be fixed to the axis of the bicycle by a pair of stud bolts at the end of it.

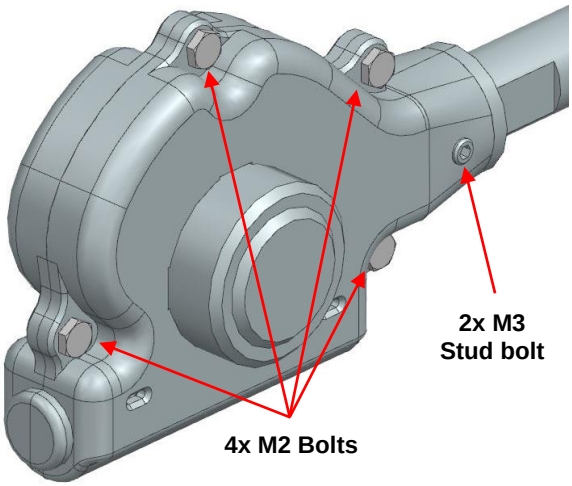

Figure 112. Bolt parts of the case assembly. Source: Own elaboration.

Since no load is transmitted inside the mechanism in the axial direction of the screws, they are not loaded externally by the assembly. However, as bolts work by stretching, unlike the studs that work by compression, the forces applied by them must be considered in balance.

On the other hand, the loads suffered by the cases because of the mechanism are based on the forces transmitted through the slide shaft and the contact with the guided pin. Keeping in mind the geometric complexity of this housing, and the different loads applied, the study of the parts will be based on the simulations, in addition to the calculation regarding the bolted joints.

THREADED JOINT CALCULATIONS

To study the behavior of the bolts, the first step is to define the mounting force necessary to ensure the correct fixation of the parts. For the screwed parts, this condition is accomplished as long as the balance of forces applied to the union of cases is not negative.

From the quality of the joining elements, the mechanical work limits for each part are obtained. Screws standardized according to DIN 933 have quality 8.8, while studs, standardized according to DIN 913 have quality 12.9. Table 7 shows the yield and ultimate strengths, corresponding to the qualities of these pieces.

Considering the 1.4 safety factor used along the project, the maximum permissible stress, or Von Mises stress, for each part is also calculated. The formulas presented below allow to calculate the maximum axial force and twisting moment to join the two cases without plastically affecting the bolt.

$$\sigma_{Adm} = \sigma_{VM} = 1.35 \cdot \sigma_T \qquad \text{[f.20]}$$

$$d_T = d - 0.938194 \cdot p \qquad \text{[f.21]}$$

$$F_M = \sigma_T \cdot \frac{\pi d_T^2}{4} \qquad \text{[f.22]}$$

$$M'_M = 0.9 \cdot M_M = 0.9(0.2 \cdot F_M \cdot d) \qquad \text{[f.23]}$$

$\sigma_T - Stretching\ stress\ produced\ in\ the\ bolt\ section\ [MPa]$.
$F_M - Axial\ load\ applied\ to\ the\ bolt\ assembly\ [N]$.
$d_T - Thread\ diameter\ [mm]$.
$p - Thread\ pitch\ [mm]$.
$M'_M - Prescribed\ maximum\ screw\ momentum\ [Nmm]$.
$M_M - Screw\ momentum\ applied\ to\ the\ bolt\ assembly\ [Nmm]$.
$d - Bolt\ metric\ diameter\ [mm]$.

As shown in the formula [f.23], the prescribed mounting momentum for threaded elements is 10% less than the theoretical moment. The following table presents the results of the formulas used and the maximum mounting loads of the screw elements.

	Bolt (8,8)	Stud bolt (12,9)
Metric diameter [mm]	2	3
Pitch [mm]	0,4	0,5
Thread diameter [mm]	1,62	2,53
Yield strength [Mpa]	800	1200
Ultimate strength [Mpa]	640	1080
Admisible stress for SF=1.4 [MPa]	457,14	771,43
Maximum thread stress [MPa]	338,62	571,43
Screw load [N]	702,05	2874,77
Screw momentum [Nmm]	252,74	1552,37

Table 8. Results of the calculations for the bolts. Source: Own elaboration.

The calculated loads correspond to the assembly of the screws if there is no separating force of the parts. Externally, there are no lateral loads that represent a risk of separation of the case, but since the bolts and the studs exert forces in different directions, each must be studied as a separating element with respect to the other.

The formula [f.24] determines that the total load exerted on the housing is equal to the difference between the mounting force of the screw and the separating force of the joint. For the separation to occur, this equality must give a negative result, otherwise the union will be maintained.

$$F_E = F_M - F_{SE} \qquad \text{[f.24]}$$

$$F_{SE} = F_S \cdot \frac{k_e}{k_e + k_c} \qquad \text{[f.25]}$$

$$d_T = d - 0.938194 \cdot p \qquad \text{[f.26]}$$

$$k = \frac{A_T E}{L} \qquad \text{[f.27]}$$

$k - Rigidity\ constant\ [N/mm]$.

Regarding the separating force, the bolted joints are affected by the load applied by the stud assembly and, therefore, the following equality can be stablished. The separating force applied to each bolt is quarter the mounting force of the studs.

$$F_S = \frac{F_M\ (stud\ bolt)}{4}$$

Continuing with the no separation condition, if the separating force is isolated in the formula [f.25] the maximum force that the union supports, before separating, is obtained. The following table shows the results obtained by using the formulas presented above.

As shown in table 8, the rigidity of the housing $200\ GPa$ corresponds to stainless steel. This material is used for the housing for its mechanical properties, its machinability, and its protection against oxidation.

	Bolt	Case joint
Young's module E [GPa]	212	200
Thread diameter [mm]	1,62	-
Thread area [mm]	2,07	9,49
Rigidity constant [10^3N/mm]	1758,10	949,40
Maximum separating load [N]	-	2002,11

Table 9. Results of the calculation of maximum separating load for a stainless-steel case. Source: Own elaboration.

In conclusion, the maximum separating force of the parts is about $2\ kN$. Taking into account that when distributing the stud mounting load in the four bolted joints, the resulting force for each union is $718.69\ N$. As this value is lower than the separating load limit, the bolts work within valid values. If, for example, the studs are assembled by a $2.5\ kN$ force, which does not exceed its limit, the minimum load required to mount the bolts is $219.16\ N$.

MECHANICAL SIMULATIONS

In order to check the work of the housings, various situations regarding the screw mounting will be simulated, according to the loads calculated above. Although the maximum mounting load of the stud bolts is $2.87\ kN$, the maximum separation load that supports the set of joints is $2\ kN$. Since the studs must ensure the immobilization of the assembly, by pressure against the axle of the internal gearing hub, the maximum load that supports the casing will be sought.

As material for these parts, the stainless steel of elastic limit $1240\ MPa$ have been selected. Considering the 1.4 safety factor, the maximum permissible stress for the part shall be $885.71\ MPa$. Therefore, simulations must give results lower than this.

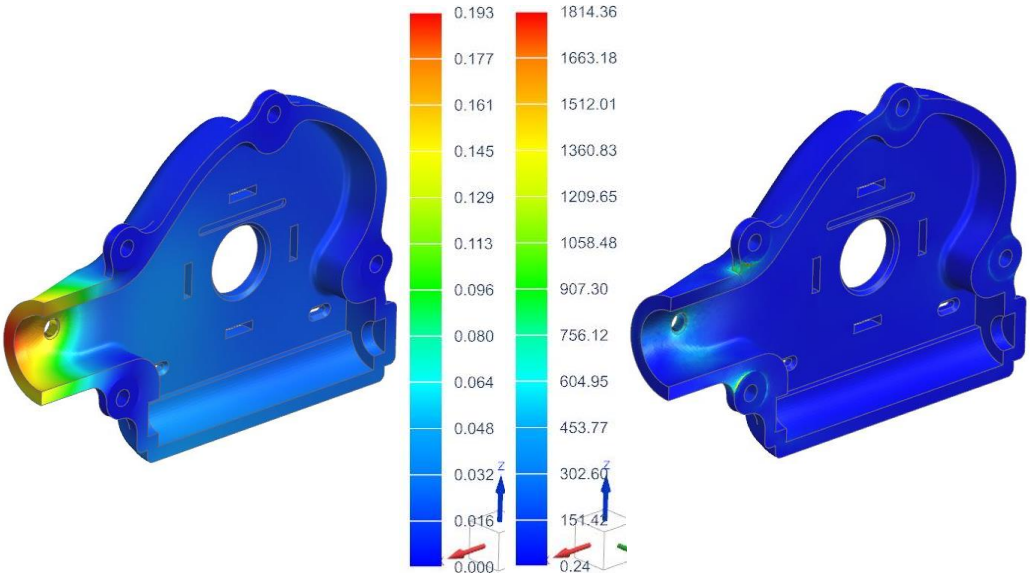

Figure 113. Simulation results obtained for the case loaded by 2000 N. Source: Own elaboration.

The simulations in figure 113, where the stud mounting load is $2000\,N$, show how the maximum stress exceeds the ultimate strength of the material. If the mounting load of the stud is reduced to $950\,N$, the maximum stress obtained in the simulations is $861.59\,MPa$, as shown in figure 114. This value is adequate to reach the security condition.

Regarding the deformations, none of the cases, the 2 tenths of a millimeter are reached at the end of the casing, where the stud is screwed. These values are acceptable, considering that the assembly is completely fixed to the hub axle.

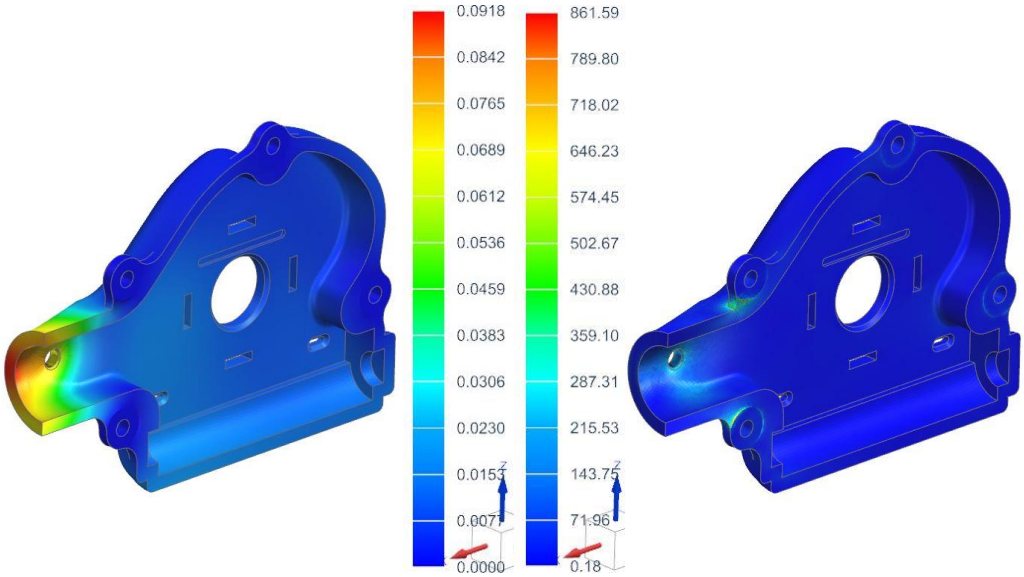

Figure 114. Simulation results obtained for the case loaded by 950 N. Source: Own elaboration.

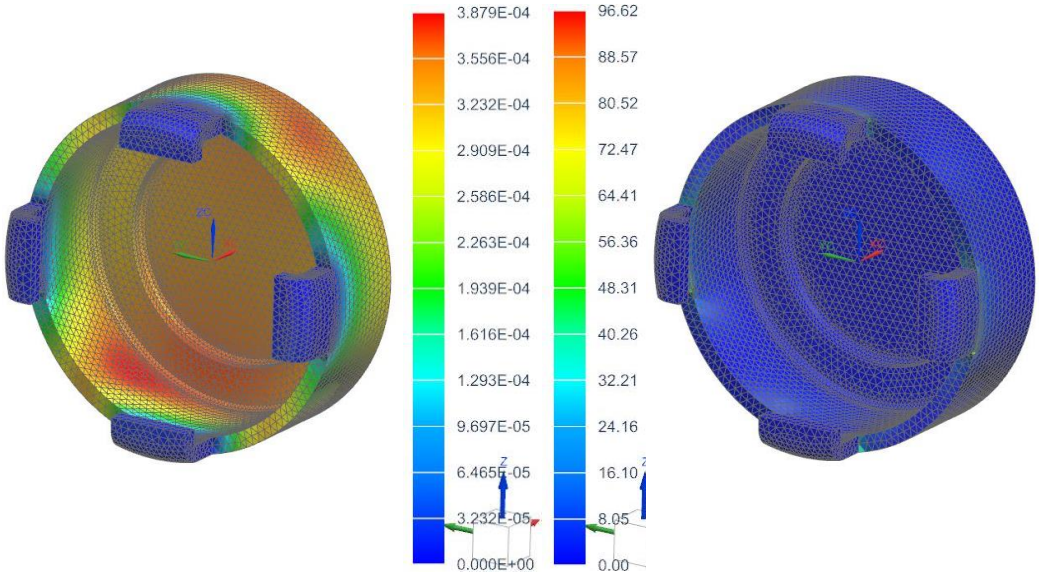

Figure 115. Simulation results obtained for bearing cases. Source: Own elaboration.

Regarding bearing cases, they must be mounted on the main housing by means of a pattern of tabs. The unique load applied to them is the radial force transmitted by the bearings. From the simulations, the results do not correspond to any compromise since both deformations and strains are limited.

3.5. KYNEMATIC SIMULATIONS

For the kinematic study, the assembly has been divided into two different mechanisms: the ratchet drive system, and the modified crank-rod-piston mechanism. Initially, the goal was to simulate the operation of the complete assembly but, due to errors generated during the resolution, it is necessary to make this separation.

In terms of configuration, the parts of the mechanism are first defined, then the kinematic pairs and finally the actuators. In the case of the ratchet assembly, a prismatic pair has been defined for the slide, a joint between it and the switching pawl, a bench joint for the selector drum, and the contact between the pawl and the drum. From these, the mechanism is calculated to have one degree of freedom, which is controlled by the actuator.

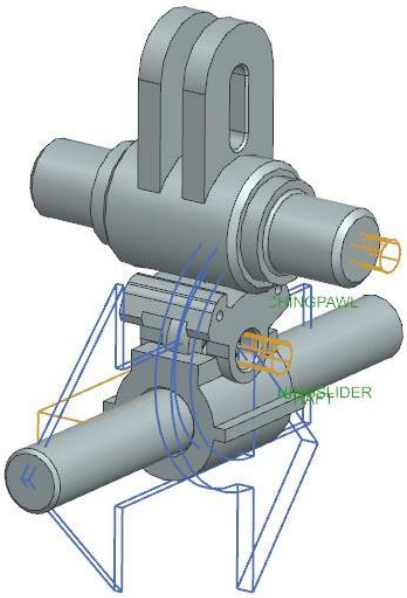

Figure 116. Simulation settings for the switching assembly. Source: Own elaboration.

To generate the movement of the mechanism, the prismatic pair will move at $10\ mm/s$ from a driver. If the simulation is set to perform 10 seconds of operation, the ratchet assembly will travel $10\ mm$ at the end of the simulation, enough to generate the desired rotation.

After generating the solution, the displacement values of the selector drum are obtained. Due to the limitations of the program, it has not correctly resolved the contact of the ratchet pieces, generating first the expected movement, and then an anomalous rotation. The results show that the $45°$ route, which should be travelled by the selector drum, is reached after 46% of the total pawl route. Therefore, the parameters of the simulation are defined again, generating the expected movement.

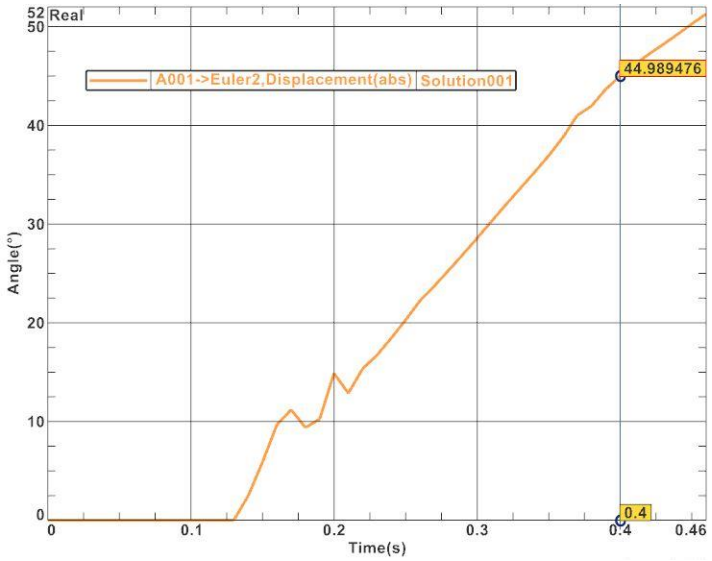

18	1.700000E-01	1.120495E+01
19	1.800000E-01	9.390664E+00
20	1.900000E-01	1.025923E+01
21	2.000000E-01	1.488816E+01
22	2.100000E-01	1.286728E+01
23	2.200000E-01	1.535536E+01
24	2.300000E-01	1.672556E+01
25	2.400000E-01	1.845385E+01
26	2.500000E-01	2.028086E+01
27	2.600000E-01	2.222396E+01
28	2.700000E-01	2.371281E+01
29	2.800000E-01	2.530295E+01
30	2.900000E-01	2.692156E+01
31	3.000000E-01	2.857618E+01
32	3.100000E-01	3.026909E+01
33	3.200000E-01	3.195348E+01
34	3.300000E-01	3.359918E+01
35	3.400000E-01	3.523975E+01
36	3.500000E-01	3.692337E+01
37	3.600000E-01	3.880486E+01
38	3.700000E-01	4.101767E+01
39	3.800000E-01	4.198278E+01
40	3.900000E-01	4.368440E+01
41	4.000000E-01	4.498948E+01
42	4.100000E-01	4.616576E+01
43	4.200000E-01	4.721382E+01
44	4.300000E-01	4.820083E+01
45	4.400000E-01	4.921992E+01
46	4.500000E-01	5.027253E+01
47	4.600000E-01	5.129178E+01

Figure 117. Resulting angles for the selector drum operation. Source: Own elaboration.

After checking the rotation of the selector drum, the next step is to simulate the displacement of the clutch. This mechanism involves the same drum, the connecting rod, and the indicator rod, as a piston.

Regarding the union pairs, figure 33 permits to understand the configuration of the mechanism. The selector drum is articulated on the bench, as defined above, while the indicator rod is attached to the bench by a prismatic pair and to the connecting rod by an articulated joint.

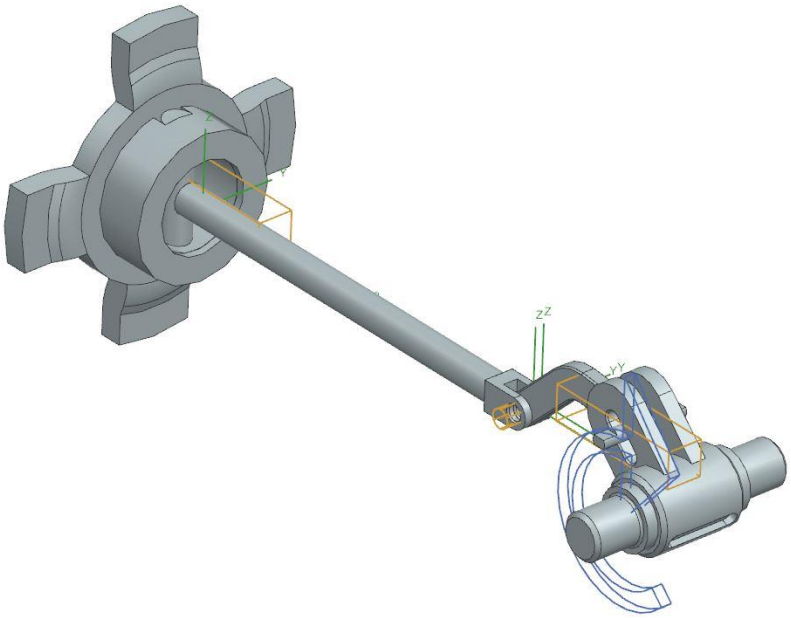

Figure 118. Simulation settings for the crank-rod-piston assembly. Source: Own elaboration.

As for the union between connecting rod and drum, a cylindrical pin is used contacting the guide of the second. This pin is also fixed to the bench by a horizontal guide. Note that due to this design, the connecting rod and the guided pin have the same movement, and therefore, in the simulation they are defined as the same part.

Overall, it is calculated that the degrees of freedom of the mechanism are reduced to one, and therefore, the clutch displacement can be activated by a single driver. This is placed in the drum, simulating ratchet drive, with a $45\,°/s$ value. If the simulation lasts one second, the drum must move $45°$ in any of its operations, resulting in the $6.5\,mm$ movement of the piston, and clutch parts.

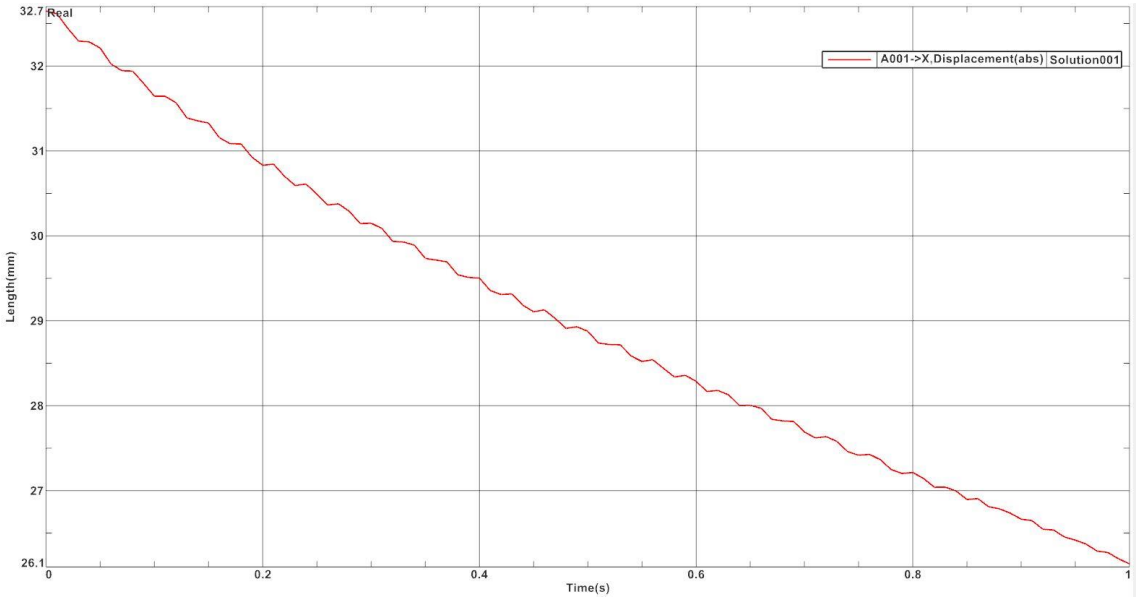

Figure 119. Resulting displacement for the piston operation. Source: Own elaboration.

Figure 119 shows the curve of the axial displacement of the piston during the shift from first to second speed. As shown, the movement generated is formed by short distances of advance alternated with small stops. However, the start and end points are separated by those $6.5\,mm$ expected.

4. BUDGET OF THE PROJECT

Below are shown and explained the costs corresponding to the design and production of the product developed throughout the proposal design.

4.1. ENGINEERING BUDGET

The engineering budget corresponds to the work performed by the designer throughout the project, in this case, the author of the project. To define a standard value per hour of work, $30\ €/h$ has been used, corresponding to a correct remuneration of a professional engineer.

ENGINEERING BUDGET	Spent time (h)	Value (30 €/h)
State of the art and market	130	3.900,00 €
Proposal drawings and definition	40	1.200,00 €
Mechanical design	115	3.450,00 €
3D models design	35	1.050,00 €
Plans drawing	30	900,00 €
Finite elements simulations	26	780,00 €
Kynematic simulations	20	600,00 €
Manufacturing process	10	300,00 €
Project tasks	220	6.600,00 €
TOTAL		**18.780,00 €**

Table 10. Engineering budget. Source: Own elaboration.

The value of the budget will be included in the total cost of the project, which will be amortized at some point, from the profits obtained in the sale of the product.

4.2. MATERIAL BUDGET

Regarding the manufacture of the product, the costs of all the elements that form it are included in the budget, all together with the standardized components.

The manufacture of the elements designed involves two types of cost: the price of the volume of material used and the production expenses of the part. In the resulting budgets, these two values are implicit in the cost of individual production.

For all parts of the product, mass production is considered, which substantially reduces the manufacturing cost for every part.

STANDARDIZED PARTS	Amount	Single cost	Total cost
Compression spring	2	5,52	11,04
Bearings	2	1,44	2,88
Tubular rivet	1	2,20	2,20
Hex bolts	4	0,26	1,04
Nuts	4	0,11	0,44
Stud bolts	2	0,16	0,32
Seeger ring	1	0,00	0,00
DESIGNED PARTS	**Amount**	**Single cost**	**Total cost**
Main cases	2	0,1280	0,2561
Bearing cases	2	0,0178	0,0355
Slider axle	1	0,0047	0,0047
Switching slider	1	0,0027	0,0027
Joint pin	1	0,0004	0,0004
Torque spring	1	5,9500	5,9500
Switching pawl	1	0,0013	0,0013
Ratchet drum	1	0,0094	0,0094
Guided pin	1	0,0002	0,0002
Connecting rod	1	0,0010	0,0010
Indicator rod	1	0,0041	0,0041
TOTAL PRODUCT COST			**24,19 €**

Table 11. Material budget. Source: Own elaboration.

The estimated value to produce the ratchet clutch system is 24.19 €.

4.3. AMORTIZATION

For the project to be viable, the sale of the product must be able to generate sufficient profits to cover the budgeted costs and, if possible, obtain profits.

The amortization time of the project depends on the sales price given to the product, which must be greater than the value of the material budget. As an assumption, a price of 200 % respect to the cost of materials used will be established, obtaining a 48.38 € final price. Part of this value is used to amortize the production costs of each unit, leaving 24.19 € to cover the engineering budget.

In order to cover the 18780 € with the profits from the sale of each product, 777 units must be sold. Setting the maximum amortization limit at three years of exchange production, the minimum number of sales must be 251 units per year, or 22 per month.

CONCLUSIONS

As introduced initially, the project has focused in completing a series of phases to develop the final proposal. Regarding the results, the following points are highlighted:

- The information obtained during the research supports the project, mainly in the development of different proposals and its technical aspects.

- In the design process two proposals are given and developed. Even though none of them are considered valid at first, the final choice combines an interesting product, which is the internal gearing hub, and a real problem to be corrected.

- The selected proposal is developed rigorously using different calculation methods, considering every part and its conditions, and the 3D modelling and drawing software.

As a general valuation, the topic of the project is interesting, and the results obtained are satisfactory.

Regarding the resulting design, the process is focused on reaching the 1.4 safety factor for every part and making the right decisions in case fail. As shown during the project, several modifications of dimensions, geometries and materials have been adopted.

In general terms, the final product is considered to satisfy the safety and functional goals. Nevertheless, some aspects of the design might describe a more complete product:

- The dimensions of the product have been defined from the parts of the internal gearing hub. As a result, most of the parts designed have a small size. Although the calculations justify the performance of these parts, this feature may correspond to problems related to the manufacturing and the mounting process.

- Regarding the calculation of loads transmitted along the mechanism, more precision is noticed to be missing. The design process may have included a previous dynamic simulation in order to stablish the working points where the forces transmitted reach their maximum value.

APPRECIATION

Finally, I would like to express my gratitude to all the people involved in the development of this project. To my tutor, Ingrid Magnusson Morer, and to the director of the mechanical department of the EPSEVG, Maurici Sivatte Adroer.

I would also like to thank the people who have accompanied me throughout my career and who have made it an experience full of professional and personal learning. Among them the teaching staff, classmates, family, and my partner.

BIBLIOGRAFIA

1. Wikipedia contributors. Bicicleta. Wikipedia, The Free Encyclopedia. Retrieved March 13, 2022, from https://es.wikipedia.org/w/index.php?title=Bicicleta&oldid=143685265

2. Wikipedia contributors. Transmisión de bicicleta. Wikipedia, The Free Encyclopedia. Retrieved March 13, 2022, from https://es.wikipedia.org/w/index.php?title=Transmisi%C3%B3n_de_bicicleta&oldid=141337356

3. Berto, F. J. (2022). bicycle. In Encyclopedia Britannica. https://www.britannica.com/technology/bicycle

4. Karl Drais Invents the Two-Wheeled Bicycle. (n.d.). Historyofinformation.com. Retrieved December 12, 2022, from https://www.historyofinformation.com/detail.php?id=2054

5. Denis Johnson - graces guide. Gracesguide.co.uk. Retrieved December 12, 2022, from https://www.gracesguide.co.uk/Denis_Johnson

6. Kirkpatrick Macmillan (1812 - 1878). BBC. Retrieved November 14, 2022, from https://www.bbc.co.uk/history/historic_figures/macmillan_kirkpatrick.shtml

7. Bicycle aerodynamics: History, state-of-the-art and future perspectives. Sciencedirect.com. Retrieved November 15, 2022, from https://www.sciencedirect.com/science/article/pii/S0167610520300441

8. Eugene Meyer - graces guide. Gracesguide.co.uk. Retrieved November 15, 2022, from https://www.gracesguide.co.uk/Eugene_Meyer

9. Bicycle History. Jimlangley.net. Retrieved November 16, 2022, from https://www.jimlangley.net/ride/bicyclehistorywh.html

10. Transmisión por cadena. Ecured.cu. Retrieved March 15, 2022, from https://www.ecured.cu/Transmisi%C3%B3n_por_cadena

11. Biciclub, & Triana, D. (2016, May 5). Los sistemas básicos de transmisión: cadena, correa y cardán. Biciclub.com. https://biciclub.com/los-sistemas-basicos-de-transmision-cadena-correa-y-cardan/

12. Hans Renold - graces guide. Gracesguide.co.uk. Retrieved November 17, 2022, from https://www.gracesguide.co.uk/Hans_Renold

13. Rover Company. Rover “safety” bicycle, 1885. Org.uk. Retrieved January 7, 2023, from https://collection.sciencemuseumgroup.org.uk/objects/co25833/rover-safety-bicycle-1885-bicycle

14. Who invented the derailleur? Disraeligears.co.uk. Retrieved November 18, 2022, from https://www.disraeligears.co.uk/site/who_invented_the_derailleur.html

15. Gradient derailleurs. Disraeligears.co.uk. Retrieved January 15, 2023, from https://www.disraeligears.co.uk/site/gradient_derailleurs.html

16. UK patent 660,230 - Hercules. Disraeligears.co.uk. Retrieved November 18, 2022, from https://www.disraeligears.co.uk/site/uk_patent_660230_-_hercules.html

17. Servicing the Sturmey-Archer AW wide-ratio three speed bicycle hub. Sheldonbrown.com. Retrieved January 15, 2023, from https://www.sheldonbrown.com/sturmey-archer/aw.html

18. Conoce 16 tipos de bicicletas y sus características. (2019, July 19). Las mejores bicicletas eléctricas, componentes, accesorios y equipación de ciclismo; BikeAnalytics. https://bikeanalytics.com/tipos-de-bicicletas/

19. Tipos de bicicleta. (2021, January 31). La Bicicleta. https://labicicleta.info/tipos-de-bicicleta/

20. Las bicicletas eléctricas de una velocidad reducen los precios y popularizan las ventas. Hibridosyelectricos.com. Retrieved December 19, 2022, from https://www.hibridosyelectricos.com/articulo/bicicletas-electrica/bicicletas-electricas-velocidad-reducen-precios-popularizan-ventas/20201105182743039665.html

21. Tráfico y Seguridad Via, R. No necesitan matricularse. Dgt.es. Retrieved December 20, 2022, from https://revista.dgt.es/es/noticias/nacional/2019/05MAYO/0531-Bicis-electricas-NP.shtml

22. Wikipedia contributors. (2022, May 17). Manual transmission. Wikipedia, The Free Encyclopedia. https://en.wikipedia.org/w/index.php?title=Manual_transmission&oldid=1088323592

23. Viso, E. (2019, September 13). Los cuatro tipos de caja de cambios. Tecvolución. https://tecvolucion.com/tipos-de-caja-de-cambios/

24. Brain, M., & Threewitt, C. (2000, April 1). How manual transmissions work. HowStuffWorks. https://auto.howstuffworks.com/transmission.htm

25. Wikipedia contributors. Transmisión manual. Wikipedia, The Free Encyclopedia. Retrieved March 15, 2022, from

https://es.wikipedia.org/w/index.php?title=Transmisi%C3%B3n_manual&oldid=142289557

26. Wikipedia contributors. Transmisión no sincronizada. Wikipedia, The Free Encyclopedia. https://es.wikipedia.org/w/index.php?title=Transmisi%C3%B3n_no_sincronizada&oldid=140039677

27. Wikipedia contributors. Transmisión manual secuencial. Wikipedia.Org. Retrieved March 17, 2022, from https://es.wikipedia.org/wiki/Transmisi%C3%B3n_manual_secuencial

28. Brain, M. (2003, April 4). How sequential gearboxes work. HowStuffWorks. https://auto.howstuffworks.com/sequential-gearbox.htm

29. Carbajal, M. (2021). Qué es una transmisión secuencial en el auto y cómo funciona - Siempre Auto. https://siempreauto.com/que-es-una-transmision-secuencial-en-el-auto-y-como-funciona/

30. Wikipedia contributors. Transmisión automática. Wikipedia, The Free Encyclopedia. https://es.wikipedia.org/w/index.php?title=Transmisi%C3%B3n_autom%C3%A1tica&oldid=142260827

31. Martín, E. (2021, November 5). Los coches eléctricos pueden tener cambio manual, aunque pueda no tener mucho sentido. Motorpasion.com; Motorpasión. https://www.motorpasion.com/futuro-movimiento/coches-electricos-pueden-tener-cambio-manual-pueda-no-tener-mucho-sentido

32. Ávila, D. (2021, September 20). Cambios automáticos: tipos, cómo funcionan y características. Actualidad Motor. https://www.actualidadmotor.com/cambios-automaticos-tipos-funcionamiento-caracteristicas/

33. Wikipedia contributors. (2022b, May 24). Dual-clutch transmission. Wikipedia, The Free Encyclopedia. https://en.wikipedia.org/w/index.php?title=Dual-clutch_transmission&oldid=1089587853

34. Delgado, V. (2019, June 26). *¿Qué es mejor, doble embrague o automático convencional?* TopGear. https://www.topgear.es/noticias/garaje/mejor-doble-embrague-automatico-convencional-445223

35. Wikipedia contributors. (2022b, May 20). *Continuously variable transmission*. Wikipedia, The Free Encyclopedia. https://en.wikipedia.org/w/index.php?title=Continuously_variable_transmission&oldid=1088860113

36. La transmisión automática de un scooter: revisión y mantenimiento. (2017, March 28). Moto1Pro. https://www.moto1pro.com/reportajes-motos/la-transmision-automatica-de-un-scooter-revision-y-mantenimiento

37. Harris, W. (2005, April 27). *How CVTs work*. HowStuffWorks. https://auto.howstuffworks.com/cvt.htm

38. EPSEVG Departamento de ingeniería mecánica. Diseño de máquinas. Tema 7-Trenes de engranajes. Cap09-01 Engranatges i trens.pdf

39. Single speed electric bike. (2021, December 29). Desiknio; Desiknio Cycles. https://desiknio.com/e-bikes/x35-single-speed/

40. Troubleshooting sturmey archer 3-speed hubs. Terminalcityriders.Ca. Retrieved November 28, 2022, from https://terminalcityriders.ca/articles/troubleshooting-sturmey-archer-3-speed-hubs/

41. TecknoMechanics [@TecknoMechanics]. (2020, February 10). How a motorcycle transmission works (Animation). Youtube. https://www.youtube.com/watch?v=g8xnIFf4id4

42. Sturmey Archer Ltd. AW 3 Speed Wide Ratio Gear. Sturmey-archerheritage.com. Retrieved February 20, 2023, from http://www.sturmey-archerheritage.com/files/view-1046.pdf

43. Bujes, ejes, dimensiones - estado de la técnica. Bike-components.de. Retrieved March 20, 2023, from https://www.bike-components.de/blog/es/comprendiendo/bujes-ejes-dimensiones-estado-de-la-tecnica/

44. Czarface. (2018, November 14). Frame spacing/hub O.l.d. information. Halo Wheels. https://www.halowheels.com/frame-spacing-hub-o-l-d-information/

45. Torres Coscoyuela, M., González del Pino, J., Yáñez Calvo, J., & Bartolomé del Valle, E. (1999). Estudio dinamométrico de la mano y el pulgar. Revista espanola de cirugia ortopedica y traumatologia, 43(5), 321–326. https://www.elsevier.es/es-revista-revista-espanola-cirugia-ortopedica-traumatologia-129-articulo-estudio-dinamometrico-mano-el-pulgar-13007234

46. Manganon, P. L. (2001). Ciencia De Materiales. Selección Y Diseño. Prentice Hall Mexico.

47. AISI 1006 Steel, hot rolled bar, 19-32 mm (0.75-1.25 in) round. Matweb.com. Retrieved April 23, 2023, from

https://www.matweb.com/search/DataSheet.aspx?MatGUID=dd9850edc3bc4dd589f89662e0028daa&ckck=1

48. Muelle de compresión M01LE1270. Springmakers. Retrieved May 4, 2023, from https://www.springmakers.net/es/muelles-standard/56765-muelle-compresion-m01le1270.html

49. Muelle de torsión M06LE8330. Springmakers. Retrieved May 1, 2023, from https://www.springmakers.net/es/muelles-standard/65573-muelle-torsion-m06le8330.html

50. Gonzalez, R. A. (2015). METODOS DE CALCULO DE FATIGA PARA INGENIERIA: METALES. EDICIONES PARANINFO.

51. SKF. Skf.com. Retrieved April 11, 2023, from https://www.skf.com/pe/products/rolling-bearings/ball-bearings/deep-groove-ball-bearings/productid-626

52. AISI Type W1 Tool Steel, water quenched at 775°C (1425°F), tempered 350°C (660°F). Matweb.com. Retrieved May 18, 2023, from https://www.matweb.com/search/DataSheet.aspx?MatGUID=29bd5fccff234a4ea7b458f865323afd

53. AISI 1010 Steel, cold drawn. (n.d.-b). Matweb.com. Retrieved April 22, 2023, from https://www.matweb.com/search/DataSheet.aspx?MatGUID=025d4a04c2c640c9b0eaaef28318d761

54. AISI 1016 Steel, cold drawn, 19-32 mm (0.75-1.25 in) round. (n.d.). Matweb.com. Retrieved May 31, 2023, from https://www.matweb.com/search/DataSheet.aspx?MatGUID=ee1200a693f5462982452165a18447cb